

ABSTRACT

Title of Document: SCANNING TUNNELING MICROSCOPY /
SPECTROSCOPY
STUDIES OF BINARY ORGANIC FILMS

Wei Jin Doctor of Philosophy, 2010

Directed By: Janice Reutt-Robey, Professor
Chemical Physics Program
Department of Chemistry and Biochemistry

Multi-component organic molecular films have seen increasing applications in photovoltaic technologies and other organic electronic applications. These applications have been based upon assumptions regarding film structure and electronic properties. This thesis provides an increased understanding of factors that control structure in binary molecular films and begins to establish structure-electronic property relations. In this thesis, three technologically relevant “donor-acceptor” systems are studied with variable temperature STM/STS: pentacene (Pn):C₆₀, zinc phthalocyanine (ZnPc): C₆₀ and ZnPc: perfluorinated zinc phthalocyanine (F₁₆ZnPc). These three model systems provide a systematic exploration of the impact of molecular *shape* and molecular *band offset* on morphology-electronic relations in thin film heterostructures.

For Pn:C₆₀, I show how domain size and architecture are controlled by composition and film processing conditions. Sequential deposition of pentacene,

followed by C_{60} , yields films that range from nanophase-separated, to co-crystalline phases, to a templated structure. These distinct structures are selectively produced from distinct pentacene phases which are controlled via pentacene coverage.

For the ZnPc: C_{60} system, the shape of ZnPc and the lattice mismatch between ZnPc and C_{60} are quite different from the Pn: C_{60} films. Nonetheless, ZnPc: C_{60} films also yield chemical morphologies that can be similarly controlled from phase separated, to co-crystalline phases, to templated structures. In both of these binary films, I exploit relative differences in the component cohesive energies to control phase selection. In bilayer films of both systems, a common structural element of stress-induced defects is also observed.

In ZnPc: F_{16} ZnPc, I explore two components with similar shapes and cohesive energies while retaining molecular band offsets comparable to Pn: C_{60} . In this shape-matched system, a checkerboard ZnPc: F_{16} ZnPc arrangement stabilized by hydrogen bonds readily forms. This supramolecular structure introduces a new hybridization state close to the Fermi Level, yielding electronic properties distinct from the component phases.

Through investigations of these three model systems, I have developed an understanding the control of chemical morphology along the donor-acceptor interface and the way this morphology influences electronic transport.

SCANNING TUNNELING MICROSCOPY / SPECTROSCOPY STUDIES OF
BINARY ORGANIC FILMS

By

Wei Jin

Dissertation submitted to the Faculty of the Graduate School of the
University of Maryland, College Park, in partial fulfillment
of the requirements for the degree of
Doctor of Philosophy
2010

Advisory Committee:
Professor John D. Weeks, Chair
Professor Theodore L. Einstein
Professor Michael A. Coplan
Professor Ellen D. Williams
Professor Philip R. DeShong

Dedication

This work is dedicated to my parents and my family

Acknowledgements

It is a pleasure to thank the many people who made this thesis possible.

First and foremost, I am heartily thankful to my advisor, Dr. Janice Reutt-Roby, for her consistent support throughout the years of my graduate study. Her encouragement, guidance and support from the initial to the final stages helped me to develop a comprehensive understanding of the subject.

It is difficult to overstate my gratitude to Dr. Daniel Dougherty. With his enthusiasm, his inspiration, and his great efforts to explain physics clearly and simply, he helped to make STM experiments fun for me. I am proud of being “the first student he has influence on”.

I would like to thank Dr. Bill Cullen for helping me run all the experiments, fixing all the instruments I broke and delicious dessert he always brings into lab.

Dr. Ellen Williams, Dr. John Weeks, Dr. Ted Einstein, Dr. Phil DeShong and Dr. Michael Coplan deserve special thanks as my thesis committee members.

I must thank all of my friends from surface science group, Yinying Wei, Brad Conrad, Jianhao Chen, Michelle Zimmermann, Blake Riddick, Qiang Liu, and also Pengyi Zhang, Hongzhong Zhou, Lin Yuan from another “non-science” group. My time here in Maryland would have been much more difficult without their friendship.

I wish to thank my parents for the support they provided me through all these years. In particular, I must acknowledge my husband, Chen, without his love and encouragement, I would not have finished this thesis.

TABLE OF CONTENTS

Dedication.....	ii
Acknowledgements.....	iii
List of Tables.....	vi
List of Figures.....	vii
Glossary of Abbreviations.....	xiv

1. CHAPTER 1 INTRODUCTION 1

1.1. MOTIVATION.....	1
1.2. ORGANIC MOLECULES ADSORBED ON SURFACES.....	6
1.3. INVESTIGATION METHODS.....	9
1.4. THESIS OVERVIEW.....	10

2. CHAPTER 2 EXPERIMENTAL METHODS 12

2.1. SCANNING TUNNELING MICROSCOPY (STM)/ SCANNING TUNNELING SPECTROSCOPY (STS)	12
2.2. EXPERIMENTAL SETUP	19

3. CHAPTER 3 SINGLE COMPONENT MONOLAYER PHASES 27

3.1. C₆₀ ON AG(111)	27
3.2. PENTACENE ON AG(111)	30
3.3. NEAT ZINC PHTHALOCYANINE (ZnPC) AND PERFLUORINATED ZINC PHTHALOCYANINE (F₁₆ZnPC) ON AG(111).....	48

4. CHAPTER 4 BINARY SYSTEM: PENTACENE: C₆₀ 58

4.1. PENTACENE STANDING UP ON C₆₀ MONOLAYER.....	58
4.2. C₆₀ CHAINS ON PENTACENE BILAYER.....	69
4.3. C₆₀-PENTACENE NETWORK.....	79

5. CHAPTER 5 BINARY SYSTEM: ZINC PHTHALOCYANINE: C₆₀ 95

5.1. ZnPC HIGHLY TILTING ON C₆₀ MONOLAYER.....	95
5.2. REVERSED DEPOSITION: FORMATION OF WANDERING C₆₀ CHAINS	110
5.3. C₆₀-INDUCED ZnPC DISPLACEMENT: FORMATION OF C₆₀-ZnPC CO-CRYSTALLINE MONOLAYER	125

6. CHAPTER 6 BINARY SYSTEM: ZnPC:F₁₆ZnPC 133

6.1. INTRODUCTION	133
6.2. EXPERIMENTAL	135
6.3. RESULT	135
6.4. DISCUSSION	140
6.5. SUMMARY	142

7. CHAPTER 7 SUMMARY AND OUTLOOK	143
---	------------

LIST OF TABLES

Table 6.1 Primitive Vector Parameter of the adsorbed overlayer with respect to Ag(111)*	138
--	-----

LIST OF FIGURES

- Figure 1.1 Schematic illustrations of the four key steps in the generation of photocurrent from incident light in OPV cell: (1) photo absorption, (2) exciton diffusion to donor-acceptor interface; (3) exciton dissociation and separation, which is driven by HOMO-LUMO offset, and (4) carriers collection at the electrode.....3
- Figure 1.2 Schematic illustrations of (a) bulk heterojunction with high donor-acceptor interfacial area for organic solar cell; (b) the effect of relative orientation and donor-acceptor distance on charge separation at the donor-acceptor interface.5
- Figure 1.3 Electronic structure of a metal and an organic solid (a) assuming common vacuum level; (b) assuming a shift of vacuum level Δ at the interface due to dipole layer formation. In this figure, the organic side is charged positive, increasing the electron affinity (EA).8
- Figure 1.4 Schematic illustration of strategy for fabricating binary films with distinct chemical morphologies: (a) Monolayer phase diagram of single components A and B showing richer phase behavior for A component; (b) Left column: Structurally distinct monolayers of A (labeled i-iv) produced by temperature-coverage ($T - \theta$) control; Right column, Structurally distinct binary films produced by B deposition on A monolayers i-iv..... 10
- Figure 2.1 Schematic illustration of STM in constant current imaging mode. Images are acquired by moving the tip across the surface while recording the tip height (z) needed to maintain constant tunneling current at a fixed bias voltage..... 15
- Figure 2.2 Schematic illustration of $z(V)$ curve measurement 17
- Figure 2.3 Validation of $z-V$ scanning tunneling spectroscopy. Comparison of the highest occupied molecular orbitals (HOMO) for $(2\sqrt{3} \times 2\sqrt{3})R30^\circ\text{-C}_{60}/\text{Ag}(111)$: (a) $z-V$ spectroscopy, (b) ultraviolet photoemission spectroscopy (UPS) 18
- Figure 2.4 Cross section of the UHV chamber and its components; (a) Linear transfer arm; (b) Organic molecular evaporators; (c) Gate valve; (d) Load lock chamber; (e) Quartz crystal microbalance; (f) Screw to adjust crystal position; (g) Gate valve; (h) Organic molecular evaporator; (i) x-y-z sample manipulator; (j) Heated sample stage; (k) Sputter gun; (l) Tip/sample carousel; (m) VT-STM; (n) Wobble stick; (o) CCD camera; 19
- Figure 2.5 (a) Omicron VT-STM stage after removal of vacuum shroud.

(http://www.omicron.de/products/spm/variable_temperature_instruments/vt_stm/). (b) Schematic illustration of VT-STM scanner arrangement.....	21
Figure 2.6 Representative STM image of (a) A clean Ag(111) surface with pits and mounds right after sputtering; (b) A clean, smooth Ag(111) surface after sputtering and annealing.	24
Figure 2.7 Schematic illustration of experimental tip-etching setup: (a) coarse etch; (b) fine etch	25
Figure 2.8 Schematic of the STM tip conditioning process: Thermionic emission from a nearby tungsten filament bombards the STM tip. A tip-filament potential difference of 200 V and a filament current of 1.0 A are typical.....	26
Figure 3.1 Chemical structure of C ₆₀	28
Figure 3.2 STM images of C ₆₀ on Ag(111) (a) STM image shows C ₆₀ monolayer. A topographic profile is shown for the indicated line; (b) $(2\sqrt{3} \times 2\sqrt{3})R30^\circ$ commensurate structure model of C ₆₀ is superimposed on the STM image, (c) Structural model.	29
Figure 3.3 Structural models: (a) Individual pentacene molecule; (b) (110) plane of bulk pentacene shows herringbone molecular arrangement	31
Figure 3.4 Growth of ordered pentacene on Ag(111) at room temperature for different deposition times: (a) 30 s; 2D gas; (b) 60 s; stripes appears at silver step edges (white arrows); (c) 78 s; (d) 106 s; stripes increases in area with deposition time.....	34
Figure 3.5 Percentage surface covered by ordered pentacene structures at room temperature as a function of deposition time under constant pentacene flux of 10^{-4} nm/s measured by QCM. This plot includes Figure 3.4 measurements and additional images acquired during the same growth experiment. Error bars represent the standard deviation of percent coverage measured in different regions of the surface (3-5 different 50-100nm regions). Inset: The same data plotted versus the nominal thickness measured with a QCM during the sequential deposition steps.....	35
Figure 3.6(a) STM image measured at 50 K after pentacene deposition at 300 K illustrating order surrounding bilayer island edges ;(b) STM image measured at 50 K illustrating first layer molecules that are partially covered by second layer molecules near an island boundary. Note that second layer molecules (unit cell indicated by the white polygon) in this image appear as two-lobed structures. Schematic of pentacene bilayer unit cells on Ag(111): (c) Top view (d) Side view	37

Figure 3.7 STM image measured at 50 K after growth at 300 K reveals coexistence of two different ordered monolayer phases.....	38
Figure 3.8(a) STM image showing a structure 1 domain with the unit cell highlighted and (b) STM image showing a structure 2 domain with the unit cell highlighted.	38
Figure 3.9 Schematic of pentacene monolayer unit cells on Ag(111): (a) structure 1 and (b) structure 2.	41
Figure 3.10 Phase diagram of pentacene on Ag(111)	47
Figure 3.11 Molecular structures of zinc phthalocyanine and perfluorinated zinc phthalocyanine and ionization energies and electron affinities from PM3-MO calculation.	50
Figure 3.12 Superposition of successive phthalocyanine molecules in a molecular column along the <i>b</i> axis: (a) α -polymorph; (b) projection on (100) in α -polymorph; (c) β -polymorph; (d) projection on (001) in the β -polymorph. The differences between α and β -polymorph are (i) the tilt angle of the molecules within the columns and (ii) the mutual arrangement of the columns.	51
Figure 3.13 (a-b) STM images of ZnPc monolayer structures. Insets show higher resolution images and unit cells for each structure. (a) Metastable low-density phase, produced by deposition on room temperature substrate; (b) Stable high-density phase, produced by vacuum deposition and annealing to 400K. Both monolayers have point-on-line registration to substrate. (c) Structural model.....	54
Figure 3.14 (a-b) STM images of F ₁₆ ZnPc monolayer. Film consists of alternating double row structures, labeled A and B. Unit cell (large parallelogram) has parameters $a = 1.50 \pm 0.02$ nm, $b = 6.55 \pm 0.03$ nm, $\theta = 81 \pm 3^\circ$; (c) Molecular packing in the two double row structures A and B. Rows A: Rectangular arrangement with 1.50 nm and 1.68 nm nearest- and next-nearest-neighbor molecular spacings; Rows B: Oblique arrangement with 1.50 nm and 1.72 nm nearest and next-nearest neighbor molecular spacings and an internal angle of 65°	56
Figure 4.1 (a) STM image showing a pentacene island on top of 1 ML C ₆₀ /Ag(111). (b) Distance-voltage characteristic (average of 13 sweeps measured at different locations) for a pentacene island. HOMO-derived structure is marked by the arrow. (c) STM image showing the edge of a pentacene island on 1 ML C ₆₀ . (d) Line profile across the point on the island edge indicated by the blue	

line in (c).....	62
Figure 4.2 (a) STM image of pentacene on C ₆₀ showing several parallel bright stripes meandering on the surface. (b) Large scale STM image showing a parallel array of bright domains extending over large distances and over numerous monatomic Ag surface steps.....	64
Figure 4.3 (a) STM image of pentacene on C ₆₀ showing molecular scale features; inset: overlay of a possible registry between standing pentacene molecules (blue lines) and the C ₆₀ sublayer (green circles). Schematic model of the vertical defects in the pentacene overlayer due to: (b) Changing tilt angle. (c) Rigid shift.....	65
Figure 4.4 (a) STM image of an isolated C ₆₀ molecule (apparent height of ~0.5nm above the pentacene substrate) on pentacene bilayer. The apparent lateral dimension of the C ₆₀ molecule is exaggerated due to the convolution of the real shape of the molecule with the shape of the STM tip; the unit cell of pentacene bilayer is highlighted; (b) Large scale STM image illustrating the formation of linear C ₆₀ structure (white arrow) on the pentacene bilayer.....	71
Figure 4.5 (a) STM image showing the disordered C ₆₀ phase confined in linear C ₆₀ chains; (b) STM image showing the C ₆₀ meandering chains.....	72
Figure 4.6 STM image showing a linear C ₆₀ structure with molecular resolution.	72
Figure 4.7 Schematic model of the arrangement of a C ₆₀ molecule on the pentacene bilayer; (a) Side view; (b) Top view;(c) Side view.	73
Figure 4.8 Tunneling spectra acquired in <i>z</i> - <i>V</i> mode: (a) On pentacene bilayer with HOMO and LUMO peak position indicated; HOMO traces averages 24 sweeps; LUMO traces average 30 sweeps; (b) C ₆₀ chains with HOMO and LUMO peak position indicated. HOMO traces averages 29 sweeps; LUMO traces average 33 sweeps. The initial condition is 23 pA 1.2 V for all four traces.	75
Figure 4.9 Linear fit to polarization energy <i>E</i> _{pol} versus the number of nearest neighbors.....	77
Figure 4.10 STM images of surface structures prepared by deposition of 0.4 ML C ₆₀ onto a 0.8 ML pentacene (2D gas) film at 300 K: (a) Extended domains of the network structure coexist with smaller regions of 2D pentacene gas (b) Structural uniformity and (c) Characteristic length scales of the network and pore features.	82
Figure 4.11 STM image of C ₆₀ post-adsorbed on the pentacene-C ₆₀ network. Magnified inset with network grid overlay confirms C ₆₀ decoration of network	

pore sites.	83
Figure 4.12 Comparison of dz/dV local tunneling spectra for C_{60} network structure (green) and reference C_{60} close-packed island (red) on Ag(111). Energy alignment of 4.4 eV image state feature confirms direct C_{60} -Ag(111) contact in network structure. Spectra acquired with initial tunneling condition of -0.87 V and 30 pA.	84
Figure 4.13 Proposed structural models for network structure showing alternating rows of C_{60} and C_{60} connected by pentacene (a) Top view, (b), (c) Side view	85
Figure 4.14 STM image of (a) A C_{60} island surrounded by the pentacene 2D gas phase. (b) Magnified STM image of the C_{60} island showing C_{60} forming close pack structure. The C_{60} island is very rough by comparison to the compact hexagonal C_{60} islands that form on clean Ag(111). This increased island boundary length reflects a decrease in the boundary energy due to attractive C_{60} -pentacene gas interactions. This phase separated structure was prepared by the deposition of C_{60} (0.6 ML) on the 2D pentacene gas (0.4 ML).	87
Figure 4.15 STM images of structural patterns generated directly by C_{60} deposition on dense 2D pentacene gas at room temperature: (a) 1.2 ML pentacene film structure prior to C_{60} deposition; (b) Multi-phase structure following 0.4 ML C_{60} deposition. Two networks (labeled 1, 2) form in 2D pentacene gas region, while C_{60} chains assemble on the pentacene bilayer. Inset: Network structure 2 magnified. (c) Multi-phase structure following 0.6 ML C_{60} deposition. Small pentacene 2D gas island is bounded by network structure 1 and pentacene bilayer-supported C_{60} chains; (d) Line profiles of pentacene 2D gas: blue- before C_{60} deposition (low pentacene density), green- after C_{60} deposition (high pentacene density)	88
Figure 4.16 Schematic illustration of network formation mechanism upon C_{60} deposition on 2D pentacene gas.....	91
Figure 4.17 Schematic model of the local C_{60} -pentacene arrangement in network structure emphasizes favorable pentacene quadrupole - C_{60} octapole interactions: (a) side view, (b) top view	92
Figure 5.1 (a) Large scale of STM image showing a ZnPc island on top of 1 ML C_{60} /Ag(111); (b) STM image showing domain boundary of the ZnPc islands: α -phase along $[110]$ of C_{60} monolayer, β -phase along $[112]$; Inset: Line profile across the point on the island edge for two phases indicated by the dark blue (β -phase) and bright blue (α -phase).....	99
Figure 5.2 (a-b) STM images showing (a) the α -phase ZnPc on C_{60} monolayer,	

containing three ZnPc stripes of varying intensity: A (bright), B (medium) and C(dim.) with variable spacing (b) molecular scale features; (c) Histogram of the number of near-neighbor A-striations between any two C-striations; Proposed model: (d) Top view; (e) Side view.....	101
Figure 5.3 (a) STM image of the ZnPc β -phase on C_{60} showing (b) Magnified image showing two inequivalent orientations marked as green and red; Proposed model of the ZnPc β -phase islands:(c) Top view; (d) Side view.	102
Figure 5.4 (a) STM image of post-deposition annealed ZnPc island on C_{60} showing a compacted shape relative to room-temperature-grown islands; (b) Line profile across the point on the island edge indicated by the blue line in (a); (c) STM image showing molecular scale features with unit cell superimposed; (d) Top view of proposed model; (e) Side view of proposed model.	103
Figure 5.5 (a) STM image showing a F_{16} ZnPc island on a 1 ML $C_{60}/Ag(111)$, The C_{60} close packed $[110]$ direction is highlighted in green; Inset: Line profile across the point on the island edge indicated by blue line; (b) STM image showing molecular scale features; Defect is marked by dark green circle; Different number of molecular features in different stacks are highlighted by the light green circle; (c) Schematic model of the point defects at the end of each stack; vector along $[112]$: top view (Actual tilt angle is shown in the side view), (d) Histogram of the number of F_{16} ZnPc molecules contain in each stack.	106
Figure 5.6 (a) STM image of 0.3 ML C_{60}/HD -ZnPc monolayer; Magnified inset shows bare HD-ZnPc region, confirming the lack of structural change; (b) 1 ML C_{60}/HD -ZnPc monolayer; (c) Molecularly resolved STM image shows quasi-linear C_{60} chains of single-molecule width; (d) Molecularly resolved STM image shows chain coarsening after annealing at 400 K; (e) Histograms of the coordination number (N_c) probability of C_{60} in unannealed samples (red) and annealed samples (green). The coordination number probability of unanneal sample (red) peaks at $N_c=2$, indicating the presence of linear structures. (f) Molecularly resolved STM image shows very similar quasi-linear C_{60} chains on pentacene bilayer support.	115
Figure 5.7 Effective C_{60} - C_{60} interaction: Girifalco potential with dipole-dipole repulsion.....	118
Figure 5.8 Simulated structures based upon the 2D dipole fluid potential with dipole values ($N=685$ particles in $35\text{ nm}\times 35\text{ nm}$ plane at room temperature): (a) 16.8 D; (b) 19.2 D; (c) 20.6 D; (d) 23.8 D. Substrate corrugation is excluded from the simulation. Snapshots are following 1.6×10^4 ps of elapsed time.....	119

- Figure 5.9 Pair distribution function $g(r)$ obtained from the molecular dynamic simulation performed with a dipole value of $p=23.8$ D (Figure 5.8.c) and from measurement. Experimental values are based upon the analysis of 3 samples and 11 images (corresponding to a total analyzed area of 4400 nm^2) 120
- Figure 5.10 (a) STM image of surface structure following the annealing of a binary film consisting of a C_{60} wandering phase supported on a LD-ZnPc monolayer. ($T=400$ K, $t=15$ minutes). Domains of the co-crystalline zigzag network coexist with the HD-ZnPc monolayer (b) Magnified STM image of the co-crystalline structure. (c) Structural parameters for the array superimposed on the STM image..... 128
- Figure 5.11 Comparison of dz/dV local tunneling spectra for C_{60} zigzag structure (green), C_{60} meandering chains on ZnPc monolayer (blue) and reference C_{60} close-packed island (red) on Ag(111). Energy alignment of 1.9 eV HOMO feature confirms direct C_{60} -Ag (111) contact in zigzag chains. Spectra acquired with initial tunneling condition of -1.27V and 0.05nA..... 129
- Figure 5.12 Proposed structural models for the co-crystalline C_{60} -ZnPc phase, consisting of C_{60} zigzags arrays 130
- Figure 5.13 Schematic illustration of 2D co-crystalline formation mechanism upon C_{60} displacing ZnPc after annealing. 132
- Figure 6.1(a-b) STM images of ZnPc: F_{16} ZnPc intermixed monolayer. Topographic profile along dark blue line shown in inset. (c) Structural model of commensurate checkerboard phase. Registration to Ag(111) determined with the assistance of a $(2\sqrt{3} \times 2\sqrt{3})R30^\circ$ - C_{60} calibrate (not shown). (d) Molecular neighbors in checkerboard show two C-F...H separations, H_1 (285 pm) and H_2 (298 pm) with ± 20 pm uncertainty..... 136
- Figure 6.2 Tunneling spectra acquired in z - V mode:(a) Single component monolayer phases: For occupied molecular state: ZnPc (green) trace averages 14 sweeps at 50 pA from -0.910 V initial bias F_{16} ZnPc (red) trace averages 27 sweeps at 60 pA from -1.000 V initial bias. For unoccupied molecular state: ZnPc (green) trace averages 10 sweeps at 50 pA from -0.834 V initial bias; F_{16} ZnPc (red) trace average 10 sweeps at 50 pA from -0.839 V initial bias. (b) Intermixed Checkerboard phase: traces average 40 sweeps at 40 pA with initial -0.839 V bias for both occupied molecular state and unoccupied state ZnPc (green) and F_{16} ZnPc (red) traces acquired by separately positioning the tip over the dim and bright image features 139

GLOSSARY OF ABBREVIATIONS

2D	two dimensional
2PPES	two-photon photoemission spectroscopy
3D	three dimensional
ACA	9-acridine carboxylic acid
AFM	atomic force microscopy
amu	atomic mass unit
BN	boron nitride
CuPc	copper phthalocyanine
D	Debye
DFT	density functional theory
EA	electron affinity
F ₁₆ ZnPc	perfluorinated zinc phthalocyanine
HOMO	highest occupied molecular orbital
HOPG	highly ordered pyrolytic graphite
IP	ionization potential
IPES	inverse photoelectron spectroscopy
ITO	indium tin oxide
LDOS	local density of states
LEAD	low energy atom diffraction
LUMO	lowest unoccupied molecular orbital
ML	monolayer
MPc	metal phthalocyanine
NEXAFS	near edge x-ray absorption fine structure
NN	nearest neighbor
O/O	organic/organic
OLED	organic light-emitting diode
OMBD	organic molecular beam deposition
OPV	organic photovoltaic
OTFT	organic thin film transistor
PDF	pair distribution function
Pn	pentacene
ps	picosecond
PTCDA	perylene-3,4,9,10-tetracarboxylic-3,4,9,10-dianhydride
QCM	quartz crystal microbalance
STM	scanning tunneling microscopy
STS	scanning tunneling spectroscopy
TPD	temperature programmed desorption
UHV	ultra high vacuum
UPS	ultraviolet photoemission spectroscopy
VT-STM	variable temperature scanning tunneling microscopy

XRD
ZnPc

x-ray diffraction
zinc phthalocyanine

1. Chapter 1 Introduction

1.1. Motivation

Organic semiconductors are molecular materials formed by assemblies of molecules held together by weak van der Waals forces. This implies that the properties of the solid are directly governed by those of the individual molecules, which can be regarded as the elemental blocks of the material, and also by the way these bricks are spatially organized. These features open very attractive perspectives for controlling materials properties through molecular engineering of these assemblies. It can be expected that the electronic properties of organic semiconductors can be tuned through the modification of the chemical structure of the constituent molecules and the spatial arrangement of the molecules in the solid [1].

Organic semiconductors have certain advantages over traditional inorganic semiconductors, such as low production cost, light weight, flexibility and large area applications. Devices based on organic semiconductors have many applications, such as organic light emitting diodes (OLEDs) [2-4], organic thin film transistors (OTFTs) [5-7] and organic photovoltaic cells (OPVs) [8, 9]. The transport of charges in the organic layers plays a key role in defining the overall performance of these devices. In OLEDs, electrons injected from the cathode and holes from the anode have to migrate in opposite directions throughout organic

layer(s) to meet and recombine radiatively [10]; conversely, in OPVs, the charges generated by the dissociation of excitons have to reach the electrodes [11]. While the development of OLEDs has led to commercial products, OPVs have yet to show the performance desirable for broad commercialization.

The low efficiency of OPVs arises from the fundamental nature of charge photogeneration and transport in organic materials (Figure 1.1), which occurs as follows: (1) light absorption (exciton generation), (2) exciton diffusion, (3) exciton dissociation, and (4) charge collection [12]. In step 1, the organic material absorbs light and excitons (electron-hole pairs) are generated, with binding energies ranging from 0.1~2 eV [13, 14]. Efficient dissociation of the strongly bound excitons requires either a strong electric field ($F > 10^6 \text{ Vcm}^{-1}$) or donor-acceptor heterojunctions [15], where the dissociation is driven by offsets in the HOMO or LUMO levels of donor versus acceptor. Additional factors can also come into play [16]. Step 2 is the diffusion of excitons towards the organic-organic interface. Step 3 is exciton dissociation, resulting in electron transfer to the acceptor materials and hole transfer to the donor materials. Finally, in step 4 the newly generated free charges are transported toward the respective electrodes through organic-metal interfaces and contribute to an electrical current in the external circuit. In Figure 1.1, the organic-organic (red shade) and organic-metal (green shade) interfaces are of importance of the OPV work performance. The main body of this thesis will discuss these two interfaces.

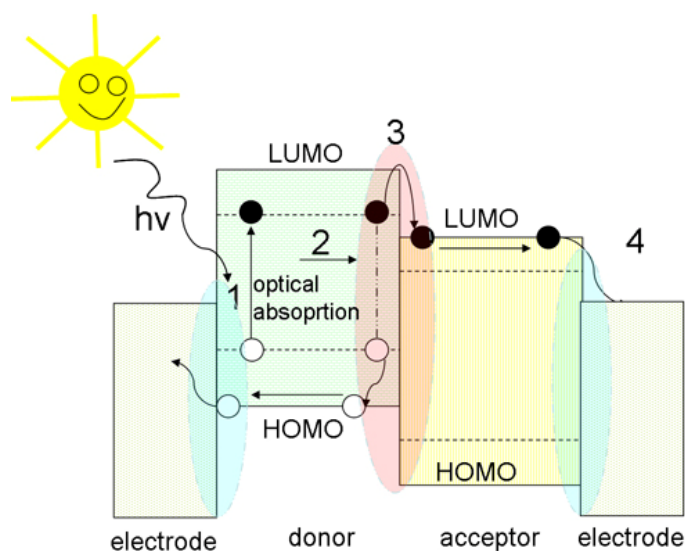


Figure 1.1 Schematic illustrations of the four key steps in the generation of photocurrent from incident light in OPV cell: (1) photo absorption, (2) exciton diffusion to donor-acceptor interface; (3) exciton dissociation and separation, which is driven by HOMO-LUMO offset, and (4) carriers collection at the electrode.

One barrier to the improvement of organic photovoltaic devices is an incomplete understanding of electronic-morphology relationship on the nanoscale. It has become evident that the same material can exhibit a wide range of performances depending on variations in nanoscale film morphology (molecular packing, domain alignment, and lateral and vertical phase separation) induced by different processing condition [17-19]. Organic molecular films contain a combination of many ordered and disordered regions, grain boundaries, heterogeneous interfaces, localized traps, and phase-separated domains. These features impact charge generation, transport, recombination, injection, extraction and trapping at sub-100nm length scales [18,20,21]. Indeed, the bulk heterojunction is a very promising device structure for organic photovoltaic applications (Figure 1.2.a). Excitons produced by photo absorption are always

within the diffusion distance of an interface, allowing efficient charge separation throughout the bulk of the device. There is great interest in understanding the molecular interactions that produce device structures reliably. Researchers have applied an entire range of structural probes, from atomic force microscopy (AFM) to x-ray scattering, to better characterize structural variations, however, there is a clear need for high-resolution measurements that correlate electronic properties directly with local film morphology at the molecular level. The goals of this thesis are to study the following two issues at the organic-organic interface and organic-metal interface:

- Effect of molecular orientation along the donor-acceptor interface on energy level alignment (Figure 1.2.b)
- Mechanisms by which nano-phase structures form and evolve in vapor-deposited films

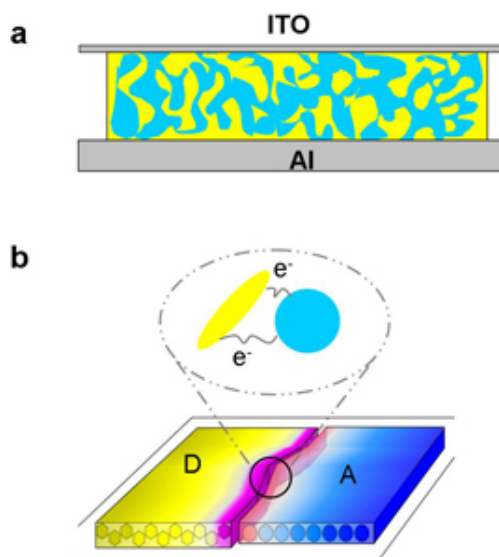


Figure 1.2 Schematic illustrations of (a) bulk heterojunction with high donor-acceptor interfacial area for organic solar cell; (b) the effect of relative orientation and donor-acceptor distance on charge separation at the donor-acceptor interface.

Within the field of organic photovoltaics, currently two different classes of materials are investigated [22, 23]: polymers and oligomers. Polymers are chain-like molecules that can be rendered soluble in organic solvents and are well suited for mass production. Oligomers and small molecules involve more handling effort such as acquiring more expensive film fabrication equipment and precise fabrication conditions, but can be prepared in very well ordered films of high purity [24]. In this thesis, I focus on small molecules and well ordered films because they are better suited to fundamental studies. The high-quality films then can serve as model systems that will ultimately make it possible to understand the properties of polymers, in particular the mechanisms governing film morphology and charge transport.

The systems I will discuss in this thesis are: pentacene (Pn) :C₆₀ [25-28], zinc

phthalocyanine (ZnPc):C₆₀ [24-26] and ZnPc :perfluorinated zinc phthalocyanine (F₁₆ZnPc). For these systems, photovoltaic efficiency has already been established, but the knowledge and control of processing conditions are still limited.

1.2. Organic Molecules Adsorbed on Surfaces

1.2.1. Fundamental Aspects of Molecular Thin Film Growth

When organic molecules are deposited on solid substrates, the situation is very complex. Molecules—in contrast to atoms—have a shape with a pronounced anisotropy. This introduces a new dimensionality to thin film growth. Moreover, molecules are nonrigid and can undergo deformation when brought into contact with a substrate. Also for many organic molecules a unique bulk structure does not exist [29]. Different polymorphs give rise to different arrangements for a given molecule and sometimes pronounced differences in molecular packing, but with very similar lattice energies.

When organic molecules are brought into contact with solid substrates, in tandem with distortion, molecules will form a bond to the substrate, the strength of which can vary from 0.5 eV to 2 eV [24]. In the simplest case of physisorption, van der Waals interactions are involved. For aromatic compounds, in particular when deposited on metallic substrates, the molecular π -system interaction with the substrate can vary dependent on aromatic molecules and substrate. For the metals

like Ag(111), the interaction can be weak (pentacene on Ag(111)) or rather strong (3,4,9,10-perylene-tetracarboxylic acid dianhydride (PTCDA)/Ag(111)) [30]. In general, the formation of ordered monolayers of organic molecules is governed by the molecule-molecule and overlayer-substrate interactions. Depending on registration to the substrate, the formation of different types of ordered monolayer structures may be classified as commensurate, coincident, or incommensurate phases [31]:

- Commensurate: All the overlayer lattice points lie simultaneously on two primitive substrate lattice lines and coincide with symmetry equivalent substrate points. This can be described as “point-on-point” coincidence.
- Coincident: Every lattice point of the overlayer lies at least on one primitive lattice line of the substrate, a condition that has been described generally as “point-on-line” coincidence.
- Incommensurate: Under this condition, no distinctive registry between the substrate lattice and the deposit lattice exists.

1.2.2. Electronic Coupling of Adsorbed Molecules to the Underlying Substrate

When organic molecules and the surface of another material are far apart, their energy levels align by sharing the vacuum level at infinite distance, as shown in Figure 1.3.a. When organic molecules are brought into contact with another

material surface, the adsorption process generally modifies the electronic structure of the molecules at the interface through polarization of the electron density of the organic materials due to interaction with the image charge on the substrate surface, rehybridized orbitals, partial charge transfer through covalent organic-substrate bonds, charge transfer across the organic-substrate interface, molecular organization by (inter)diffusion across the organic/substrate interface, and adsorption-induced reconstruction [32, 33]. These effects lead generally to the formation of a dipole layer. The dipole layer will lead to a shift of vacuum level, as shown in Figure 1.3.b. Relating the magnitude of the shift (Δ) to the electronic details presents a significant research challenge.

In the present work, the impact of molecular adsorption geometry on interfacial electronic structure will be of particular interest.

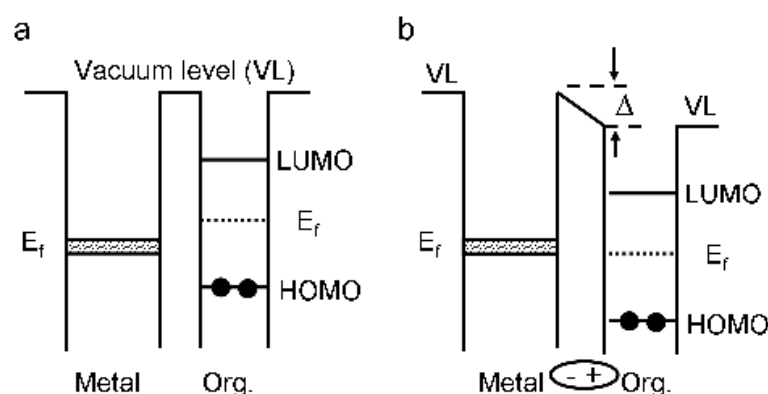


Figure 1.3 Electronic structure of a metal and an organic solid (a) assuming common vacuum level; (b) assuming a shift of vacuum level Δ at the interface due to dipole layer formation. In this figure, the organic side is charged positive, increasing the electron affinity (EA).

1.3. Investigation Methods

Morphology evolution in binary molecular films is a challenging research problem. Under the assumption of no chemical reaction between donor and acceptor molecules, thermodynamics dictates that lower temperature growth conditions will favor phase-separated domains, with higher temperature conditions generally needed for entropically driven mixed structures [31-33]. Actual film growth generally proceeds under far-from-equilibrium conditions, however, limited surface mobility leads to greater admixing at lower temperature. In the absence of donor-acceptor chemical reactions, film processing conditions, such as relative flux, substrate temperature, and deposition sequence, will control film morphology.

Organic molecular beam deposition (OMBD) is an ideal growth technique for studying the effects of the deposition conditions on the properties of molecular films [34]. Samples prepared by OMBD allow for stringent control of film thickness, composition and processing conditions. Growth strategies that involve both sequential deposition and co-deposition are used to selectively fabricate film structures that include nano-phase-separated, intermixed (co-crystalline), and layered phases. From previous studies conducted in our group, binary monolayer films of a donor (9-acridine carboxylic acid (ACA)) and an acceptor (C_{60}) were fabricated with structures that range from an intermixed chiral phase to nano-phase-separated single component domains [35]. Mismatched thermal properties, molecular masses and molecular shapes of the film constituents allow

for kinetic control of binary film morphology. To generate distinct structures, I exploited the properties (structure and mobility) of the component molecules. Scanning tunneling microscopy/spectroscopy was performed on *in situ* grown films to correlate structure with electronic properties of the same sample nanoregions.

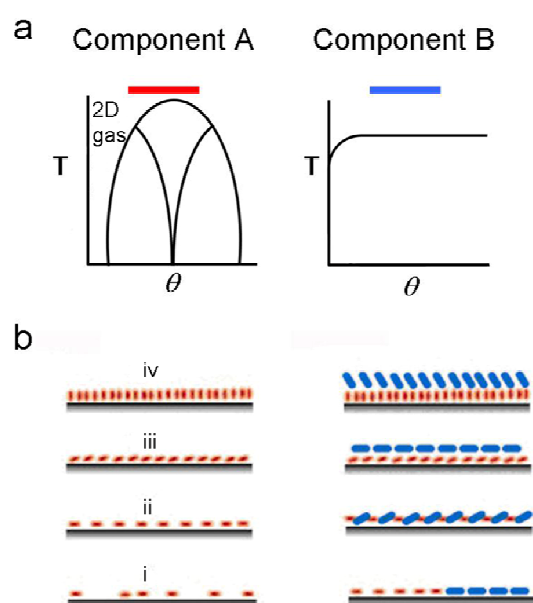


Figure 1.4 Schematic illustration of strategy for fabricating binary films with distinct chemical morphologies: (a) Monolayer phase diagram of single components A and B showing richer phase behavior for A component; (b) Left column: Structurally distinct monolayers of A (labeled i-iv) produced by temperature-coverage ($T - \theta$) control; Right column, Structurally distinct binary films produced by B deposition on A monolayers i-iv.

1.4. Thesis Overview

This thesis will present a detailed structural and electronic characterization of three different organic binary systems and contrast their properties. The experimental methods, including the ultra high vacuum systems (UHV), silver

film preparation and organic film deposition are described in Chapter 2. STM/STS measurements and data analysis are also covered in this chapter. The properties of single component molecular films: $C_{60}/Ag(111)$, pentacene/ $Ag(111)$, $ZnPc/Ag(111)$ and $F_{16}ZnPc/Ag(111)$ are presented in Chapter 3. Pentacene exhibits rich phase behavior on $Ag(111)$ with $T - \theta$ (temperature-coverage) control of gaseous, ordered monolayer and bilayer structure. $ZnPc$ exhibits two monolayer structures on $Ag(111)$ with distinctly different stability and density. In Chapter 4 three distinct pentacene: C_{60} binary architectures will be discussed: (1) bilayer structure with “standing up” pentacene; (2) C_{60} linear chains on the pentacene crystalline bilayer; (3) C_{60} -pentacene co-crystalline network. In Chapter 5 three distinct $ZnPc:C_{60}$ binary molecular films will be discussed: (1) bilayer structure with highly tilted $ZnPc$; (2) C_{60} wandering chains formation on the $ZnPc$ high density monolayer; (3) C_{60} - $ZnPc$ co-crystalline formation from the annealing of metastable $C_{60}/ZnPc$ bilayer films. In Chapter 6, co-crystalline $ZnPc:F_{16}ZnPc$ checkerboard molecular films are discussed. A summative comparison and suggestions for future work will be presented in Chapter 7.

2. Chapter 2 Experimental Methods

As discussed in Chapter 1, the electronic properties of organic thin films are, in many cases, strongly dependent on properties of the individual molecules that constitute the film. Investigation of electronic-morphology relationships at the molecular scale is thus a challenging research topic. Scanning probes are ideally suited to the study of organic semiconductor thin films because it provides structural and electronic information of the same sample nanoregions.

In this chapter, I will start with the basic principle of STM/STS. Then I will describe the experimental setups for all the experiments discussed in the following chapters.

2.1. Scanning Tunneling Microscopy (STM)/ Scanning Tunneling Spectroscopy (STS)

In 1982, Binnig and Rohrer [36] and their colleagues at the IBM labs in Zurich invented a new kind of surface analytical instrument—Scanning Tunneling Microscopy (STM). The emergence of STM represented a genuine revolution in surface science and solid-state physics. STM makes it possible to directly observe geometric and electronic surface structures on the atomic level at ambient pressure and at room temperature. This technique has revolutionized surface science and the way we study surface phenomena. G. Binnig and H. Rohrer were awarded the

Nobel Prize in physics 4 years later for their work.

The STM is based on the concept of quantum tunneling. When a sharp metallic tip is brought very close about an atomic diameter to a conducting substrate, a bias voltage applied between the two will cause electrons to tunnel through the junction. The current flow between the tip and the sample strongly depends on the tip to surface gap due to the tunneling effect. We can consider this to be physically equivalent to the 1D case of an electron encountering a rectangular potential barrier. The current transmitted is simply exponentially dependent on the barrier width [37]:

$$I \propto (V/z)\exp(-A\sqrt{\phi}z) \quad \text{Eq. (2.1)}$$

where z is the barrier width, V is the bias across the barrier, ϕ is the barrier height. Equation.(2.1) demonstrates that the probability of transmission through the barrier decreases exponentially with the thickness of the barrier (z) and the square root of the barrier height (ϕ). This fact is the basis for interpreting the images as simply a contour of constant height above the surface.

Unfortunately, this simple model is not good enough to interpret an image with sub-angstrom corrugation. In order to understand the operation of real microscopes, a more sophisticated model of the 3D tunneling current is required. The most commonly used theoretical model was developed by Bardeen in 1961 [38]. Bardeen proposed using first order time-dependent perturbation theory to solve for the overlap of the wavefunctions of tip and sample, using Fermi's golden rule. With a sample bias $-V$, the total tunneling current is calculated as [39]:

$$I = \frac{4\pi e}{\eta} \int [f(E_F - eV + \varepsilon) - f(E_F + \varepsilon)] \rho_s(E_F - eV + \varepsilon) \rho_t(E_F + \varepsilon) |M_{ts}|^2 d\varepsilon \quad \text{Eq. (2.2)}$$

where $f(E_f)$ is the Fermi function, V the applied voltage, ρ_s and ρ_t are the local density of state (LDOS) of sample and tip, M_{ts} the tunneling matrix element between electron states in tip and in sample. M_{ts} is determined by

$$M_{ts} = \frac{\eta^2}{2m} \int dS \cdot (\psi_t^* \nabla \psi_s - \psi_s \nabla \psi_t^*) \quad \text{Eq. (2.3)}$$

where the integral is over some surface in the vacuum (barrier) region separating the two sides. ψ_s and ψ_t are the wavefunctions of surface and tip, respectively.

If the Fermi level is approximated as a step-function and the tunneling matrix M is constant over the energy interval [40], the tunneling current can be written as:

$$I \propto \int_0^{eV} \rho_s(E_F - eV + \varepsilon) \rho_t(E_F + \varepsilon) d\varepsilon \quad \text{Eq. (2.4)}$$

which indicates that both states contribute equally to the tunneling current. Ideally, we would like to relate the STM image directly to a property of the surface. Since the detailed properties of the tip are unknown, we choose a form for the tip wave function proposed by Tersoff and Hamann [41]. In the Tersoff-Hamann model, the wave function of the substrate and the tip are considered as separated, undisturbed systems. The tip is treated as a spherical potential well (s wave) and the density of states of the tip is a constant. Eq. (2.4) can be further simplified, and the density of states of the sample can become:

$$\frac{dI}{dV} \Big|_V \propto \rho_s(E_F - eV) \quad \text{Eq. (2.5)}$$

From this theory, we know that the tunneling current is a function of the bias voltage V , and the distance between tip and sample. In typical constant-current

topographic imaging modes, the tip is scanned across the surface at constant tunneling current, which is maintained at a preset value by continuously adjusting the vertical tip position with the feedback voltage (Figure 2.1). The height of the tip $z(x,y)$ as a function of position is recorded and processed by a computer [42]. In this thesis, STM will be performed in constant-current topographic imaging mode.

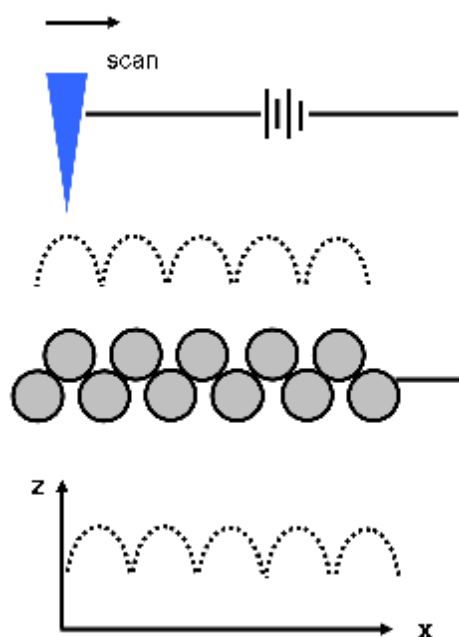


Figure 2.1 Schematic illustration of STM in constant current imaging mode. Images are acquired by moving the tip across the surface while recording the tip height (z) needed to maintain constant tunneling current at a fixed bias voltage.

While the dependence of current on position reveals the geometric structure of the surface, the dependence of current on voltage gives information about its electronic structure. As shown in Eq. (2.5), the first derivative of the tunneling current is proportional to the local density of electronic states. Of particular interest in my work is the use of an STM as an instrument to perform spatially resolved spectroscopy on a variety of organic molecular thin films at room

temperature.

Conventional I - V curves are obtained by measuring the variation of the tunneling current as a function of voltage at a constant tip-sample separation z . This measurement requires the addition of a sample-and-hold circuit to the feedback loop. This circuit holds the tip position stable while the voltage is ramped and the current response is measured. In this mode, the feedback loop is inactive, allowing the fixed tip position and even the complete nulling of current. For small voltages, <1 V, the I - V curves show a linear voltage-dependence characteristic of ohmic behavior. For larger voltages, the exponential dependence dominates the I - V characteristic. For separation $\geq 7 \text{ \AA}$, no current is observed at lower voltages. Consequently, spectroscopic data can only be obtained over a limited voltage range for a fixed separation.

Excessive currents during spectroscopy often damage film structure by displacing molecules or inducing chemical reaction. An alternative method for measuring spectroscopic data is to keep the feedback active while ramping the voltage at a fixed tunneling current to get $z(V)$ curves. The tunneling current is held constant by moving the tip. In this way the tip-sample separation is constantly adjusting itself, and a large dynamic range in voltage can be obtained. This mode is suitable for soft molecular layers at room temperature where damage by large currents in conventional $I(V)$ measurements [43-45]. To minimize film perturbation, low (~ 50 pA) currents are utilized and tip height z begins at a noncontact position (controlled via the initial voltage of ca. 0.5 V). The z position

is then monitored as voltage is increased under constant low-current conditions. Electronic states are detected as steps in the $z(V)$ trace, where the tip rapidly retracts due to an increase in tunneling probability due to the resonance (Figure 2.2). Of course, the tip response time for z motion must be faster than the ramp rate. One limitation of this approach is that lower voltages (≤ 0.4 V) cannot be measured reliably due to strong tip-sample interactions. Thus, one cannot scan through zero bias with this method. In this thesis, we utilize z - V measurements to determine the energetic positions of electronic states with respect to the Fermi level. Additional information on the LDOS is not possible because of the unknown instrumental response of the retracting tip. Experimental validation of this method is shown in Figure 2.3 where $z(V)$ spectra of $(2\sqrt{3} \times 2\sqrt{3})R30^\circ$ monolayer of C_{60} on Ag(111) (Figure 2.3.a) are used to determine the energetic positions of electronic states and are compared to the results of ultraviolet photoemission spectroscopy (UPS) (Figure 2.3.b). In general, the two measurements are in agreement within a few of tenths of an eV.

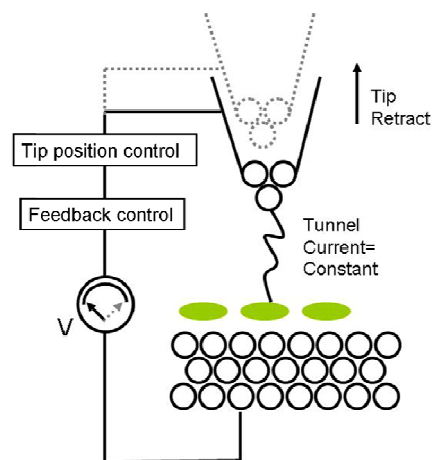


Figure 2.2 Schematic illustration of $z(V)$ curve measurement

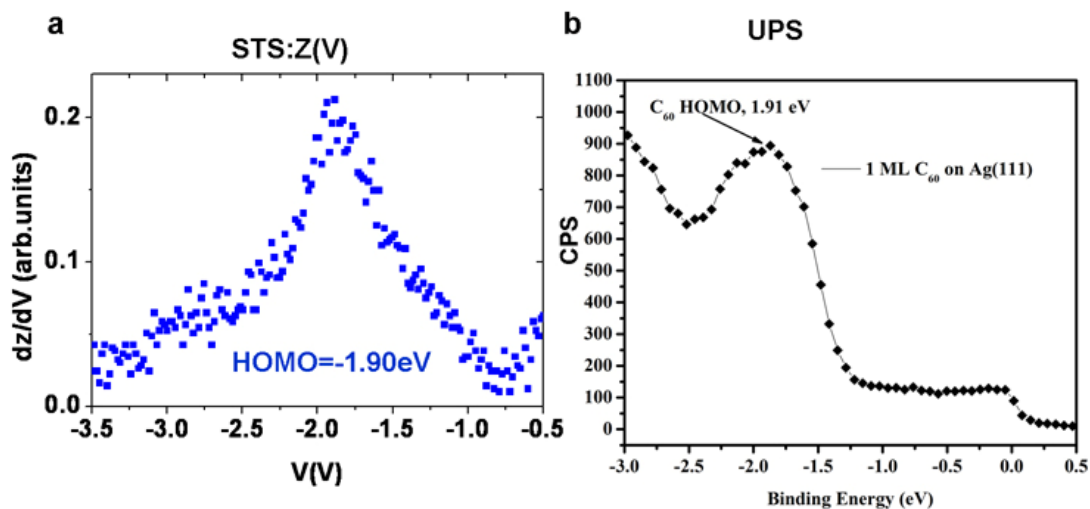


Figure 2.3 Validation of z - V scanning tunneling spectroscopy. Comparison of the highest occupied molecular orbitals (HOMO) for $(2\sqrt{3} \times 2\sqrt{3})R30^\circ$ - $C_{60}/Ag(111)$: (a) z - V spectroscopy, (b) ultraviolet photoemission spectroscopy (UPS)

In summary, the main merits of z - V STS used for this thesis are:

- It minimizes perturbation of organic films by maintaining low tunneling current;
- The morphology/composition dependence of electronic structure can be measured with submolecular resolution;
- Accurate measurements of energy state within ~ 6 eV of E_f can be reliably determined.
- Spectroscopic measurements are possible on room temperature samples.

2.2. Experimental Setup

2.2.1. Omicron VT-STM

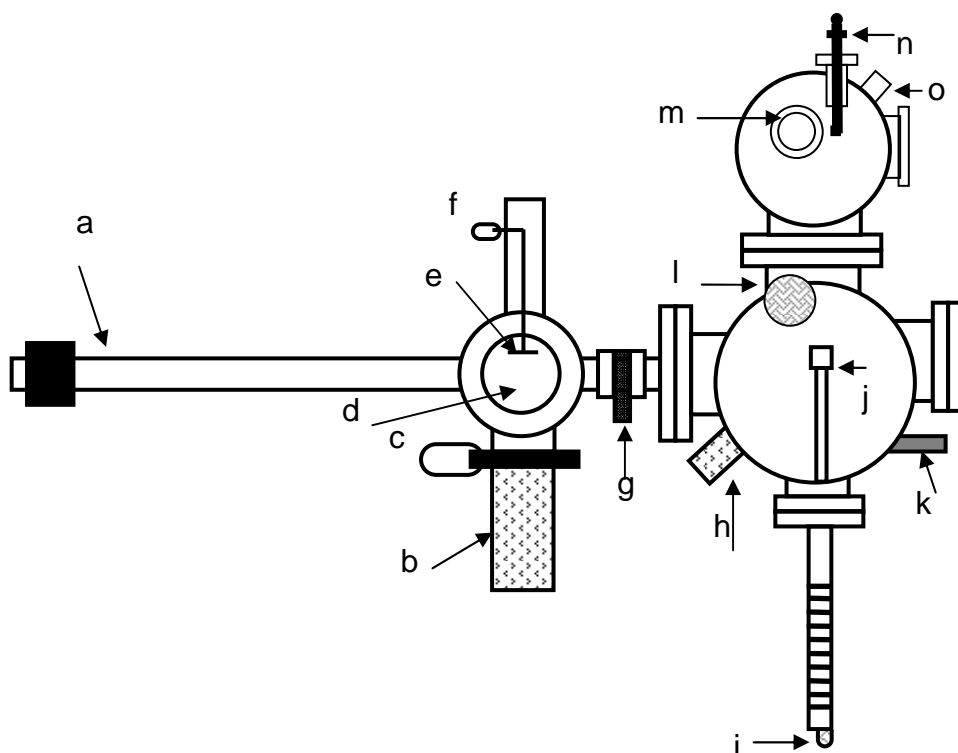


Figure 2.4 Cross section of the UHV chamber and its components; (a) Linear transfer arm; (b) Organic molecular evaporators; (c) Gate valve; (d) Load lock chamber; (e) Quartz crystal microbalance; (f) Screw to adjust crystal position; (g) Gate valve; (h) Organic molecular evaporator; (i) x-y-z sample manipulator; (j) Heated sample stage; (k) Sputter gun; (l) Tip/sample carousel; (m) VT-STM; (n) Wobble stick; (o) CCD camera;

All the experiments in this thesis were performed with an Omicron Variable Temperature STM (VT- STM) in an ultra-high vacuum chamber. Figure 2.4 is a schematic of the layout of the UHV apparatus.

The VT-STM permits STM measurements at sample temperatures from 25 K to 1400 K. In this thesis, measurements were performed at 50 K and 300 K. The four steel tubes extending perpendicular to the lower conflatTM flange house steel

springs from which the microscope stage is suspended during scanning. Copper fins surrounding the rim of the stage have magnets between them to provide additional eddy current damping (Figure 2.5.a). The smaller cylindrical tube extending at an angle through the base of the stage provides a connection from the sample to a continuous flow cryostat. The sample sits on the assembly on the center of the stage and can be transferred via a wobble stick visible.

A single tube scanner ($10\mu\text{m}\times 10\mu\text{m}$) is employed in the VT-STM. STM tips are magnetically fastened to the scanner and exchanged *in-situ* using a special tip transfer holder and the wobble stick. Figure 2.5.(b) shows a schematic of the scanner-sample assembly. The cylindrically symmetric design allows uniform thermal expansion of tip, scanner and sample. This reduces unwanted thermal drift in the tip position relative to the sample. This design further permits scanning while the temperature of the sample is changed without risk of crashing the tip or losing the tunneling signal.

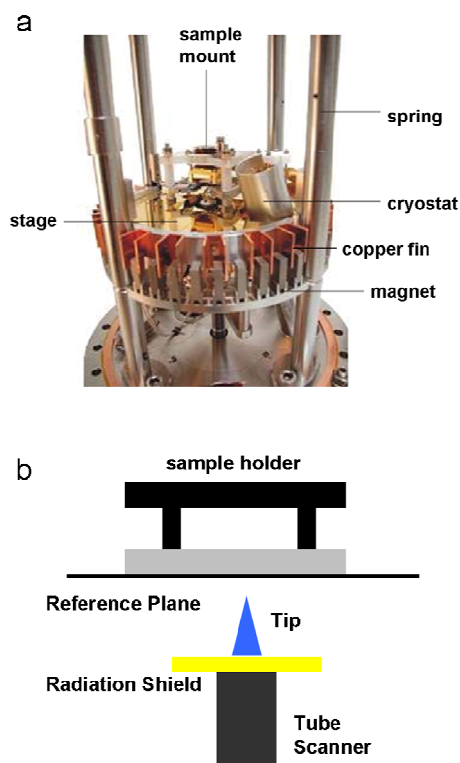


Figure 2.5 (a) Omicron VT-STM stage after removal of vacuum shroud. (http://www.omicron.de/products/spm/variable_temperature_instruments/vt_stm/). (b) Schematic illustration of VT-STM scanner arrangement

2.2.2. Ultra-high Vacuum (UHV) Requirement for Surface and Interface Characterization

The characterization of surfaces and interfaces at the atomic level requires an atomically clean surface that remains essentially unchanged over the duration of the experiment. According to the kinetic theory of gases, the flux I of molecules impinging on the surface from the environment is given by the expression

$$I = \frac{P}{\sqrt{2\pi mk_B T}},$$

where P is the pressure, m is the mass of a molecule, k_B is Boltzmann's constant, and T is the temperature. Assuming that, all the molecules that strike the surface stick, the time to form a monolayer on the surface is

calculated by the expression $\tau = \frac{n_0}{I}$, where n_0 is the number of atoms in monolayer. For a given species of gas and for a given temperature, I depends on pressure. For a typical atomic density of a surface, $n_0 = 10^{15} \text{ cm}^{-2}$, $m = 28 \text{ amu}$ (atomic mass unit), and $T \sim 290 \text{ K}$, τ is calculated to be 3 nanosecond at 760 Torr (atmospheric pressure) and 1 hour at 10^{-9} Torr [46]. Because an experiment generally takes one hour or longer, a pressure better than 10^{-10} Torr is required for the maximum contamination not to exceed a few percent of surface atomic density during an experiment. A vacuum pressure in the regime of 10^{-10} Torr, conventionally known as an ultra-high vacuum (UHV), is a prerequisite for characterization and is used in this thesis.

2.2.3. Organic Molecular Beam Deposition (OMBD)

One of the most important advantages of the use of ultrahigh vacuum (UHV) is the possibility to grow organic thin films with extremely high chemical purity and structural precision at monolayer control [47-49]. Typically, growth occurs by the evaporation of a highly purified powder from a temperature controlled oven or Knudsen cell in a background vacuum ranging from 10^{-7} to 10^{-11} Torr [50]. The organic molecules are deposited on a substrate held perpendicular to the beam approximately 10-20 cm from the source. The amount of material deposited is controlled by a combination of flux (regulated by source temperature and sample-source distance) and exposure time (regulated by a mechanical shutter,

which can switch the beam flux from “on” to “off”). Flux is calibrated with a quartz crystal microbalance thin film monitor [47].

The deposition parameters for each sample will be discussed in detail in the following chapters.

2.2.4. Substrate Preparation

The substrates used in all the experiments are Ag(111) films. The reasons we choose Ag(111) are:

- Silver is an electrode material in photovoltaic applications
- Ag(111) supports molecular adsorption of many aromatic hydrocarbons, including carboxylic acids, without chemical reaction at room temperature
- Ag(111) surface fabrication and cleaning recipe are established in our group

The Ag(111) substrates were prepared by depositing a 600~800 nm epitaxial film of Ag on freshly cleaved mica (SPI, V4 grade) under vacuum (1×10^{-6} Torr). According to an established method [51], the deposition rates were about 10 nm/s, which was monitored using a quartz crystal microbalance (QCM), while the substrate was held at a temperature of 500 K.

The films were transferred through air to the UHV chamber for further cleaning by cycles argon sputtering/annealing. In my experiment, typical ion sputtering utilized 1 KeV Ar^+ beams. The differentially pumped Ar^+ source operating at 1 KV, 10 mA at 3×10^{-6} Torr generates an ion current of $\sim 12 \mu\text{A}$.

The energetic ions exchange energy with the atoms (silver and contaminants) on and near the surface, causing ejection of bombarded species producing a chemically clean surface. The Ag(111) films were sputtered at room temperature, resulting in microscopically rough films with pits and mounds as per Figure 2.6.a. A sputtered surface can be smoothed by subsequent annealing. During annealing, the surface atoms diffuse over the surface and heal the defects. Typically the Ag(111) surface was sputtered for 1 hour and annealed at 500 K for 30 minutes. The resulting surface was then characterized by STM (Figure 2.6.b) and low energy electron diffraction (not shown) giving sharp (111) diffraction features, indicative of a single crystalline film.

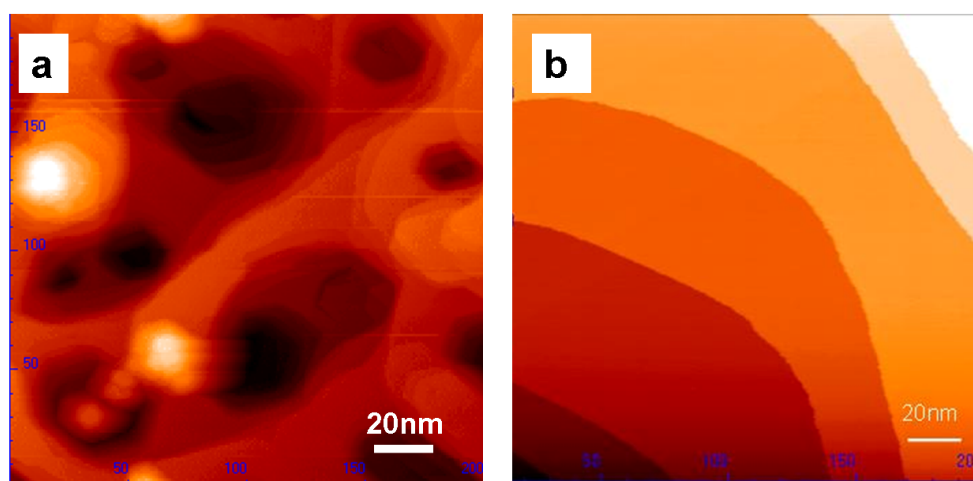


Figure 2.6 Representative STM image of (a) A clean Ag(111) surface with pits and mounds right after sputtering; (b) A clean, smooth Ag(111) surface after sputtering and annealing.

2.2.5. Tip preparation for STM

Electrochemically etched tungsten tips were used for all the experiments

presented in this thesis. They are prepared by the method reported by A. Melmed [52]. Briefly, a straight piece of tungsten wire is first etched by using 2M KOH solution and ~ 5 VAC from a VariacTM with a carbon counter electrode (Figure 2.7.a). The resulting tip is then fine etched with a thin layer of 0.5M solution KOH, suspended in a fine loop of Pt wire. The loop is moved forward over the very end of the tip under the control of an optical microscope and an AC etching voltage (3~5 V) is applied during the forward motion (with a simple on-off switch in series with the VariacTM). Fine etching is repeated until the tip end appears fuzzy due to the optical fringes that appear for the finest tips (Figure 2.7.b). After fine etching the tip is rinsed with deionized water. The tungsten tip is then transferred into the UHV chamber. Before using it for imaging, the “wet” oxide layer covering the tip is removed by an electron beam treatment. With a current of 1 A through the filament and 200 V bias applied on tip, thermally emitted electrons flow to the tip and heat it (Figure 2.8). With a maximum current to the tip of $0.1 \mu\text{A}$, the tip is heated for ~ 30 s.

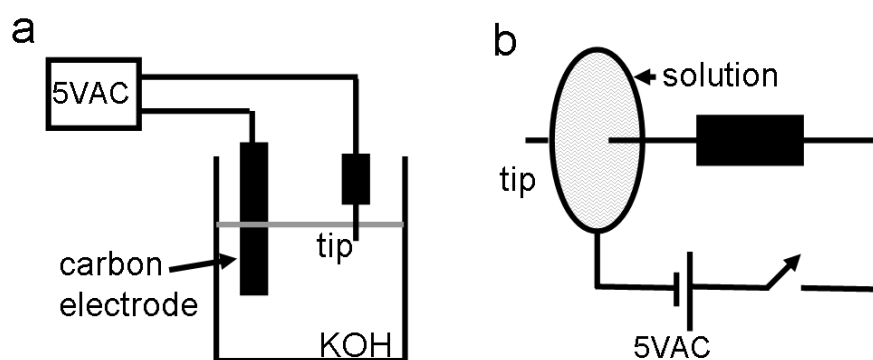


Figure 2.7 Schematic illustration of experimental tip-etching setup: (a) coarse etch; (b) fine etch

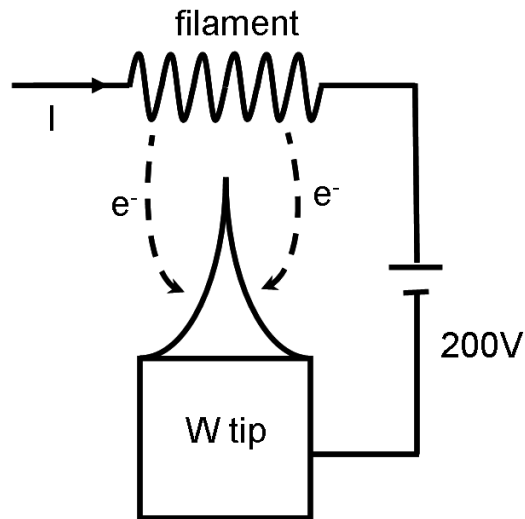


Figure 2.8 Schematic of the STM tip conditioning process: Thermionic emission from a nearby tungsten filament bombards the STM tip. A tip-filament potential difference of 200 V and a filament current of 1.0 A are typical.

3. Chapter 3 Single Component Monolayer Phases

As an introduction to the structural and electronic properties of binary systems, I will first describe single component films on Ag(111). The pentacene studies have been published in Journal of Physical Chemistry C (D. B. Dougherty, W. Jin, W. G. Cullen, J. E. Reutt-Robey, S. W. Robey, *Variable Temperature Scanning Tunneling Microscopy of Pentacene Monolayer and Bilayer Phases on Ag(111)*, the Journal of Physical Chemistry C 2008, **112**: p.20334-20339). In this collaborative effort, I did sample preparation, data acquisition and structural model determination.

3.1. C₆₀ on Ag(111)

Fullerenes are among the best acceptor materials for organic photovoltaics owing to excellent exciton mobility, a relatively stable triplet state, and a relatively large exciton diffusion length [53], which has been reported to be as long as 400 Å [54]. Combined with its high electron affinity, C₆₀ and its derivatives have received much attention and have been adopted extensively for organic solar cells [26, 55-59]. C₆₀ is an organic molecule in which the 60 carbon atoms are arranged in 20 hexagons and 12 pentagons that interlock to form a sphere. In this structure each carbon is sp^2 hybridized bonded to three other

carbon atoms with an average bond length of 1.44 \AA [60]. The calculated C_{60} diameter is 7.1 \AA [61]. C_{60} has a nearest neighbor distance of 10.04 \AA in the bulk (111) plane of the *fcc* lattice at 300 K [62]. The crystal is quite soft, with the compressibility at low pressure along *any* axis being comparable to that of graphite along its *c* axis [63]. The energy gap between the lowest unoccupied molecular orbital (LUMO) and the highest occupied molecular orbital (HOMO) is 1.9 eV [60]. C_{60} therefore is an intrinsic semiconductor.

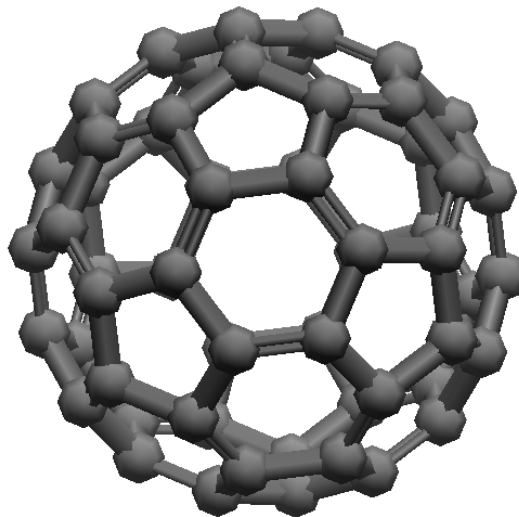


Figure 3.1 Chemical structure of C_{60}

The adsorption of C_{60} molecules on Ag(111) surfaces has been studied in numerous STM experiments [64-67]. At room temperature, C_{60} molecules are highly mobile on Ag(111) terraces and migrate and segregate to the step edge, where they nucleate and form 2D islands. The islands consist of C_{60} molecules arranged in a close-packed hexagonal structure. This $(2\sqrt{3} \times 2\sqrt{3})R30^\circ$ structure is commensurate with the substrate and all molecules are adsorbed at hollow sites [65-69]. An x-ray photoelectron diffraction (XPD) study at room temperature

concluded that the monolayer is a mixture of two orientations, one with the C_{60} hexagonal face down, and the other with a C-C bond down [70]. An *ab initio* density functional theory (DFT) calculation for the same structure found that the ground state adsorption geometry is the *hcp* hollow site, with the hexagonal face down [68], as shown in Figure 3.2.c. A partial charge transfer Δq of approximately of 0.8 electrons from the silver substrate to each C_{60} molecule in the monolayer has been reported [71]. Previous temperature programmed desorption (TPD) studies reveal that the desorption temperature for C_{60} from Ag(111) is about 770 K, with a fullerene-substrate interaction of 2 eV/molecule [65, 66].

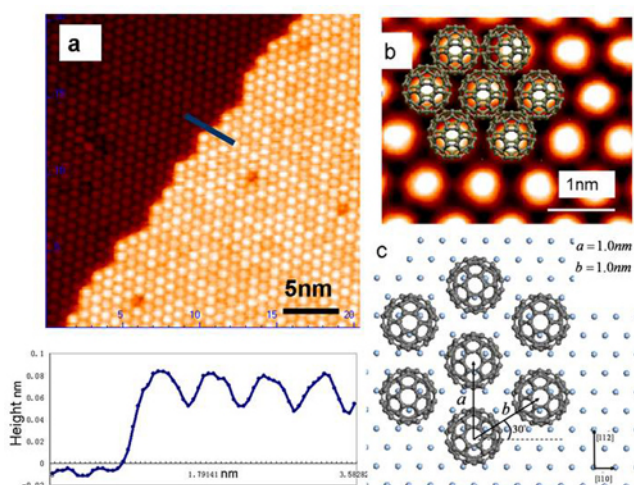


Figure 3.2 STM images of C_{60} on Ag(111) (a) STM image shows C_{60} monolayer. A topographic profile is shown for the indicated line; (b) $(2\sqrt{3} \times 2\sqrt{3})R30^\circ$ commensurate structure model of C_{60} is superimposed on the STM image, (c) Structural model.

3.2. Pentacene on Ag(111)

3.2.1. Introduction

Pentacene is currently regarded as among the most promising organic molecules for electronic device applications. Pentacene ($C_{14}H_{22}$), a fused aromatic molecule, contains of five benzene rings (Figure 3.3 a). Its bulk phase has a triclinic crystal structure with two molecules per unit cell and it forms a layered structure along the $\langle 001 \rangle$ direction, with the herringbone arrangement of molecules in the (001) plane [72, 73] (Figure 3.3.b). Organic thin film transistor based on pentacene shows charge mobilities in excess of $5 \text{ cm}^2/\text{Vs}$ [6]. Since SiO_2 is often employed as the gate dielectric in OTETs, there are many reported studies of pentacene/ SiO_2 interface formation [74-80]. On SiO_2 as well as molecular monolayer passivated surfaces, pentacene molecules adopt a nearly standing orientation relative to the surface. The resulting “standing up” phase is comparable to the ab plane of the bulk crystal. The interplane spacing of monolayer is usually larger than that of bulk pentacene: d_{001} from 14.1 \AA to 16.1 \AA [81] due to different tilting angles of the long molecular axis. Pentacene-metal interfaces have also attracted considerable interest as electrical contacts in thin film devices. Examples of structural studies of pentacene on noble metal surfaces include pentacene on Cu(110) [82-85], Cu(119) [85], Au(110) [85-87], Ag(110) [88], Ag(111) [89-92] and Au(111) [93-95]. In contrast to its behavior on SiO_2 , pentacene adopts a flat orientation on metal monolayers and often forms

commensurate ordered overlayers.

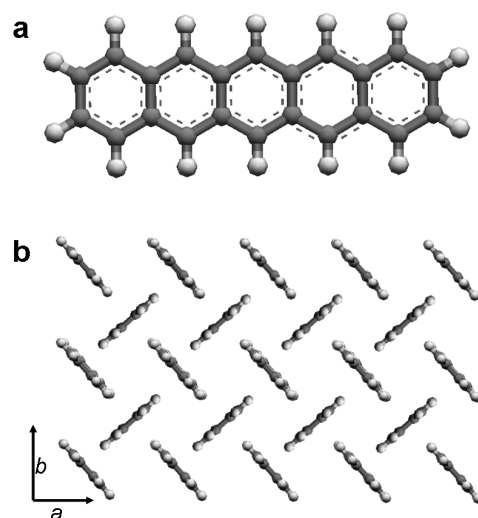


Figure 3.3 Structural models: (a) Individual pentacene molecule; (b) (110) plane of bulk pentacene shows herringbone molecular arrangement

There is an especially interesting point about the adsorption of pentacene on Ag(111). Recently, Eremtchenko *et al.* proposed a novel growth mode for this system in which an ordered second layer of pentacene forms on top of an apparently disordered first layer at 300 K [89]. In contrast to Au(111) [93-95], where a multitude of different ordered structures arise in the first layer, ordering in the first pentacene layer on Ag(111) was not directly observed at room temperature and has been reported only for cooled Ag(111) substrates [90, 92]. Kafer and Witte have questioned the interpretation of Eremtchenko *et al.* on the basis of a multi-technique study that showed significant similarities in growth mode between pentacene on Ag(111) and pentacene on Au(111) [91]. These authors suggested that the proposed ordered bilayer on Ag(111) may instead be an ordered *monolayer* similar to those seen on Au(111) [93-95]. Our experiments tried to answer the critical question raised by the disagreement in references [89]

and [91] about the initial growth mode of pentacene on Ag(111): under what conditions does long-range order exist in the first monolayer?

3.2.2. Experimental

Pentacene was evaporated in a preparation chamber (base pressure 2×10^{-9} Torr) from a boron nitride (BN) crucible in an effusion cell (Createc, SFC-40) held at a temperature of 390 K. The effusion cell was located 5 cm from the Ag substrate and 18 cm from a quartz crystal microbalance (QCM) used to monitor the deposition rate. In the present experiments, a deposition rate of 10^{-4} nm/s measured with the QCM yielded a complete pentacene bilayer in 2.0 ± 0.5 min. The absolute quantity of material deposited onto the Ag substrate at this flux was then more precisely calibrated from molecularly resolved STM images of different layers acquired at 50 K. The areal density of molecules in the first layer was 0.7–0.8 molecules/nm² and the areal density in the second layer was 0.7 molecules/nm².

All STM imaging was performed in constant-current mode with electrochemically etched tungsten tips. Tips were heated after introduction into the UHV chamber by electron bombardment. Subsequently, they were reprocessed in the STM, as needed by applying combinations of current and voltage pulsing. The sample was cooled in the STM stage to 50 ± 10 K using a continuous flow cryostat. Sample temperature was monitored with a Si diode thermometer

(Lakeshore) mounted on the STM stage near the sample plate.

STM images measured at 50 K were corrected for the thermal drift that exists due to the temperature gradient between the tip (300 K) and the sample (50 K). This was carried out by measuring the drift vector of a fixed surface feature (e.g., a step edge or point impurity) and using this vector to generate a linear transformation to correct STM images measured within 30 minute to 1 hour of the drift vector measurement. The accuracy of this procedure was confirmed with known surface structures, such as the $(2\sqrt{3} \times 2\sqrt{3})R30^\circ$ monolayer of C_{60} on Ag(111).

3.2.3. Result

3.2.3.1. Pentacene Adsorption on Ag(111) at 300K

In this section, we present data explicitly illustrating the growth of the ordered pentacene structure on Ag(111) at 300 K. Following the efforts of Eremtchenko *et al.*, [89], we address the growth in more quantitative detail. Figure 3.4.a shows an STM image measured after a 30 s exposure to pentacene, where no evidence of ordering can be seen. In Figure 3.4.b, the first signs of order are present (after a 60 s pentacene exposure) in the form of small domains (white arrows in Figure 3.4.b) near the Ag(111) surface steps. Under these tunneling conditions (-0.82V, 0.095nA), the ordered domains have comparable (or even slightly smaller) apparent heights than their immediate surroundings. This height

information is clouded by the convolution of density of electronic states and topography in STM. However, the relative apparent height is in the range observed for ordered molecular monolayers that coexist with mobile 2D gas phases [96].

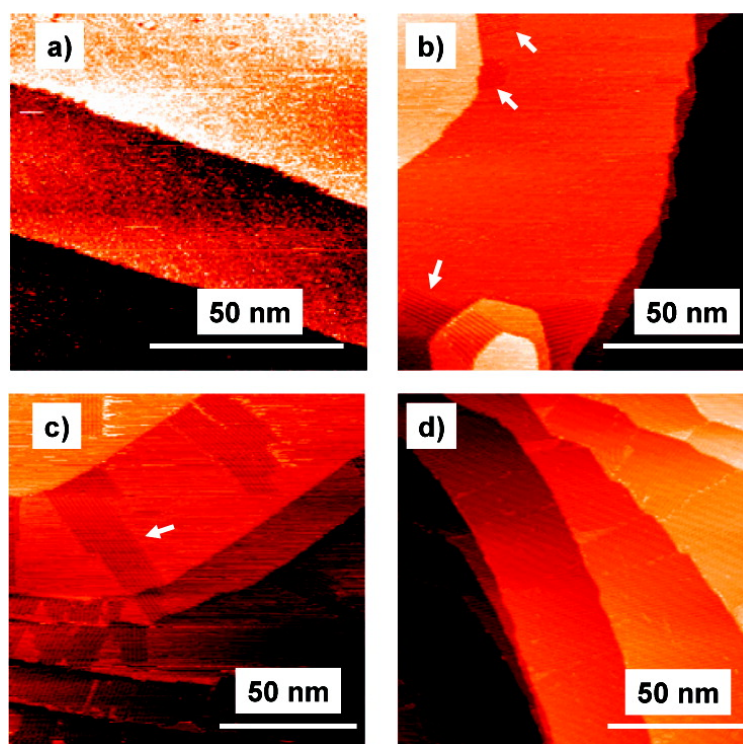


Figure 3.4 Growth of ordered pentacene on Ag(111) at room temperature for different deposition times: (a) 30 s; 2D gas; (b) 60 s; stripes appear at silver step edges (white arrows); (c) 78 s; (d) 106 s; stripes increase in area with deposition time.

Figure 3.4.c shows approximately 50% coverage by the ordered structure (78 s exposure), and Figure 3.4.d shows a nearly complete coverage of the structure (106 s exposure). In Figure 3.5, the percentage surface area covered by the ordered structure as measured from the STM images in Figure 3.4, as well as others measured during the same sequential deposition experiment, is plotted versus total deposition time. The inset of Figure 3.5 shows the same data plotted versus nominal thickness measured at the position of the QCM during the

deposition.

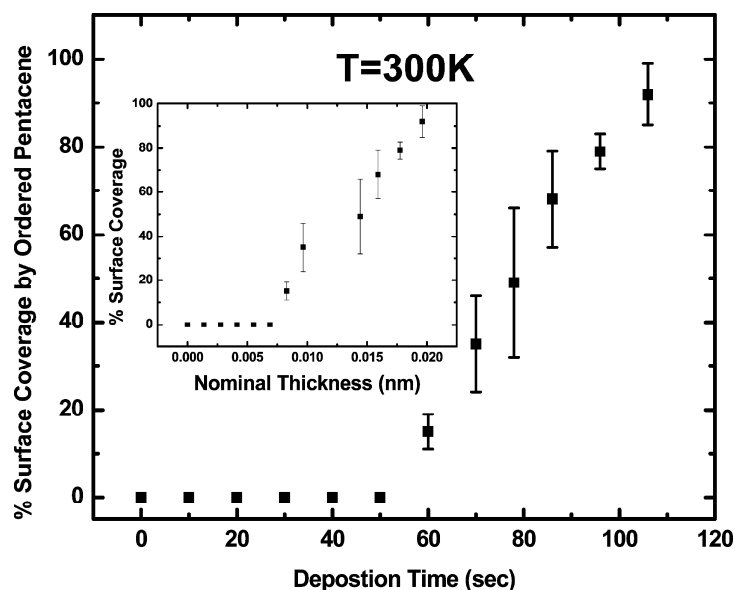


Figure 3.5 Percentage surface covered by ordered pentacene structures at room temperature as a function of deposition time under constant pentacene flux of 10^{-4} nm/s measured by QCM. This plot includes Figure 3.4 measurements and additional images acquired during the same growth experiment. Error bars represent the standard deviation of percent coverage measured in different regions of the surface (3-5 different 50-100nm regions). Inset: The same data plotted versus the nominal thickness measured with a QCM during the sequential deposition steps.

The growth of the ordered structure may thus be characterized by the minimum pentacene coverage required for nucleation (achieved at ~ 50 s deposition time) and the subsequent approximately linear growth in the fractional surface area occupied by this structure. This gradual size increase for the ordered phase strongly suggests a bilayer phase. In general, a monolayer phase transition would be expected to display a more abrupt size increase following nucleation.

3.2.3.2. Ordered Pentacene on Ag(111) at 50K

Molecular resolution was readily achieved for the pentacene bilayer regions at 300 K, such as those in the STM images in Figure 3.4.b–d. The areas surrounding these islands were observed to be either noisy or featureless, in agreement with the report in reference [89]. Also in agreement with the previous work is the observation that the bilayer nucleates in small islands at the edges of monatomic Ag steps, as shown in the STM image measured at 300 K in Figure 3.4.b.

When the sample is imaged at 50 K, the regions surrounding the small bilayer islands no longer appear featureless but, instead, show a regular arrangement of molecular-scale features, as illustrated in the STM image in Figure 3.6.a. These features are consistent in size and shape with expectations for a pentacene molecule lying flat on the Ag(111) surface [89-92]. In contrast, the appearance of pentacene molecules in the bilayer island region is narrower, consistent with the likelihood that they are tilted by $28^\circ \sim 34^\circ$ out of the plane of the surface [89, 91]. The proposed structure model is in Figure 3.6.c-d.

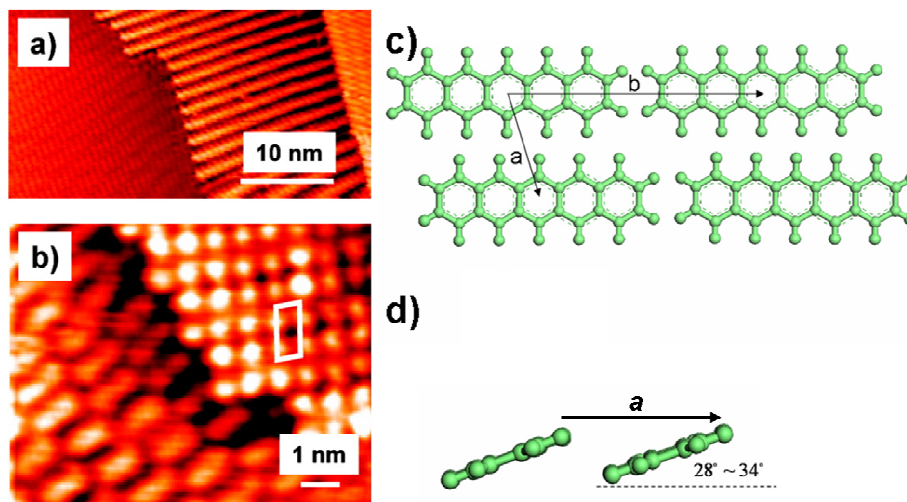


Figure 3.6(a) STM image measured at 50 K after pentacene deposition at 300 K illustrating order surrounding bilayer island edges ;(b) STM image measured at 50 K illustrating first layer molecules that are partially covered by second layer molecules near an island boundary. Note that second layer molecules (unit cell indicated by the white polygon) in this image appear as two-lobed structures. Schematic of pentacene bilayer unit cells on Ag(111): (c) Top view (d) Side view

The molecular topography along the interface between the bilayer island and pentacene monolayer confirms that the ordered structure described by Eremtchenko *et. al.* is, indeed, a bilayer, as opposed to a high-density ordered monolayer phase [89]. Most importantly, as seen in Figure 3.6.b, bilayer molecules at the edge of the island partially obscure molecules in the monolayer, definitively proving that these domains comprise a growing second layer. The double-lobed submolecular structure of each bilayer pentacene molecule in this STM image was previously reported [89] and likely reflects the nodal structure of low lying molecular orbitals of pentacene.

Away from the bilayer islands, two different monolayer phases coexist on Ag(111), as shown in Figure 3.7. Each of these two phases was observed with comparable frequency in the coverage regime we have studied (at the onset of

formation of ordered bilayer islands). Additional structures might be accessible at yet lower pentacene coverages, as reported on Au(111) [89-92].

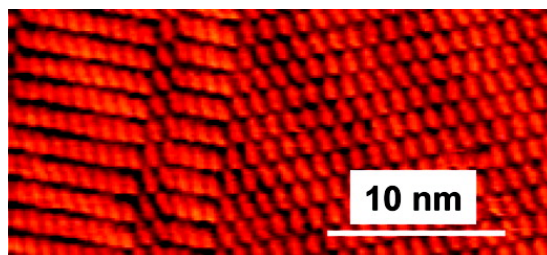


Figure 3.7 STM image measured at 50 K after growth at 300 K reveals coexistence of two different ordered monolayer phases.

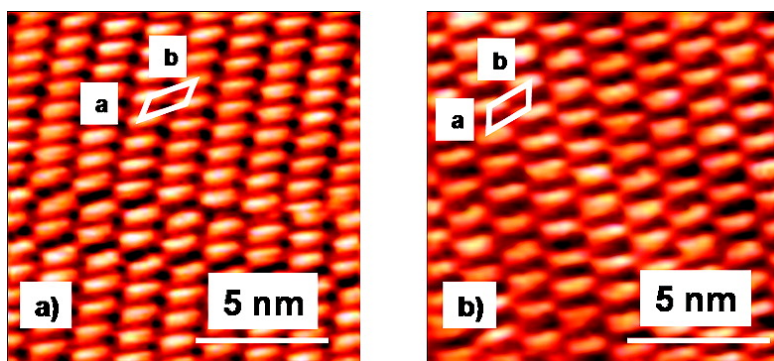


Figure 3.8(a) STM image showing a structure 1 domain with the unit cell highlighted and (b) STM image showing a structure 2 domain with the unit cell highlighted.

The ordered pentacene structure in Figure 3.8.a (structure 1) has an oblique unit cell, as indicated in the STM image. The dimensions of the unit cell are $a = 0.85 \pm 0.05$ nm and $b = 1.70 \pm 0.12$ nm with an included angle of $60 \pm 2^\circ$. The long axis of the pentacene molecules in this closely packed structure coincides with the $[1\bar{1}0]$ direction of the Ag(111) surface lattice. The error bars in the lattice parameters are the (1σ) standard deviations of a sampling of length measurements made on different unit cells (50) in several high-resolution STM images, such as Figure 3.8.a. A lower density monolayer structure (structure 2) coexists with structure 1 and is shown in Figure 3.8.b. This structure has pentacene molecules

arranged in a unit cell with dimensions $a = 1.0 \pm 0.1$ nm, $b = 1.5 \pm 0.1$ nm, with an included angle of $71 \pm 2^\circ$. The long axis of the molecule in the lower density structure (structure 2) makes an angle of 10° with the $[\bar{1}10]$ surface direction on the Ag substrate.

3.2.4. Discussion

3.2.4.1. Room Temperature Pentacene Monolayers: Order vs. Disorder

It is remarkable that STM measurements made at 300 K cannot detect topographic variations due to the presence of first layer pentacene molecules on Ag(111) (apart from a general tendency for images to be more “noisy”). This is a significant contrast to STM measurements of pentacene on other surfaces [82-86, 89-92], especially Au(111), which is structurally similar to Ag(111).

On the basis of the lack of direct resolution of first-layer molecular features at 300 K, pentacene molecules must be extremely mobile on Ag(111). Static, but disordered molecules, would still be imaged as topographic protrusions. We thus surmise that the first layer of pentacene on Ag(111) exists as a dynamically disordered 2D phase of rapidly moving molecules at 300 K [96]. Upon cooling, this “2D gas” then condenses into the ordered structures shown in Figure 3.6–3.8. We note that low energy atom diffraction (LEAD) measurements did not observe a monolayer structural transition between 200K and 50K [90]. This indicates that the ordered monolayer phases are already nucleated by 200 K and that

condensation occurs somewhere between this temperature and 300 K.

The possible influence of the STM tip on this “2D gas” must also be considered. In fact, the tip can cause significant perturbations even for strongly chemisorbed molecular layers [97]. The STM tip may enhance the mobility of pentacene molecules in the first layer on Ag(111) due to attractive van der Waals interactions that tend to lift molecules from the surface. In our experiments, the tunneling resistance was held quite high (10 G Ω) to minimize tip–sample interactions. On the basis of these conditions, it is unlikely that tip perturbations are solely responsible for the apparent dynamic disorder in the first layer. If they were, the gentle tunneling conditions we have employed would preserve some remnant indications of order that would disappear with continued STM imaging. Since this order remnant was never observed, we conclude that the first layer of pentacene on Ag(111) exists as a 2D gas phase whose mobility may be somewhat enhanced by the presence of the STM tip.

3.2.4.2. Structural Models of Pentacene Monolayer Phases

The ordered monolayer structures that we have observed at 50 K provide useful insight into the surface bonding and intermolecular interactions of pentacene on Ag(111). The unit cells for structures 1 and 2 are shown schematically in Figure 3.9. First, it is worth pointing out that the unit cell dimensions for both first-layer structures are similar to pentacene monolayer unit

cells on other surfaces [82-95]. Most significantly, structure 1 is identical to the monolayer structure of pentacene on Ag(111) observed by Danismann *et al.* after hyperthermal molecular beam growth of pentacene at 200 K [90], and structure 2 is identical to the “brick wall” structure observed using STM at 77 K by Zhang *et al.* [92]

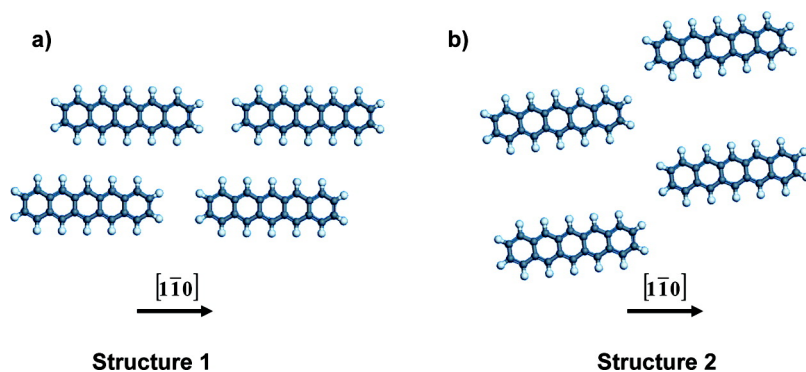


Figure 3.9 Schematic of pentacene monolayer unit cells on Ag(111): (a) structure 1 and (b) structure 2.

In general, the spacing between pentacene molecules in both monolayer structures 1 and 2 is rather large along both directions. Recently, density functional theory calculations have been carried out for pairs of coplanar pentacene molecules in an effort to understand intermolecular interactions on surfaces [98]. These calculations suggest that direct intermolecular interactions between pentacene molecules are essentially negligible at the distances observed on Ag(111). The only exception is structure 2, for which the b unit cell dimension would probably result in an attractive intermolecular interaction for an isolated dimer.

Given the large intermolecular distances and the apparent commensuration in the monolayer structures, the Ag substrate is the primary cause of monolayer

ordering at lower temperatures. This can originate from two effects: (1) direct bonding interactions between pentacene and Ag(111) and (2) indirect substrate-induced intermolecular interactions. These two effects will be addressed below.

The desorption energy for monolayer pentacene on Ag(111) has been estimated to be about 1.5 eV [91], indicating that the molecule-substrate interaction is strong enough to qualify as chemisorption. Furthermore, near edge X-ray absorption fine structure (NEXAFS) spectroscopy has shown that the molecular orbitals in the first pentacene monolayer are substantially modified by interaction with the metal surface [91]. Other details of the direct bonding interaction, such as the existence of a preferred site location, between pentacene and Ag(111) are not yet known from either experiment or calculation. Since the pentacene molecule is large and its lowest energy orbitals are significantly delocalized, more than one surface site must be considered to understand the adsorption structures. This probably contributes to the observed coexistence of different monolayer structures in our experiments and in others [93-95, 99, 100]. Since the molecule samples a number of different surface sites simultaneously, slightly different surface arrangements should result in comparable total adsorption energies.

Although the pure “through-space” component of intermolecular interactions will be weak at these spacings, substrate-mediated interactions may be significant. Now we consider the electrostatic repulsion between induced dipoles in the

adsorbed pentacene. When any nonpolar molecule is adsorbed on a surface, the intrinsic clean-surface dipole layer (due to charge “spill-out” [101]) induces a dipole in the molecule related to its polarizability. This effect is often responsible for adsorption-induced work function changes caused by nonpolar species. The repulsion between induced dipoles will favor a greater intermolecular spacing than would be expected in the absence of the silver surface [98].

Indirect interactions between pentacene adsorbates could also arise from interferences due to the scattering of surface state electrons from the molecules [102, 103] or from elastic deformation of the Ag surface [104]. A simple surface state-mediated interaction picture (which would lead to much larger pentacene spacings of 2.4 nm [102, 103]) is unlikely. Finally, the distribution of the moderate chemisorption interaction over multiple silver atoms implies negligible elastic interactions [100]. Pentacene monolayer structures, accessible only at lower temperatures, thus appear most influenced by direct bonding with the substrate atoms and substrate-induced dipole repulsion.

3.2.4.3. The Pentacene Bilayer on Ag(111)

Previous assignment of the ordered pentacene structure observable at 300 K to a pentacene bilayer is based upon the analysis of changes in High Resolution Electron Energy Loss Spectroscopy (HREELS) [89]. The STM images in Figure 3.4 offer direct structural support of this assignment.

Quantitative measures of bilayer nucleation and growth, as plotted in Figure 3.5, provide a final confirmation. The deposition time required for completion of the ordered structure (106 s) is approximately twice the time required for the initial appearance of the structure (50–60 s). Sequential layer growth of two layers with approximately equal molecular densities accounts for this growth behavior. Molecularly resolved images obtained at 50 K reveal the bilayer structure directly and allow for absolute coverage calibration. This calibration eliminates the difficulties, pointed out in reference [89], with interpreting thickness-dependent STM data using nominal exposures measured with a QCM.

The density of second-row pentacene molecules in the bilayer phase (0.7 molecules/nm²) is comparable to the densities of the “structure 2” monolayer phase (0.7 molecules/nm²) and the “structure 1” monolayer phase (0.8 molecules/nm²). This permits an absolute calibration for the constant flux growth data in Figure 3.5, where the total number of molecules on the surface increases approximately linearly with deposition time (slope 0.013 molecules/nm² s) for the entire 0–106 s deposition interval. Such linearity is expected only if the ordered structure involves bilayer formation. Upon the basis of the small difference in surface density between the bilayer and the monolayer phases, a coverage-dependent phase transition from 2D gas to striped bilayer structures would exhibit extremely nonlinear growth.

Kafer and Witte have established that thick films of pentacene on Ag(111) grow in a Stranski-Krastanov fashion, where 3D islands nucleate on top of a

uniform wetting layer [91]. We propose that this wetting layer is, in fact, the ordered bilayer described here and in reference [89]. Often, the wetting layer in SK growth is the first layer, but a wetting film can also comprise the first two layers. The second layer must simply be thermodynamically stable with respect to the formation of 3D islands.

The thermodynamic stability of the second pentacene layer is an interesting issue. Aromatic molecules have been observed to adopt bilayer structures, as in the case of benzene on Cu(111) [105] and Cu(110) [106]. In contrast, multilayer pentacene films on Au(111) dewet the surface on a 5–20 h time scale (at 300 K) [107]. In our experiments on pentacene bilayers on Ag(111), no dewetting occurred over the 48 h period of observation (at 300 K). Evidently, the pentacene bilayer films on Ag(111) are more stable than multilayer pentacene films on Au(111) [107]. The more thermally robust pentacene monolayer on gold leads to weaker interactions with subsequent pentacene layers.

Finally, an intriguing comparison is made between pentacene bilayer structures on Ag(111) and pentacene structural transformations observed on $(\sqrt{3} \times \sqrt{3})R30^\circ$ Ag/Si(111) [108, 109]. On this largely inert Ag/Si(111) surface, several recent studies have reported STM tip-induced structural changes in the first layer of pentacene [108]. The tip-induced structure appears strikingly similar to the pentacene bilayer on Ag(111) [89]. No evidence of similar tip-induced structural changes for pentacene monolayers on Ag(111) was observed. The extent of the bilayer on Ag(111) is adjusted solely by total pentacene deposition time

(Figures 3.3 and 3.4). Repeated scanning over the same pentacene monolayer region on silver did not drive bilayer formation. The similarity in appearance between the bilayer on Ag(111) [89] and the tip-induced structure on $(\sqrt{3} \times \sqrt{3})R30^\circ\text{Ag/Si(111)}$ [109] indicates similar packing densities with tilted top layer molecules. Although bilayers (on Ag(111)) and tip-induced structures (on $(\sqrt{3} \times \sqrt{3})R30^\circ\text{Ag/Si(111)}$) involve similar top-layer arrangements, the underlying surface-contacting layers may be more distinct due to different interactions with the substrates.

3.2.5. Summary

In summary, we have deposited pentacene on Ag(111) at 300 K and observed the resulting structure and morphology at this temperature and then at 50 K to determine the conditions for ordering in the first layer. On the basis of an absolute coverage calibration, we show that the first pentacene layer does not exhibit long-range order at 300 K. To create order in the first pentacene layer on Ag(111), we have cooled the surface from 300 to 50 K. This results in the condensation of two different ordered pentacene structures (structure 1 and structure 2) with flat-lying molecules arranged in oblique unit cells that are typical for pentacene on most single-crystal metal surfaces.

Room temperature order in pentacene films emerges only in the second layer. The density of pentacene molecules at the bilayer surface is the same (within

experimental error) as the density of pentacene molecules in the monolayer structure 2 observed at 50 K. Nonetheless, the detailed arrangement of first-layer pentacene molecules in the bilayer structure is distinct from the monolayer structure 2 arrangement observed at 50 K. The temperature-coverage phase diagram for pentacene/Ag(111) is summarized in Figure 3.10.

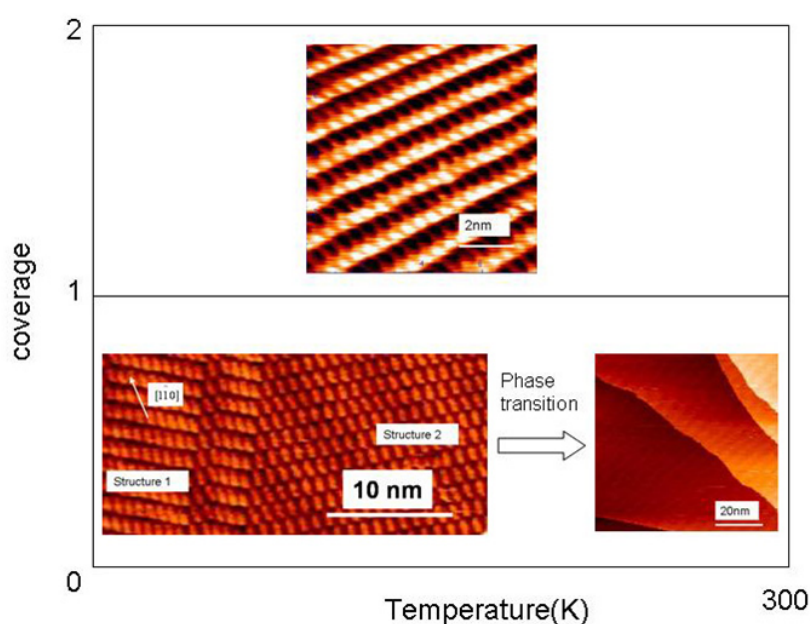


Figure 3.10 Phase diagram of pentacene on Ag(111)

Molecularly resolved images of the boundary between the pentacene bilayer and monolayer clearly show a discontinuous arrangement in the first layer molecules at the boundary. Indeed, the irregular arrangement of pentacene boundary molecules suggests that substantial disorder remains in the first layer of the crystalline bilayer. This is significant because such disorder is likely to degrade the efficiency of carrier injection at pentacene/Ag electrodes.

Finally, we re-emphasize the significance of these experiments in the context of comparison with pentacene adsorption adsorbed on other Au and Cu surfaces.

We have shown that the differences in adsorption behavior in the first layer are merely related to the enhanced mobility of pentacene on Ag(111) at 300 K as compared to other noble metals. Greater mobility implies a weaker chemisorption interaction relative to Au and Cu surfaces. When this mobility is suppressed by cooling, ordering in the first layer occurs, resulting in structures that are qualitatively similar to other known pentacene monolayer structures. The formation of a complete and ordered second layer starting from a disordered first layer is unique to pentacene on Ag(111). This scenario, first proposed by Eremtchenko *et al.* [89], was discounted by Kafer and Witte [91]. The present STM studies provide very direct evidence supporting this remarkable growth mode.

3.3. Neat Zinc Phthalocyanine (ZnPc) and Perfluorinated Zinc Phthalocyanine (F₁₆ZnPc) on Ag(111)

3.3.1. Introduction

Metallophthalocyanine (MPc) molecules are molecular semiconductors with a planar structure consisting of aromatic macrocycles with a centrally coordinated metal atom. These highly stable molecules absorb light efficiently and are stable with high symmetry, planarity and electronic delocalization [110]. These properties are

useful for technological applications, including chemical sensors, optical devices, solar cells and photosensitizers for medical treatment.

One of the advantages of metal phthalocyanines is their electronic properties can be tuned by chemical substitution. Phthalocyanines are typically hole transport materials [110] (i.e. donors), but they can be made into electron transport materials by simple chemical exchange of the hydrogen atoms with fluorine atoms [111]. Theoretical calculations and electrochemical measurements show that alkyl- or halide- substitution of terminal hydrogen changes the ionization energies over a broad range, with the molecular HOMO-LUMO gaps largely unchanged [112]. In Figure 3.11, the molecular structures, theoretical ionization energies, and affinities for individual ZnPc and F₁₆ZnPc molecules are displayed [112]. Quantum chemical calculations reveal HOMO's and LUMO's as single and doubly-degenerate π orbitals, respectively [113].

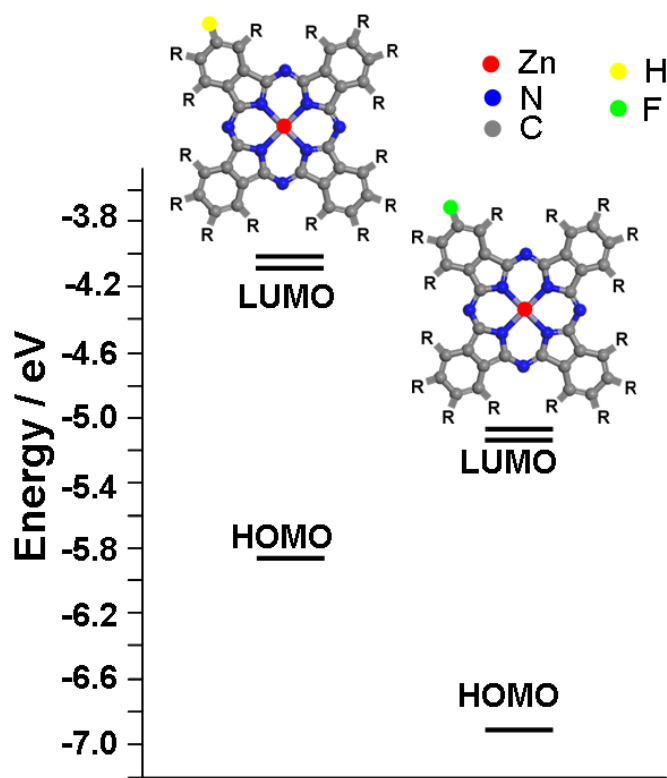


Figure 3.11 Molecular structures of zinc phthalocyanine and perfluorinated zinc phthalocyanine and ionization energies and electron affinities from PM3-MO calculation.

Most MPCs crystallize in a monoclinic lattice with a characteristic herringbone-type packing of the molecules. A large variety of polymorph forms have been reported: the differences between them are (i) the tilt angle of the molecules within the columns and (ii) the mutual arrangement of the columns [114]. The two most common polymorph forms are: the α -polymorph [115] and the β -polymorph [116], as shown in Figure 3.12. The degree of overlap of adjacent molecules is different in these molecular columns. The molecular interactions have thus been thought to be larger in the β -polymorph, the stable form, than in the α -polymorph, the metastable one. By thermal treatment the α -phase can be transformed to the β -phase [117]. The replacement of the central

atom slightly modifies the electronic properties of the materials, while the structure parameters for the polymorph are largely unchanged [113, 118].

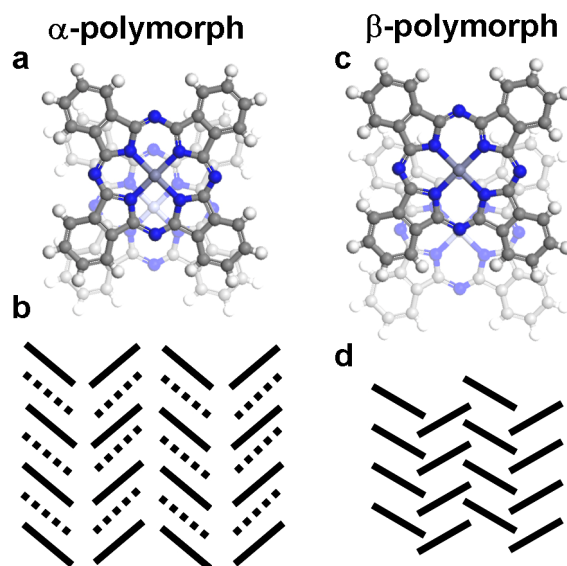


Figure 3.12 Superposition of successive phthalocyanine molecules in a molecular column along the b axis: (a) α -polymorph; (b) projection on (100) in α -polymorph; (c) β -polymorph; (d) projection on (001) in the β -polymorph. The differences between α and β -polymorph are (i) the tilt angle of the molecules within the columns and (ii) the mutual arrangement of the columns.

Due to the pronounced anisotropy of the optical and electro-optical properties of bulk MPc, there is a large interest in growing ordered and highly oriented films with a well defined and stable phase. The growth and morphology of MPc thin films have been studied on a number of different substrates including alkali-halide substrates [119, 120], ITO [121], oxidized Si [121], polycrystalline gold [121], HOPG, MoS₂ [122], Au(111) [123-127], “5×20” Au(001) [128-130], and Ag(111) [131-134]. The orientation of the molecules on the substrate is determined by the relative strengths of the molecule-molecule versus molecule-substrate interactions [121].

For alkali-halide substrates, it was found that the MPc-substrate interaction is dominated by electrostatic forces between the MPc metal ion and the anion in the substrate surface leading to planar adsorption geometry. The packing density of the MPc molecules within the first monolayer is maximized by small rotations of the molecules around an axis normal to the molecular plane and the substrate surface. In the case of metal substrate, the π - π interactions between the molecule and metal substrate also result in a planar adsorption [115, 135]. For both cases, the high packing density of MPc monolayers exceeds that of any crystallographic plane in the bulk structure. When these compressed monolayers are used as a support for the growth of multilayers, a significant amount of stress builds up, and above a critical thickness the ordered multilayers become unstable with respect to the formation of 3D islands [119, 120].

When the strength of the interaction between the substrate and the deposited molecules is reduced, the growth mode is significantly affected. On H-terminated Si(001)-(2 \times 1) surfaces, CuPc molecules adopt nearly upright orientation and co-facially stack into columns due to negligible substrate interaction [136].

CuPc and ZnPc (Figure 3.11) are the most common molecules used in organic solar cells and have very similar properties. We choose to study ZnPc since the close shell (d^{10}) configuration of the central Zn^{2+} ion results in optical spectra that is not complicated by additional bands. The goal is to compare hole and electron transport materials. The molecules have the same footprint and are often assumed

to provide similarly structural films. Here we see that peripheral atoms strongly affect monolayer structures.

3.3.2. Experimental

ZnPc and F₁₆ZnPc were deposited onto Ag(111) from two BN crucibles at 660 K and 680 K. The typical rate was 0.25 ML/min. After deposition the samples were transferred under vacuum to the STM.

3.3.3. Result and Discussion

3.3.3.1. ZnPc/Ag(111)

Two ZnPc monolayer structures, with distinct structures and stabilities, are readily observed. ZnPc deposition on a room temperature Ag(111) substrate results in the direct formation of an ordered ZnPc film with a density of 0.51 molecules/nm². As shown in Figure 3.13.a, this low-density monolayer (LD-ZnPc) has an oblique lattice with parameters $a = 1.56 \pm 0.02$ nm, $b = 1.25 \pm 0.02$ nm with an angle $\theta = 83 \pm 2^\circ$. The lattice vector a is along the silver surface close packed $[1\bar{1}0]$ direction. The submolecular resolution image (Figure 3.13.a inset) reveals the 22° rotation of the molecular mirror plane M_I (phenyl bisector) with respect to the lattice vector a . The point-on-line registry of this film with the

substrate generally indicates a weak energetic interaction between ZnPc and Ag(111).

A more stable high density phase (HD-ZnPc) is obtained upon annealing this LD-ZnPc film to 400 K for 15 min, (Figure 3.13.b). In the HD-ZnPc phase, molecules pack with a density of 0.55 molecule/nm², an increase of 7% from the LD-ZnPc phase. The HD-ZnPc phase also possesses higher symmetry, displaying (within experimental error), a square lattice with the lattice vector $a = 1.35 \pm 0.03$ nm, $b = 1.33 \pm 0.02$ nm, and an internal angle of $\theta = 88 \pm 3^\circ$. The angle between the vectors a and the mirror M_I is about 35° . The molecular packing arrangement is provided in Figure 3.13.c. Like the LD-ZnPc phase, the higher density phase displays a point-on-line registration, with the a lattice vector aligned along the substrate $[1\bar{1}0]$ direction.

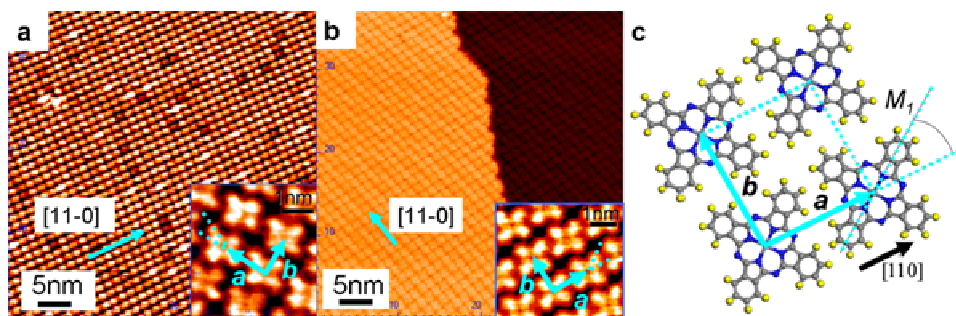


Figure 3.13 (a-b) STM images of ZnPc monolayer structures. Insets show higher resolution images and unit cells for each structure. (a) Metastable low-density phase, produced by deposition on room temperature substrate; (b) Stable high-density phase, produced by vacuum deposition and annealing to 400K. Both monolayers have point-on-line registration to substrate. (c) Structural model

Both ZnPc monolayers, the metastable LD-ZnPc phase and the stable HD-ZnPc phase, are similar to those observed for CuPc on Ag(111) [134]. In the structural transformation from the LD- to HD- phase, the molecular axes M_I and

M_2 are rotated with respect to the lattice vectors a_1 and b_1 increasing the van der Waals contact with neighboring molecules, accounting for the greater stability of the HD phase.

3.3.3.2. $F_{16}\text{ZnPc}/\text{Ag}(111)$

At $F_{16}\text{ZnPc}$ coverages <0.6 ML, no ordered monolayer structures are observed. Increasing the coverage to $\gtrsim 0.6$ ML results in $F_{16}\text{ZnPc}$ island formation with the ordered molecular arrangement shown in Figure 3.14.a. Higher magnification images (Figure 3.14.b) reveal molecules are organized in two alternating double molecular rows, labeled as “A” and “B”, along the $[\bar{1}10]$ direction as indicated by the arrow. Within A (and B) molecules adopt the same in-plane orientation. The unit cell for this film is correspondingly large ($a = 1.50 \pm 0.02$ nm, $b = 6.55 \pm 0.03$ nm, $\theta = 81 \pm 3^\circ$), as highlighted on the image. Molecular models of the A and B double row structures are provided in Figure 3.14.c. Rows A and B display comparable molecular packing densities of 0.41 molecules/nm². Both rows show a 1.50 nm $F_{16}\text{ZnPc}$ molecular spacing along the substrate $[\bar{1}10]$ direct. Row A has a nearly rectangular molecular arrangement, with an internal angle of $\theta = 84 \pm 3^\circ$, giving an $F_{16}\text{ZnPc}$ next-nearest neighbor distance of 1.63 ± 0.2 nm. The molecular symmetry axis M_1 is rotated 33° from lattice vector a . Row B has a more oblique molecular arrangement, with an internal angle of $65 \pm 3^\circ$ and an $F_{16}\text{ZnPc}$ next-nearest neighbor distance of

1.75 ± 0.2 nm. Consequently, rows A and B have comparable ZnPc packing densities. Similarly ordered double-row molecular arrangements are observed for $F_{16}\text{CuPc}/\text{Ag}(111)$ [137], $F_{16}\text{CuPc}/\text{Cu}(111)$ [138], and vanadyl phthalocyanine (VOPc) on cobalt (II) phthalocyanine (CoPc) monolayer/ $\text{Au}(111)$ [139] and are attributed to electrostatic repulsion between neighboring molecules. Alternating rotation of the molecules between rows minimizes electrostatic repulsion [138].

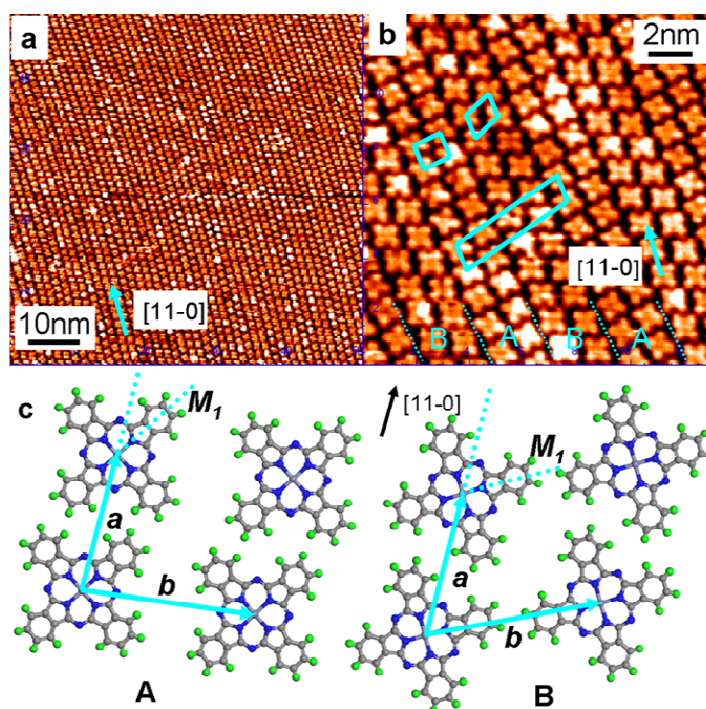


Figure 3.14 (a-b) STM images of $F_{16}\text{ZnPc}$ monolayer. Film consists of alternating double row structures, labeled A and B. Unit cell (large parallelogram) has parameters $a = 1.50 \pm 0.02$ nm, $b = 6.55 \pm 0.03$ nm, $\theta = 81 \pm 3^\circ$; (c) Molecular packing in the two double row structures A and B. Rows A: Rectangular arrangement with 1.50 nm and 1.68 nm nearest- and next-nearest-neighbor molecular spacings; Rows B: Oblique arrangement with 1.50 nm and 1.72 nm nearest and next-nearest neighbor molecular spacings and an internal angle of 65° .

3.3.4. Summary

Single component ZnPc and $F_{16}\text{ZnPc}$ films follow structural trends

established for MPc film growth on a variety of substrates including HOPG [140], MoS₂ [122], Au(111) [123, 125], “5 × 20” Au(001) [128, 129], and Ag(111) [134, 137]. On these surfaces, MPc molecules also readily form ordered structures that are incommensurate with the substrate. The monomolecular arrangement in these incommensurate phases is largely dictated by the molecule-molecule interaction. For F₁₆ZnPc, alternatively arranged double-molecular-rows form along the $\bar{1}10$ direction of Ag(111). Within the same double-molecular-row, all F₁₆ZnPc molecules possess the same in-plane orientation. The molecules in the neighboring double-molecular-rows, however, adopt different in-plane orientation. This can be understood in terms of minimization of the repulsive intermolecular electrostatic force between molecules.

4. Chapter 4 Binary system: Pentacene: C₆₀

As described in Chapter 3, pentacene has rich phase behavior on Ag(111) allowing us to “engineer” film structure via growth conditions. Three distinct binary molecular films will be discussed in this chapter: (1) pentacene standing up on C₆₀ monolayer; published in Applied Physics Letters (D. B. Dougherty, W. Jin, W. G. Cullen, J. E. Reutt-Robey, and S. W. Robey, *Striped Domains at the Pentacene:C₆₀ interface*, Applied Physics Letter, 2009, **94**: p.023103); (2) C₆₀ linear chains on the pentacene crystalline bilayer; published in Physics Review B (D. B. Dougherty, W. Jin, W. G. Cullen, G. Dutton, J. E. Reutt-Robey, and S. W. Robey, *Local Transport Gap in C₆₀ Nanochains on a Pentacene Template*, Physics Review B, 2008,**77**: p.073414); (3) C₆₀-pentacene co-crystalline network by depositing C₆₀ on pentacene 2-D gas, published in Langmuir (W. Jin, D. B. Dougherty, W. G. Cullen, S. W. Robey, and J. E. Reutt-Robey, *C₆₀-Pentacene Network Formation by 2-D Co-Crystallization*, Langmuir, 2009,**25(17)**: p.9857)

4.1. Pentacene Standing Up on C₆₀ Monolayer

4.1.1. Introduction

A major motivation for the development of electronic devices based on

organic materials is their mechanical flexibility. This property is valuable for the design of durable devices, sometimes in unique formats such as “electronic paper” [141]. Mechanical flexibility arises microscopically from interactions between the constituent molecules that are significantly weaker than covalent or ionic interactions in most inorganic materials [142]. These weak intermolecular interactions suggest that reconstructions of surfaces and interfaces of organic materials may be very common and potentially dramatic. Large numbers of relatively low energy degrees of freedom can lead to complicated molecular structural motifs at interfaces with attendant complications to the interfacial electronic level arrangement.

An example of complicated interfacial interactions is found in recent x-ray diffraction measurements that indicate the restructuring of several layers of perfluorinated copper phthalocyanine induced by formation of an interface with di-indenoperylene [143]. Such heterojunctions between different organic materials are increasingly technologically relevant in optoelectronic devices [54]. In these devices, the ability of an exciton to generate a photovoltage upon dissociation is related to the efficiency with which it can reach an interface and the efficiency of charge separation at the interface. Optimizing interface morphology for these processes is a necessary step in optimizing device performance. The objective of the work to be described in this section is to illuminate the initial stages of growth of pentacene:C₆₀ junctions, as recently employed in organic photovoltaic cells [25-28]. I demonstrate a case where weak interactions facilitate the development

of extended defect structures in the nanoscale film morphology driven by interfacial stress at a junction between two different organic semiconductors.

4.1.2. Experimental

A uniform single layer of C_{60} was grown on the Ag(111) surface by depositing a multilayer film of C_{60} from an effusion cell (Createc LTC-40) and then annealing at ~ 500 K. The result was a perfect and complete $(2\sqrt{3} \times 2\sqrt{3})R30^\circ$ overlayer of C_{60} [66]. Pentacene was deposited onto the C_{60} monolayer (held at room temperature) from a separate effusion cell (Createc SFC-40). To minimize damage to the pentacene films and preserve their structural integrity, local electronic properties were measured using constant-current distance-voltage spectroscopy $z(V)$ [43, 144].

4.1.3. Result

The STM image in Figure 4.1.a shows a large scale view of a pentacene island on 1 ML $C_{60}/Ag(111)$. The large "butterfly" shape island is typical for pentacene on the C_{60} monolayer, reflecting pentacene's appreciable diffusion length on the C_{60} sublayer. Images additionally show a pronounced triangular pattern, arising from edge dislocations in the underlying Ag(111) support film. In the following, I will show that these dislocations do not significantly affect the

organization of the pentacene layer.

The apparent height of the pentacene islands above the surrounding C₆₀ monolayer was measured as 1.2±0.2 nm based on an average of 19 different line profiles measured across different island edges on different days (e.g. Figure 4.1.b and 4.1.c). The variations in apparent height occur as a result of common (but unknown) variations in tip work function that influence the local tunneling barrier. Despite this minor effect, the correspondence between the physical length of the pentacene molecule and the observed magnitude of its apparent height is a strong indication of a “standing up” layer of pentacene on C₆₀ [145, 146], consistent with a relatively weak, non-specific interaction between the two different organic molecules. This height is slightly smaller than that typically reported for upright oriented pentacene films, possibly suggesting an increased tilt of the long axis away from the surface normal. However, electronic factors can also influence apparent height variations in STM due to molecular resonances and tip work function.

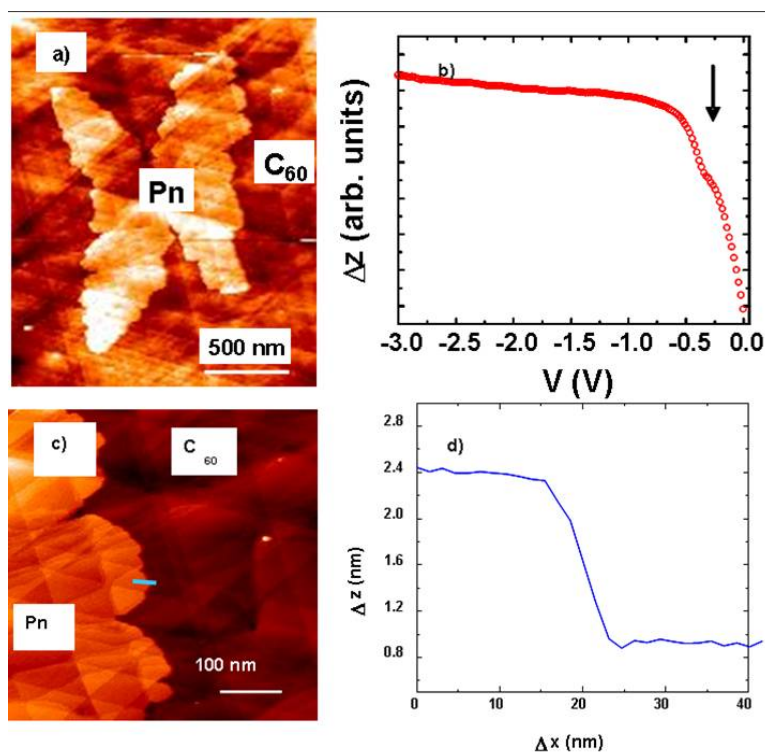


Figure 4.1 (a) STM image showing a pentacene island on top of 1 ML $C_{60}/Ag(111)$. (b) Distance-voltage characteristic (average of 13 sweeps measured at different locations) for a pentacene island. HOMO-derived structure is marked by the arrow. (c) STM image showing the edge of a pentacene island on 1 ML C_{60} . (d) Line profile across the point on the island edge indicated by the blue line in (c)

Additional support for a nearly upright molecular orientation for pentacene is found in the fractal shape observed for pentacene islands on C_{60} (Figure 4.1.a). The island shape is similar to that observed for pentacene thin film growth on SiO_2 [79] where pentacene grows by diffusion limited aggregation and the molecules orient standing up [147] in the well known thin-film phase. This nucleation behavior and the resulting island shape occur on substrates that interact relatively weakly with the π electrons in pentacene. Based on the large scale similarities between Figure 4.1.a and pentacene island shapes observed for other weakly interacting substrates, it can be inferred that the microscopic pentacene-pentacene interactions within the island and arrangement of pentacene

molecules are likely very similar to the thin film structure on SiO₂.

Further insight on the standing pentacene layer is provided by STM images of higher magnification. As shown in Figure 4.2.a-b, the pentacene layer exhibits a unique mesoscale surface pattern of striped domains above the C₆₀ sublayer. Here extended bright regions are seen to meander on the surface, approximately parallel to one another. They are separated by somewhat wider regions with an apparent height that is ~ 0.04 - 0.06 nm lower than the bright regions. The spacing between bright domains is remarkably uniform and has been measured to be 8 ± 1 nm based on an average of 100 different measurements of the spacings between parallel bright domains on different surface regions. Similarly, the width of the bright domains is consistently measured as 3.6 ± 0.6 nm. Surprisingly, the striped domains are not strongly affected by the morphology of the Ag(111) substrate, as shown by the large scale STM image in Figure 4.2.b. Stripes extend for distances >500 nm crossing Ag monatomic steps and triangular dislocations without interruption. The bright regions may be viewed as "defected" regions of the pentacene monolayer, while the darker regions represent pentacene regions with ideal ordering.

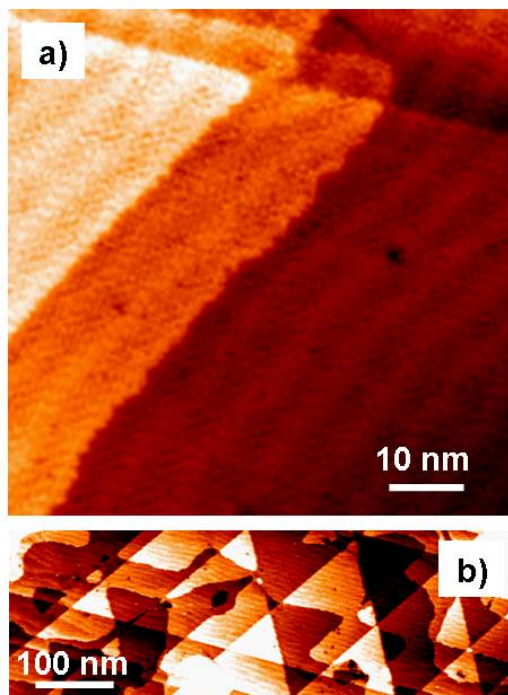


Figure 4.2 (a) STM image of pentacene on C_{60} showing several parallel bright stripes meandering on the surface. (b) Large scale STM image showing a parallel array of bright domains extending over large distances and over numerous monatomic Ag surface steps

Regions with ideal pentacene ordering are examined with higher resolution in Figure 4.3.a. In this image, we superimpose markers for the C_{60} sublayer (green circles) and the pentacene standing phase (blue lines). Pentacene positions are taken as the standing-phase a - b parameters reported for pentacene/ SiO_2 [148]. The molecular scale contrast in the STM image reflects the mismatch in the C_{60} sublayer and the pentacene ab plane. Tunneling conductance along the pentacene axis is low [149] and dominated by the local pentacene- C_{60} “contacts”, introducing topographic variations even in the ideal pentacene- C_{60} regions. Bright spots represent good contacts and therefore have the symmetry of the C_{60} sublayer. Such contrast is reminiscent of other standing organic monolayer phases [150].

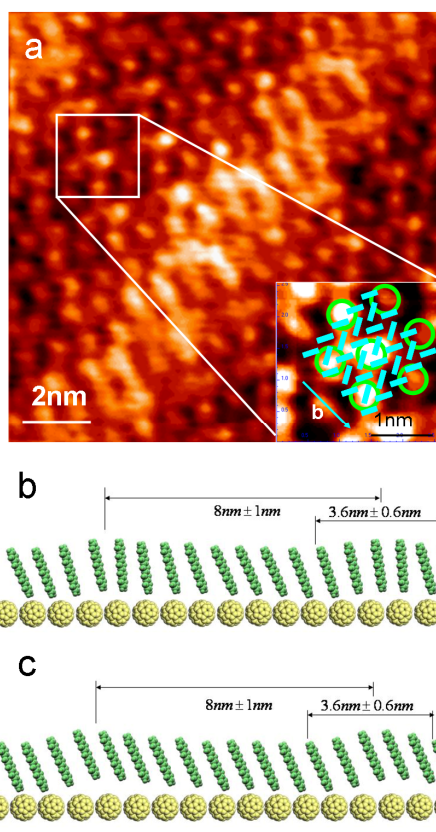


Figure 4.3 (a) STM image of pentacene on C_{60} showing molecular scale features; inset: overlay of a possible registry between standing pentacene molecules (blue lines) and the C_{60} sublayer (green circles). Schematic model of the vertical defects in the pentacene overlayer due to: (b) Changing tilt angle. (c) Rigid shift

4.1.4. Discussion

It is instructive to compare the bright striped domains for pentacene/ C_{60} films to the localized “sliding defects” reported by Kang *et al.* for pentacene adsorbed on a benzenethiol self assembly monolayer (SAM) [145]. The apparent height in STM in both cases is about 0.05 nm. The localized defects for pentacene on benzenethiol were attributed to vertical displacement of pentacene molecules compared to their immediate surroundings. This could arise from a change in the angle that the molecular long axis makes with the surface normal (Figure 4.3.b) or a rigid motion of a pentacene molecule (Figure 4.3.c). Naively interpreting the

apparent height difference between different domains as the result of such a rotation implies a change in angle of about 3° . This is consistent with angular changes observed in preliminary semi-empirical energy minimization calculations of the restructuring of C_{60} -pentacene interfaces [151].

At the pentacene/benzenethiol interface, the sliding defects are relatively "point-like," occupying small areas and nucleating at random locations in the pentacene film [145]. In the case of the pentacene layer on $C_{60}/Ag(111)$, the periodic domain structure indicates a spatially correlated condensation of defects. While both interfaces contain vertically displaced pentacene, the displacement propagates only on C_{60} .

Defect features at the pentacene: C_{60} interface may impact electrical transport in the pentacene layer or charge separation at the interface. Theoretical calculations have suggested that sliding defects for pentacene on benzenethiol would introduce shallow trap states broadened by about 0.1 eV compared to states in the defect free regions [145]. Within the resolution of the tunneling spectra (Figure 4.1.b), there are no significant differences in the electronic spectrum over the ideal regions compared to the defective regions of the pentacene film. This is consistent with distortions within the film that produce only minor (~ 0.1 eV) modifications to the electronic structure.

The likely origin of the extended defect domains for pentacene grown on $C_{60}/Ag(111)$ is stress in the pentacene film due to interactions with the C_{60} sublayer. Spontaneous formation of striped stress domains has been predicted

based on elasticity theory [152] and observed for a number of systems. These include Pb–Cu(111) surface alloys [153] and the p(2×1)-O–Cu(110) added row reconstruction [154]. The latter case shares the feature in common with pentacene/C₆₀ that stripes of the Cu–O added rows extend over large distances independent of substrate morphology.

Even though the interaction of C₆₀ with the pentacene molecule is not strong enough to force a flat-lying geometry, the C₆₀ monolayer is expected to establish a strong potential corrugation in the plane of the surface. This is especially important on Ag(111) where there is charge transfer from the metal to the fullerene [155, 156]. Since the lattice mismatch between the C₆₀ sublayer and the pentacene *ab* plane is large (~20%–40%), the sublayer will exert forces that distort the pentacene overlayer from the bulk-like geometry. The formation of domains of defects can act to relieve this substrate induced stress. The striped morphology indicates an anisotropy in the surface stress that is expected based on the anisotropy of the projected unit cell of the *ab* plane of pentacene [148]. This will lead to facile domain wall formation along one direction and/or anisotropic elastic constants in the layer.

Quantification of the influence of interface stress is difficult in this case due to incomplete knowledge of the elastic properties of pentacene films and the microscopic structure of the defective regions. Nevertheless, we can use continuum theory to assess a stress-induced origin of the stripes. The distance between stress domains l is given by [152], $l = 2\pi a e^{(\beta/C_2)+1}$, where β is the

domain wall free energy per unit length, C_2 is related to the elastic constants of the material, and a is a microscopic cutoff for the effective domain wall width [157].

The formation of the striped domains for pentacene: C_{60} at room temperature relies on the weak interactions between pentacene molecules that lead to the existence of a relatively low energy structural defect (small β). We assume that the $e^{(\beta/C_2)}$ is near unity to obtain an upper bound on the microscopic cutoff length of about 0.5 ± 0.1 nm. This is consistent with the interpretation that the transition between domains occurs by relative vertical sliding and/or changes in angle with the surface normal since these can easily occur over such short distances.

4.1.5. Summary

In conclusion, we have used STM to observe an extraordinarily long range modulation of interface morphology for single layer pentacene islands grown as a standing phase on 1 ML $C_{60}/Ag(111)$. Striped domains arise to relieve stress in the pentacene film due to interactions with the underlying C_{60} . These defects involve small vertical displacements from the C_{60} substrate. The observations described here suggest that a facile route to exerting control over nanoscale interface morphology is to carefully engineer stress relief patterns at soft interfaces.

4.2. C₆₀ Chains on Pentacene Bilayer

4.2.1. Introduction

A promising approach to nanostructuring surfaces is to fabricate molecular surface architectures that can template functional components into prescribed configurations. Beyond developing template materials and fabrication methods, it is necessary to establish correlations between real-space structure and electronic properties for both the template and the functional components. Electronic band alignment is an important consideration for most electronic devices and controlling it through structural manipulations at the nanometer-scale is technologically desirable.

Organic molecules are good candidates for carrying out templated nanostructuring since they readily self-assemble and their interactions can be tuned by chemical functionalization. Exerting control of molecular size, shape, and interactions is likely to translate into considerable control over the structure and function of templated molecular assemblies. Several studies have demonstrated the value of this approach on surfaces, focusing primarily on methods of template formation [158-163]. In this section we aim to provide local structural and spectroscopic information that can be used to begin to develop crucial structure/function correlations for molecular nanostructures at surfaces.

Recently, there have been several reports of the formation of linear fullerene nanostructures on surfaces [164-167]. Linear structures could be valuable in

device fabrication since they can fit into regions relatively densely-packed with other structures. This geometrical arrangement is difficult to achieve however, since interactions between C_{60} molecules tend to lead to hexagonal packing with about 1 nm spacing between molecules [60]. The formation of linear fullerene structures therefore usually requires the use of a template like a vicinal surface [164, 165], i.e., surfaces which have small deviations from the most symmetric crystallographic planes.

In this section, we describe a linear templating effect when small quantities of C_{60} are deposited onto an ordered bilayer of pentacene on Ag(111).

4.2.2. Experimental

Pentacene was evaporated onto the Ag(111) surface from an effusion cell (Createc SFC-40) and the formation of an ordered bilayer was verified by STM. C_{60} was then evaporated onto the bilayer from a different effusion cell (Createc LTC-40). Spectroscopy was performed in constant-current distance-voltage mode ($z(V)$).

4.2.3. Results and Discussion

4.2.3.1. Structure Properties

Figure 4.4.a shows an STM image of an isolated C_{60} molecule adsorbed on

the ordered pentacene bilayer on Ag(111) [89, 168]. As we discussed in Chapter 3, the pentacene bilayer displays long range order with an oblique unit cell that is highly anisotropic (highlighted in Figure 4.4.a), giving rise to “pentacene rows” spaced by 1.6 nm. The pentacene molecules in these rows are oriented with their long axes parallel to the plane of the substrate and their short axes tilted by $\sim 28^\circ \sim 34^\circ$ out of plane, as the structure model proposed in Chapter 3. At low coverage, subsequently deposited C_{60} molecules always locate between adjacent pentacene rows as shown in Figure 4.4.a. The observation of isolated molecules on the pentacene bilayer shows that the mobility of C_{60} on pentacene is significantly smaller than its mobility on most metals, where isolated molecules are not observed at room temperature due to rapid island formation [60, 66].

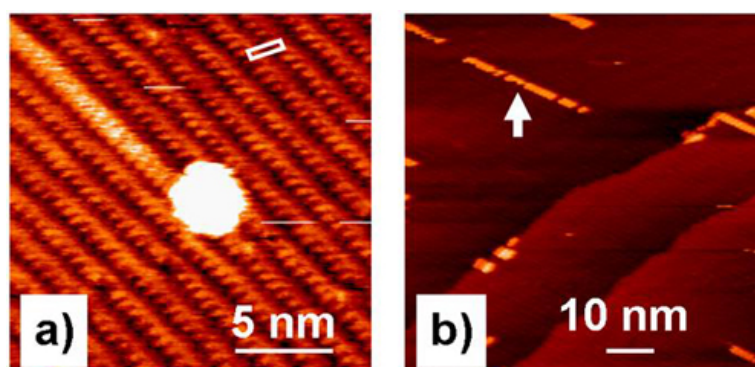


Figure 4.4 (a) STM image of an isolated C_{60} molecule (apparent height of ~ 0.5 nm above the pentacene substrate) on pentacene bilayer. The apparent lateral dimension of the C_{60} molecule is exaggerated due to the convolution of the real shape of the molecule with the shape of the STM tip; the unit cell of pentacene bilayer is highlighted; (b) Large scale STM image illustrating the formation of linear C_{60} structure (white arrow) on the pentacene bilayer.

As illustrated in the STM images in Figure 4.4.b, the pentacene row direction is transmitted to extended linear fullerene structures that appear as the bright lines running along the rows. The maximum length of such structure is expected to be

limited primarily by the width of the terrace on which they form. The maximum (defect-free) length that we have observed is about 30 nm. These linear structures are only formed on the surface at the very low-coverage regime. When the coverage of C_{60} exceeds ~ 0.05 molecules/nm², a disordered phase, meandering chains, preferentially forms as shown in Figure 4.5.a-b. Similar structures are also observed when C_{60} molecules are deposited on a zinc phthalocyanine (ZnPc) monolayer and on α -sexithiophene [169]. The details will be discussed in chapter 5.

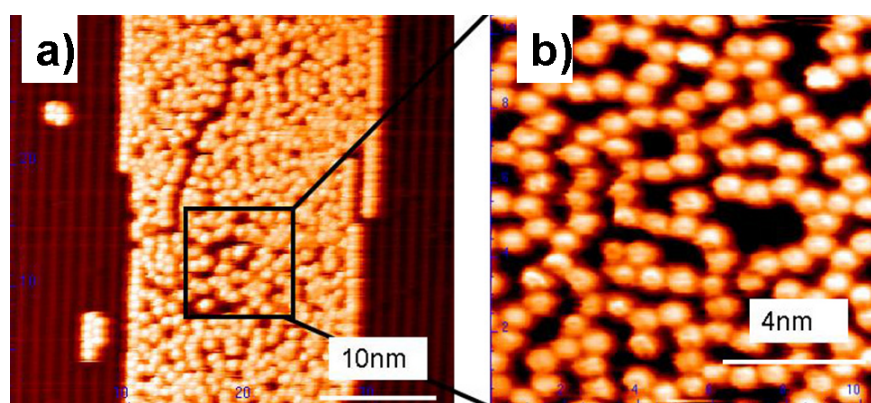


Figure 4.5 (a) STM image showing the disordered C_{60} phase confined in linear C_{60} chains; (b) STM image showing the C_{60} meandering chains.

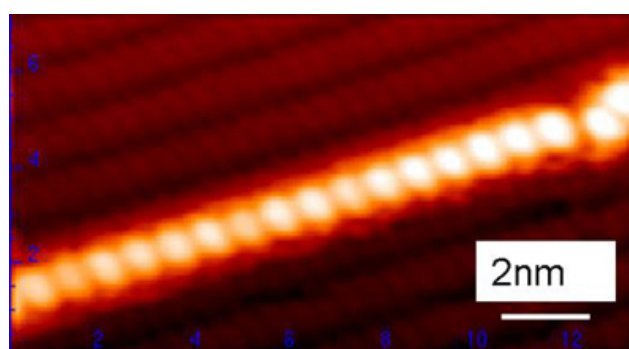


Figure 4.6 STM image showing a linear C_{60} structure with molecular resolution.

Figure 4.6 shows an STM image of a linear C_{60} structure where individual fullerene molecules can be resolved. Along the chains, molecules are separated by

the typical 1.0 nm spacing that is determined by C_{60} - C_{60} interaction [60]. Like the isolated C_{60} molecules, the chains are located in the trough between two pentacene rows. The highly specific inter-row location of C_{60} on the pentacene bilayer is driven by intermolecular interactions between C_{60} and pentacene that include both electrostatic and dispersive contributions. The first nonzero moment of C_{60} is the octapole moment, which is based upon electron deficient pentagons (*vide infra* single C-C bonds) and electron-rich hexagons (*vide infra* delocalized double C-C bonds) [170, 171]. As a planar aromatic molecule, pentacene possesses an appreciable quadrupole moment due to the electron deficient carbon framework sandwiched between the electron-rich π clouds. Consequently, the adsorption configuration of C_{60} on pentacene will be driven by the minimization of electrostatic repulsions between the C_{60} hexagons and the aromatic electron cloud of the underlying pentacene. In Figure 4.7, we show a schematic model of the local arrangement between a C_{60} and a pair of pentacene molecules representing different bilayer rows.

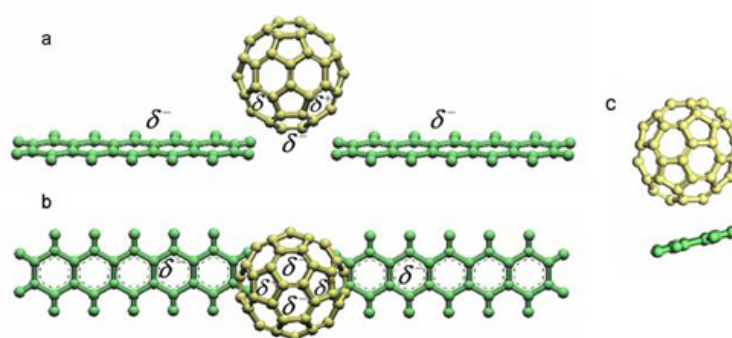


Figure 4.7 Schematic model of the arrangement of a C_{60} molecule on the pentacene bilayer; (a) Side view; (b) Top view; (c) Side view.

4.2.3.2. Spectroscopy

Figure 4.8.a and 4.8.b provide tunneling spectroscopy in $z(V)$ mode for the pentacene bilayer and C_{60} nanochains respectively. In Figure 4.8.a the spectra display resonant features near -2.0 ± 0.2 eV and 1.6 ± 0.1 eV that are associated with tunneling through the pentacene HOMO and LUMO, respectively. These values yield a peak to peak transport gap of 3.6 ± 0.3 eV. Figure 4.8.b shows resonant features at -2.2 ± 0.2 eV and 2.3 ± 0.1 eV, yielding a transport gap of 4.5 ± 0.3 eV. Tunneling spectra obtained for C_{60} chains with lengths ranging from 10 to 30 nm yielded no significant difference. All chains were lengthwise sampled to within 3 nm (approximately three C_{60} molecules) of the chain ends. Shorter chains and chain ends were not sampled to preserve the stability of the tunneling junctions for spectroscopy.

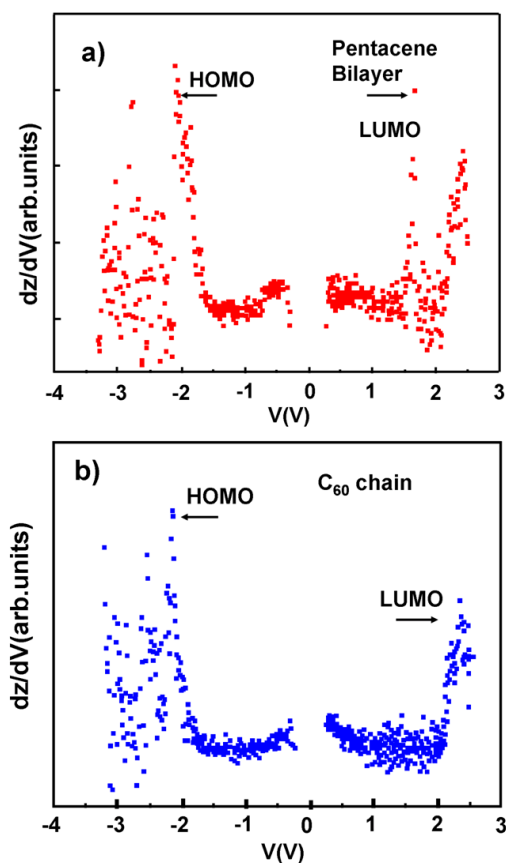


Figure 4.8 Tunneling spectra acquired in z - V mode: (a) On pentacene bilayer with HOMO and LUMO peak position indicated; HOMO traces averages 24 sweeps; LUMO traces average 30 sweeps; (b) C_{60} chains with HOMO and LUMO peak position indicated. HOMO traces averages 29 sweeps; LUMO traces average 33 sweeps. The initial condition is 23 pA 1.2 V for all four traces.

In a solid state molecular system, the transport gap is the difference between the ionization potential (IP) and electron affinity (EA) of the isolated molecule in the gas phase reduced by a polarization energy E_{pol} , which arises from the response of charge densities in neighboring molecules to electron addition or removal [142, 172]. This polarization response stabilizes injected electrons or holes, resulting in a reduced gap between $N+1$ electron and $N-1$ electron states in the solid compared to its gas phase value (N electron states) [172]. The amount of stabilization depends on details of the local environment such as the polarizability

and the number of near-neighbor molecules.

With this in mind, we can rationalize the spectroscopic measurements presented in Figure 4.9 on the basis of the local environments of the pentacene bilayer and the linear C_{60} structures. As a start, we consider the pentacene bilayer for which the measured gap (Figure 4.8.a) is essentially the same as the 3.6 eV transport gap measured for a thick pentacene films on Au surfaces [173]. This implies that the pentacene bilayer is thick enough to provide significant electrical decoupling of the templated C_{60} chain structures from the Ag(111) surfaces.

In contrast to the observation of a bulk-like transport gap for the pentacene bilayer, the magnitude of the gap measured for the C_{60} chain structure more closely resembles the gas phase value (IP-EA=4.9 eV) [174] than the value for thick C_{60} films ($\Delta E_{transport}=3.7$ eV) [174]. The C_{60} HOMO is shifted away from the Fermi level by ~ 0.2 eV and the C_{60} LUMO is shifted away from the Fermi level by ~ 0.6 eV when compared to the bulk fullerene crystal [174]. We attribute these differences to the reduced coordination of the molecules in the linear fullerene structures, which reduce the total polarization response of the surroundings of the chain when electrons are added or removed.

This interpretation can be semi-quantitatively justified by neglecting the polarization response of the pentacene bilayer on which the C_{60} chains are grown and by treating them as isolated objects. One can then track an approximately linear increase in polarization energy versus the number of C_{60} nearest neighbors (NNs). The polarization energy increase from 0 eV (0 NN, $E_{transport}=4.9$ eV) [174]

in the gas phase to 0.4 eV to the linear chain structure described here (2 NN, $E_{transport}=4.5$ eV) to ~ 1.2 eV for the surface of bulk C_{60} (9 NN, $E_{transport}=3.7$ eV) [174]. From a linear fit to polarization energy versus number of NNs [60] (assuming an ~ 0.1 eV uncertainty in the polarization energies extracted from Ref. [174]), as shown in Figure 4.9, it is estimated that each near-neighbor C_{60} molecule in a solid state system adds 0.13 ± 0.02 eV/NN polarization stabilization to the transport gap.

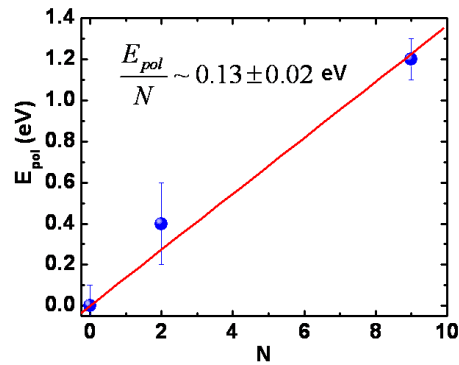


Figure 4.9 Linear fit to polarization energy E_{pol} versus the number of nearest neighbors

Simple electrostatic considerations allow an estimate of the expected total polarization energy in C_{60} solids using the formula $E_{pol} = \frac{ze^2\alpha}{R^2}$, where z is the number of NN molecules, α is the molecular polarizability (~ 0.085 nm³ [60]), and R is the NN spacing of ~ 1.0 nm. The value of 0.12 eV/NN [60] obtained from this formula is in good agreement with the estimate from the linear fit discussed above. The pentacene molecules underneath the chains will add polarization stabilization to the C_{60} contribution. We obtain acceptable agreement with the rough electrostatic calculation, despite neglecting this contribution, because the

magnitude of the total polarization energy associated with the pentacene film will most likely be less than or comparable to the experimental uncertainty in our determination of the transport gap.

These considerations also assume an equal polarization contribution from both the HOMO and the LUMO. This is not the case in our experiments where the LUMO is more significantly altered (relative to bulk C_{60}) by the reduced coordination than the HOMO. A more complete treatment would need to determine the polarization energy for electrons and holes separately in addition to considering the polarization response of the pentacene bilayer on which C_{60} chains are supported. However, given the agreement between the electrostatic arguments above the experimental polarization energies, it is clear that the major contributor to the magnitude of the measured transport gap is the low coordination of the C_{60} molecules in the chains.

4.2.4. Summary

In summary, we have described the formation of linear C_{60} structures resulting from the adsorption of C_{60} on an anisotropic pentacene bilayer template. At low coverages, C_{60} molecules occupy bridge-sites between parallel rows of pentacene molecules, forming chains with bulk-like C_{60} - C_{60} spacings. The transport gap measured for the linear C_{60} chains is 4.5 ± 0.3 eV. This value is much higher than the corresponding gap for bulk C_{60} due to the reduced coordination in the linear

configuration that lowers the overall polarization energy. These measurements provide direct evidence for the crucial role of local environment in determining functional properties in nanometer-scale systems.

4.3. C₆₀-Pentacene Network

4.3.1. Introduction

Intense research efforts are focused on molecular network structures assembled on solid surfaces. This is driven by the potential use as templates for organic devices and for molecular recognition in gas and bioanalytical sensors [159, 175-177]. Fabrication of these two-dimensional (2D) network structures can involve strategies analogous to those that have been used to tune pore properties and surface areas in bulk framework compounds and produce capacities for gas storage [178, 179]. For example, the deposition of iron atoms and terephthalic acid on Cu(100) generates a robust two dimensional network [180] that is analogous to the microporous iron-terephthalate framework compound [181]. In principle, surfaces allow even greater control of assembly kinetics, with the potential for supporting network formation with weaker interactions than are typically employed in bulk framework chemistry. Hydrogen and halogen bonds of modest strength have been extensively employed for network formation at surfaces [182-184].

A more physical approach to surface network formation involves templated assembly. In this surface-specific method, surfaces are first patterned on the nanoscale by either by physical (e.g. etching) or chemical (molecular adsorption) methods. This nanotemplate then directs subsequent molecular adsorption. This approach has proven suitable for the assembly of networks largely stabilized by van de Waals interactions. For example, coronene [185] and sexithiophene films [186], bimolecular networks [187], and pentacene bilayers [188] have served as templates for nanoscale patterning of C_{60} . Structural order is preserved throughout this templated assembly approach.

In this section, I show structure formation does not require ordered pentacene, but is directly produced from C_{60} deposition onto the pentacene 2D gas phase at room temperature. Coverage dependent studies give detailed insight into the mechanism of fullerene network formation. I describe how anisotropic C_{60} -pentacene interactions drive the spontaneous formation of nanonetwork structures. The kinetic route involves interaction of 2D gases of pentacene and C_{60} on the Ag(111) surface, resulting in a well-ordered bimolecular network. An overabundance of pentacene is additionally required, then expelled during co-crystallization, reaching the self-limiting $(C_{60})_4:Pn$ network stoichiometry. The co-crystalline structures rely upon weak anisotropic C_{60} -pentacene interactions, yet are surprisingly robust.

4.3.2. Experimental

Pentacene deposition was performed in the preparation chamber (base pressure of 1×10^{-9} Torr) from an effusion cell fit with a BN crucible held at ~ 390 K and positioned 5 cm from the Ag substrate. This sample was then transferred under vacuum to the UHV analysis chamber, where C_{60} deposition was performed from a separate source at 660 K. Deposition rates for pentacene and C_{60} were 0.6 ML/min and 0.3 ML/min, respectively, as monitored by a quartz crystal microbalance and calibrated directly from molecularly resolved STM images.

4.3.3. Result

4.3.3.1. C_{60} Network Formation on Pentacene/Ag(111) Molecular Films

Deposition of C_{60} on the 2D pentacene gas ($\theta_{\text{pentacene}} = 0.8$ ML) generates a network structure, as shown by the STM images of Figure 4.10.a and b. In this network, C_{60} molecules (bright features) arrange in extended chains that are spaced from each other by additional individual C_{60} molecules. This structure is commensurate, as evidenced by three 120° rotational domains, reflecting the 3-fold symmetry of the Ag(111) substrate. The C_{60} chains run along the substrate $[\bar{1}10]$ direction and the C_{60} nearest-neighbor distance of 1.01 ± 0.1 nm is similar to that of bulk C_{60} [60]. Other nanoscale dimensions of the network are the 1.92 ± 0.06 nm row-to-row spacing and the 2.55 ± 0.06 nm gap between “spacer” C_{60} molecules, as indicated in Figure 4.10.c.

The pores in the network structure, delimited by the C_{60} hard spheres, are $1.4 \text{ nm} \times 1.0 \text{ nm}$ in size, comparable to the expected footprint of a flat-lying pentacene molecule. Because the network is formed by C_{60} deposition onto a 2D pentacene gas, we conclude that pentacene molecules occupy network pores. This leads to the formation of the ordered network of C_{60} molecules, rather than the closed packed hexagonal structure that forms on bare Ag(111).

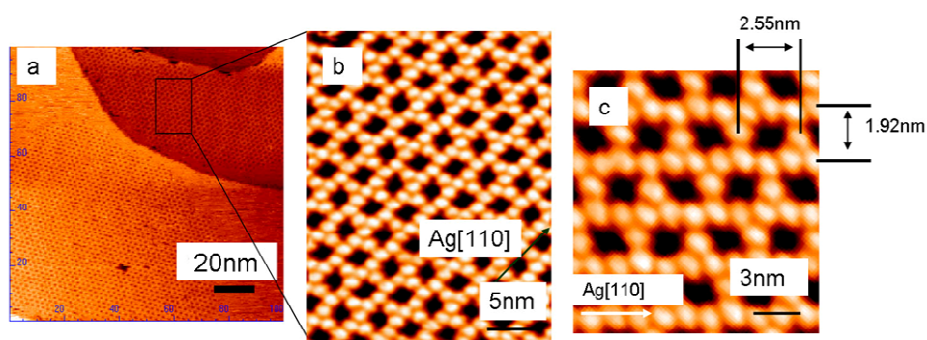


Figure 4.10 STM images of surface structures prepared by deposition of 0.4 ML C_{60} onto a 0.8 ML pentacene (2D gas) film at 300 K: (a) Extended domains of the network structure coexist with smaller regions of 2D pentacene gas (b) Structural uniformity and (c) Characteristic length scales of the network and pore features.

Occupation of the pores by pentacene molecules is confirmed by the result of depositing additional C_{60} molecules onto the network structure. As shown in Figure 4.11, post-deposited C_{60} molecules appear very bright and occupy pore sites. These pore-occupying C_{60} are raised well above the network C_{60} molecular plane by the pentacene molecules sandwiched in the network pores.

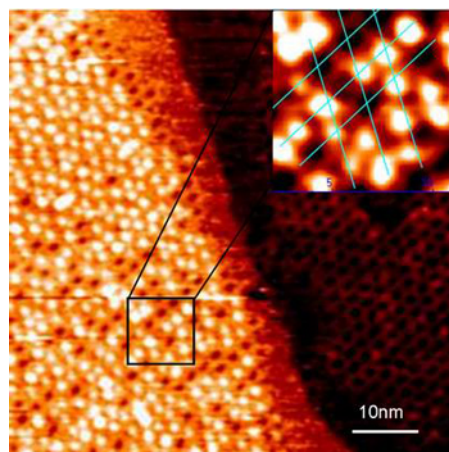


Figure 4.11 STM image of C₆₀ post-adsorbed on the pentacene-C₆₀ network. Magnified inset with network grid overlay confirms C₆₀ decoration of network pore sites.

We have investigated the bonding of C₆₀ molecules in the network structure to the Ag(111) substrate using local image state spectroscopy. Image states arise from the polarization induced by a charge above a metallic surface plane [189]. The Coulomb interaction between the polarization and the charge takes the form:

$$V(z) = -\frac{e^2}{16\pi\epsilon_0 z} \dots\dots\dots\text{Eq.(4.1)}$$

where z is the distance between the charge and the metallic surface. This potential yields a series of hydrogenic ground states converging on the vacuum level just outside of the surface. As a result, the energetic position of image states above molecular films is sensitive to the composition and structure of the molecular adlayers due to the interplay between dielectric screening (ϵ_0) and the electron affinity of the adsorbed film [190-192]. Tunneling spectroscopy measurements of image states on the C₆₀ network structure and those for a reference closed-packed C₆₀ monolayer on Ag(111) are compared in Figure 4.12. Strong features at 4.4 eV in the dz/dV spectra arise from image potential-derived states. Structure at lower

energy is due to higher unoccupied molecular orbitals on C_{60} (~ 2.9 eV) and “superatom” molecular orbitals at about 3.5 eV [193, 194]. Image state position in these two C_{60} -containing films are indistinguishable, indicating that C_{60} is bonded directly to the silver surface in the co-crystallized network, as it is for the close-packed C_{60} monolayer.

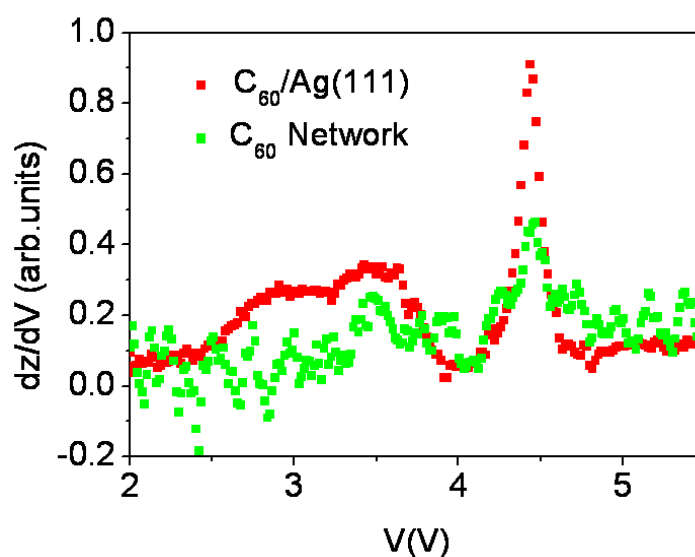


Figure 4.12 Comparison of dz/dV local tunneling spectra for C_{60} network structure (green) and reference C_{60} close-packed island (red) on Ag(111). Energy alignment of 4.4 eV image state feature confirms direct C_{60} -Ag(111) contact in network structure. Spectra acquired with initial tunneling condition of -0.87 V and 30 pA.

In contrast, C_{60} subsequently deposited on this nanonetwork (Figure 4.11) is elevated above the silver surface, which should lead to image-state shifts on the order of 0.2 eV [195]. Unfortunately, this multilayer tunnel junction is not sufficiently stable for scanning tunneling spectroscopy measurements at room temperature. We were also not able to image pentacene molecules in the network pores due to the finite size of the STM tip. When positioned directly above pentacene molecules, the tip “side tunnels” through C_{60} molecules that protrude

well above the pentacene molecular plane, as depicted in Figure 4.13.b and c. Consequently, the set-point current is attained without directly sensing the pentacene.

Based on these results we propose the model displayed in Figure 4.13 for the network structure. The main evidence from STM and STS experiments that this model explains are: (1) $z(V)$ characteristics show that C_{60} molecules sit directly on silver substrate, (2) The footprint of flat-lying pentacene molecules (van de Waals dimension of $16.6 \overset{\circ}{\text{A}} \times 7.4 \overset{\circ}{\text{A}}$) is well matched to the pore dimension, especially if C_{60} curvature is taken into account, and finally, (3) Situating pentacene molecules in the pores requires the long pentacene axes to orient along the Ag $[\bar{1}10]$ direction, the preferred pentacene alignment in monolayer pentacene structures [168]. This structural model also applies to the C_{60} -nanomesh structure [92], which was prepared by thermal annealing, but must also follow the kinetic mechanism, described below.

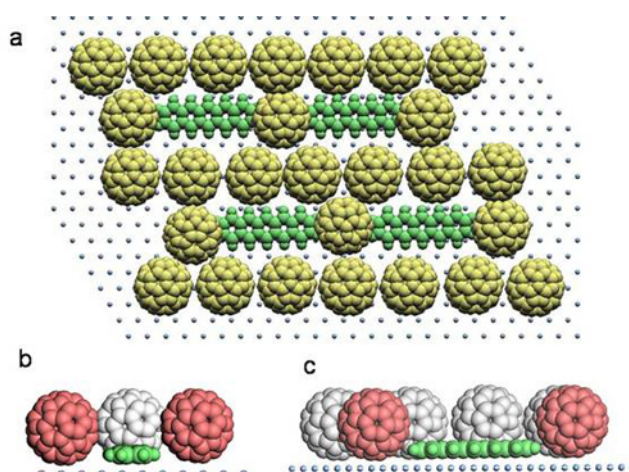


Figure 4.13 Proposed structural models for network structure showing alternating rows of C_{60} and C_{60} connected by pentacene (a) Top view, (b), (c) Side view

4.3.3.2. Pentacene precoverage dependence of co-crystallization

According to our structural model, the C₆₀-pentacene network structure has a well-defined stoichiometry of 4 C₆₀: 1 pentacene. We thus explored network formation as a function of the pentacene 2D gas by varying the pentacene pre-coverage at room temperature in the 0-1 ML range. The development of the network structure was found to depend on the pentacene 2D gas density and examination of this dependence provides formation mechanism about network formation.

When the initial pentacene coverage is below 0.4 ML, subsequently-deposited C₆₀ molecules spontaneously aggregate into close-packed islands that phase separate from the pentacene gas, as shown in Figure 4.14. The 2D pentacene gas is thereby compressed into the reduced surface area. No network formation occurs for $\theta_{\text{pentacene}} < 0.4 \text{ ML}$. Although mobile pentacene molecules in this 2D gas phase cannot be imaged directly, the diffusing pentacene molecules affect the contours of the C₆₀ island boundary. C₆₀ island shapes on bare Ag(111) without co-adsorbed pentacene phase exhibit a characteristic hexagonal shape with molecularly-straight island edges. In the presence of the pentacene 2D gas, attractive C₆₀-pentacene interactions lower the C₆₀ domain boundary energy, resulting in a more diffuse and mobile C₆₀-pentacene interface.

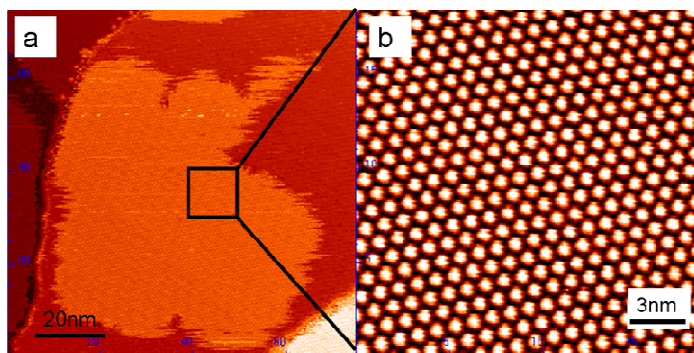


Figure 4.14 STM image of (a) A C_{60} island surrounded by the pentacene 2D gas phase. (b) Magnified STM image of the C_{60} island showing C_{60} forming close pack structure. The C_{60} island is very rough by comparison to the compact hexagonal C_{60} islands that form on clean Ag(111). This increased island boundary length reflects a decrease in the boundary energy due to attractive C_{60} -pentacene gas interactions. This phase separated structure was prepared by the deposition of C_{60} (0.6 ML) on the 2D pentacene gas (0.4 ML).

The onset of network formation is observed at a pentacene coverage of 0.4 ML. At this pentacene-coverage threshold, however, the network structure appears on only a small fraction of the surface. This is significant because, based upon pentacene: C_{60} stoichiometry alone, 0.3 ML of pentacene would be sufficient to generate a complete network structure. As pentacene coverage (density) increases from 0.4 ML to 0.8 ML the spatial extent of the network structure increases, covering up to 90% of the surface with a network structure (Figure 4.10.a).

A pentacene “local” gas density of 1.0 ML was next generated by depositing 1.2 ML pentacene on Ag(111). At this 1.2 ML coverage, islands of crystalline pentacene bilayer nucleate on the surface [168]. This generates a surface in which 20% of the area is covered by crystalline pentacene bilayers and 80% of the surface area is covered with a dense 2D pentacene monolayer gas, as shown in Figure 4.15.a. Deposition of C_{60} onto this two phases 1.2 ML pentacene

film generates the striking surface patterns of Figure 4.15.b. Of particular interest is the region originally occupied by the pentacene 2D gas, where deposition of C_{60} produces two distinct structures: the above nanonetwork (structure 1) and a new network structure (structure 2), in which dense rows of “star cells” are separated by conforming C_{60} chains. A third structure (structure 3) forms in the bilayer regions and consists of C_{60} chains templated by the crystalline pentacene bilayer [188], as previously discussed.

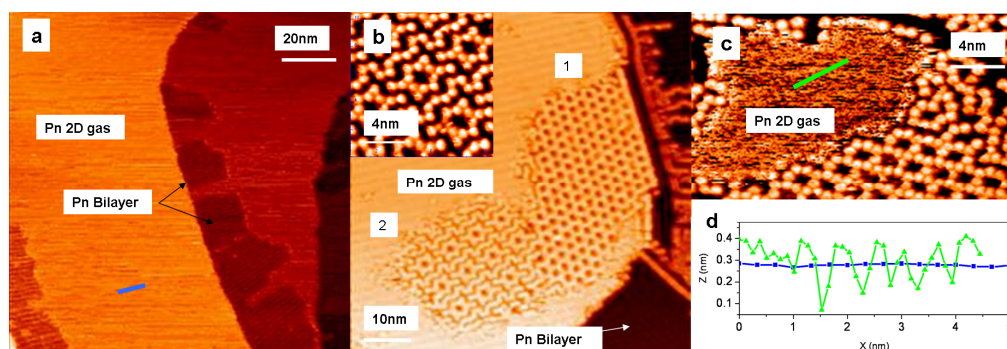


Figure 4.15 STM images of structural patterns generated directly by C_{60} deposition on dense 2D pentacene gas at room temperature: (a) 1.2 ML pentacene film structure prior to C_{60} deposition; (b) Multi-phase structure following 0.4 ML C_{60} deposition. Two networks (labeled 1, 2) form in 2D pentacene gas region, while C_{60} chains assemble on the pentacene bilayer. Inset: Network structure 2 magnified. (c) Multi-phase structure following 0.6 ML C_{60} deposition. Small pentacene 2D gas island is bounded by network structure 1 and pentacene bilayer-supported C_{60} chains; (d) Line profiles of pentacene 2D gas: blue- before C_{60} deposition (low pentacene density), green- after C_{60} deposition (high pentacene density)

A high resolution image of the new star-cell network (structure 2) is provided in the Figure 4.15.b inset. The pores in the star cells are comparable to the pores in the network structure, indicating similar occupation by flat-lying pentacene along the Ag $[110]$ direction. The lack of C_{60} connectivity in the star-cell structure

indicates a higher local pentacene density. In the absence of pentacene molecules, C₆₀ would readily form close-packed C₆₀ aggregates. The loose C₆₀ arrangement of structure 2 indicates that pentacene molecules are trapped between the C₆₀ star cells and the conforming chains, preventing C₆₀ aggregation. The gaps (dark region) between the conforming chains and star cells, 0.68 ± 0.09 nm, are more narrow than the network pores, indicating the tilting of pentacene molecules that occupy these regions.

The relative pentacene density in these two structures provides additional insight on their formation mechanism. The star-cell pattern is only observed for very dense 2D pentacene gases. We note that on the pentacene 2D gas film, network islands nucleate first along the pentacene monolayer-bilayer boundary. Network island formation at this ~1 ML pentacene coverage expels excess pentacene molecules into the surrounding pentacene 2D gas, increasing the local pentacene gas density. This higher density pentacene is needed to generate the star-cell pattern. While growth conditions can be adjusted to produce almost a complete network monolayer (structure 1), structure 2 is observed only in coexistence with either structure 1 or the bilayer islands, as Figure 4.15.b, where the requisite pentacene 2-D gas densities can be realized.

4.3.4. Discussion

In our experiment, a network structure reproducibly forms from the “chemically simple” case of C₆₀-pentacene. To understand this remarkable structure and its formation mechanism, we first summarize its characteristics and conditions for formation. The network:

1. Requires a pentacene pre-coverage of at least 0.4 ML;
2. Forms as the sole C₆₀-pentacene co-crystalline phase for C₆₀ deposition on surfaces covered with 0.4 - 1 ML pentacene. For $\theta_{\text{pentacene}} > 1$ ML, a star-cell structure and bilayer templated C₆₀ chains also appear;
3. Exhibits a self-limiting stoichiometry of 4 C₆₀: 1 pentacene;
4. Aligns pentacene-filled pores along the $[\bar{1}10]$ direction of the Ag(111) substrate;
5. Expels excess pentacene to the surrounding pentacene 2D gas phase, increasing the local 2D gas density.

The self-limiting stoichiometry is quite remarkable and implies that excess pentacene molecules are easily displaced by the incoming C₆₀ molecules. Such a molecular displacement is generally observed if the adsorption energy of the displacing molecule exceeds that of the displaced molecule [196]. Indeed, temperature programmed desorption (TPD) studies reveal that the desorption temperature for C₆₀ on Ag(111) is about 770K, corresponding to an adsorption energy of 2 eV/molecule [65, 66]. For pentacene, a considerably lower desorption maximum of 524K indicates a much smaller adsorption energy of 1.3

eV/molecule [91]. This difference in adsorption energy is consistent with the observed pentacene displacement.

The formation of the network structure is illustrated schematically in Figure 4.16. When C_{60} first arrives on the surface, isolated C_{60} molecules adsorb directly on the substrate displacing pentacene as needed and thereby increasing the local pentacene density (Figure 4.16.a). As C_{60} coverage increases, the substantial C_{60} - C_{60} van de Waals attraction [197] (~ 1 eV) drives the clustering of C_{60} on the surface (Figure 4.16.b). However, further C_{60} coalescence is inhibited by the pentacene 2-D gas environment. Attractive C_{60} -pentacene interactions arrest C_{60} islanding, driving the assembly of lower density C_{60} arrays (Figure 4.16.c). A critical pentacene density of 0.4 ML is needed to nucleate the network structure.

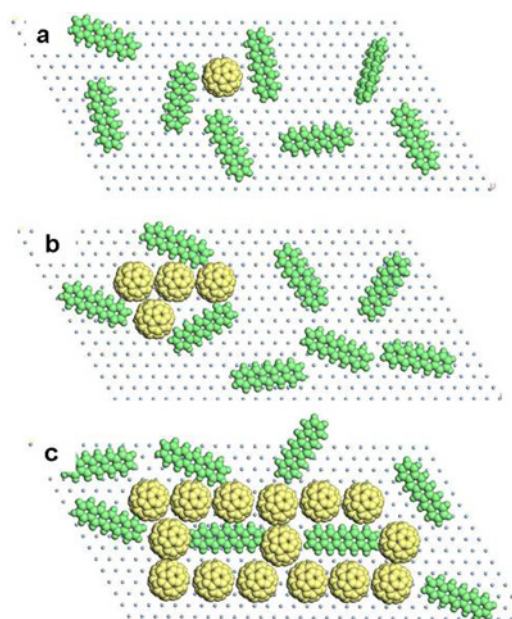


Figure 4.16 Schematic illustration of network formation mechanism upon C_{60} deposition on 2D pentacene gas

The network structure is a very stable arrangement at room temperature. Although we have not directly observed the critical nuclei for network formation,

network stability is easily rationalized. Pentacene molecules are aligned along the same $[1\bar{1}0]$ direction as in neat pentacene monolayer films [90, 168], indicating an energetically preferred flat-lying pentacene geometry. In their respective orientations on the surface, the electrostatic interactions between the C_{60} (octapole) and pentacene (quadrupole) are attractive, as depicted in Figure 4.17. The network structure thus takes advantage of electrostatic stabilization. We note that the electron-rich hexagons of the C_{60} may be further enhanced by the formation of a Ag(111)- C_{60} interface dipole [155, 156, 198], as suggested in the theoretical computations.

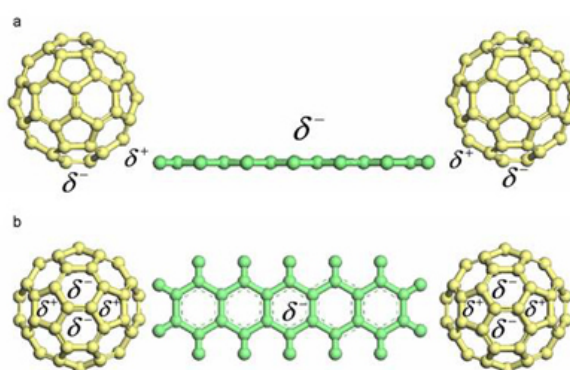


Figure 4.17 Schematic model of the local C_{60} -pentacene arrangement in network structure emphasizes favorable pentacene quadrupole - C_{60} octapole interactions: (a) side view, (b) top view

The displaced pentacene molecules can not be imaged directly at room temperature with STM. Based upon energy requirements, displaced pentacene will not completely desorb from the surface, but will transfer to the surrounding surface phases. Initial pentacene coverage of 0.8 ML, for example, ultimately produces a network structure that spans 80% of the surface area, but contains only 0.25 ML of the pentacene. The displaced 0.55 ML pentacene are transferred to

network-free surface regions. The higher pentacene density is manifested by the “star cell” patterns that emerge along the network-2D gas boundary and by the increased tunneling noise in the 2D gas regions. A comparison of line profiles for the 2D gas phase before and after C_{60} deposition (Figure 4.16.d) shows a pronounced increase in tunneling noise due to the increase in pentacene density.

4.3.5. Summary

We have described the spontaneous formation of C_{60} -pentacene network structures resulting from the co-crystallization of C_{60} molecules and pentacene molecules in a mobile 2D gas phase. This structure is realized from a wide range of initial pentacene coverages and exhibits a self-limit stoichiometry of $(C_{60})_4$ pentacene. A molecular model for the network structure is proposed consisting of an open network of C_{60} chains with flat-lying pentacene molecules trapped in the network pores. The stability of the C_{60} -pentacene network phase is accounted for by the adsorption energies of each molecular component and attractive electrostatic interactions between C_{60} and pentacene in their preferred chemisorption geometries. Network formation requires a minimum pentacene coverage in order to buffer strong C_{60} - C_{60} interactions and prevent C_{60} island formation. The stoichiometry of the network structure is self limiting over a wide range of pentacene coverage (0.4 ML - 1.0 ML). At even higher pentacene densities, an additional co-crystalline pattern (star-cell arrangement) is observed.

It is remarkable that such long range and robust supramolecular arrangements can be realized by relatively weak electrostatic interactions between these large aromatic molecules. The known anisotropy of electrostatic interactions for rigid aromatic molecules, and molecular semiconductors in particular, provides a significant tool for assembling molecular network structures. Here we have described a mechanism by which surface dynamical processes combined with weak anisotropic interactions drive precise molecular assembly.

5. Chapter 5 Binary system: Zinc Phthalocyanine: C₆₀

As discussed in chapter 3, monolayers of zinc phthalocyanine (ZnPc) on Ag(111) exhibit two different temperature-dependent structures: a high density (HD) phase and a low density (LD) phase. They are now used to fabricate binary films with distinct chemical morphologies, in similar manner to pentacene:C₆₀. Three binary structures will be discussed in this chapter: (1) ZnPc-on-C₆₀ bilayer; (2) C₆₀-on-HD ZnPc bilayer; (3) C₆₀-ZnPc co-crystalline monolayer. Collectively, these experiments show how knowledge of monolayer structures and strict control of sample processing allow for tailoring of the chemical morphology of binary films. In section 5.2, the molecular dynamics simulation is done by Mr. Qiang Liu, from Professor John Weeks group.

5.1. ZnPc Highly Tilting on C₆₀ Monolayer

5.1.1. Introduction

The morphology of organic molecular-molecular (O/O) interfaces is known to correlate strongly with the electronic structure and therefore with carrier dynamics at the interfaces [199, 200]. Even small changes in film morphology can affect charge separation at the O/O interfaces, hole and electron mobility, and hence

overall device performance. Much effort has been spent to understand and control the molecular orientation of organic films on inorganic substrates [148, 201, 202]. In general, the molecular orientation of the molecules is determined by the relative strengths of the molecule-molecule versus molecule-substrate interactions [121]. For example, when the latter force dominates, planar molecules like metal phthalocyanine lie with their molecular plane parallel to the metallic surfaces [115, 135]. However, on polycrystalline and amorphous substrates, molecules often “stand” on their side with a stacking direction parallel to the substrate [121] since in this configuration the dominant intermolecular attraction is maximized. Molecular orientation at the interface of organic heterojunctions, however, is less extensively investigated. Several controlled structural studies have been carried out to study the evolution of film morphology, molecular orientation, and ordering during the growth of organic thin films on another organic thin film [203-205], however, almost all such reports refer only to thick films investigated by x-ray diffraction. There is a dearth information on fundamental aspects of interface formation in organic heterojunctions. It should be noted that the electric and optical properties of organic thin films depend on the molecular orientation in small domains at micrometer or nanometer scales [206]. Therefore, characterization of morphology and electronic structure at organic heterojunctions with nanometer resolution is highly desirable. As discussed in chapter 4, in the pentacene-on-C₆₀ monolayer, we observed an extraordinarily long range modulation of interface morphology due to stress induced on the “standing”

pentacene films by the C_{60} sublayer [207]. In this section, we extend such measurements to systems of immediate relevance to organic photovoltaics: zinc phthalocyanine (ZnPc) and C_{60} . The effects of inorganic substrate temperature on the molecular orientation during the film growth of phthalocyanine molecules are well documented [208-212]. For example, copper phthalocyanine (CuPc) adsorbed on a HOPG, lies flat at room temperature and becomes tilted and condensed at temperature below 130 K [213]. The impact of substrate temperature effects on heterostructure interfaces is now explored.

For the ZnPc- C_{60} heterojunction, additional studies of F_{16} ZnPc- C_{60} heterojunctions demonstrate the influence of chemical modification on interfacial architecture.

5.1.2. Experiment

Binary organic-organic interfaces were prepared with the following sequential deposition protocols: a uniform single layer of C_{60} was first grown on the Ag(111) by depositing a multilayer film of C_{60} from an effusion cell (Createc LTC-40) and then annealing to ~ 500 K. The result was a uniform $(2\sqrt{3} \times 2\sqrt{3})R30^\circ$ overlayer of C_{60} [66]. ZnPc or F_{16} ZnPc were then deposited onto the room-temperature C_{60} monolayer from a separated effusion cell at 660 K or 680 K, respectively. The typical deposition rate is 0.25 ML/min.

5.1.3. Results

5.1.3.1. ZnPc on C₆₀ monolayer.

Room-temperature-grown phase:

Figure 5.1.a shows a large-scale STM image of a ZnPc monolayer island deposited on one monolayer C₆₀/Ag(111). At 0.3 ML ZnPc coverage, the islands are up to 500 nm long with aspect ratios (length to width) of 5 to 10. Two orthogonal branches are commonly observed. The two branch directions are along the $[\bar{1}10]$ and $[\bar{1}1\bar{2}]$ of C₆₀ monolayer, henceforth, referred to as the α -phase and the β -phase, as marked in Figure 5.1.b. ZnPc-elongated islands extend across the steps of the underlying C₆₀/Ag(111) substrate without interruption. The ZnPc-free regions show $2\sqrt{3} \times 2\sqrt{3}R30^\circ$ -C₆₀/Ag(111), which provides directional references. The apparent height of the ZnPc islands above the surrounding C₆₀ was measured as 1.1 ± 0.2 nm (Figure 5.1.b inset) for both phases based on an average of 15 different line profiles across different island edges on different days. In general, the height data in STM measurement is not simply reflected in the topography because the measured height is influenced by both the state density (surface and tip) and the apparent tunneling barrier height. A crude comparison of the 1.1 nm film height with the physical dimension of ZnPc (1.4 nm \times 1.4 nm), does suggest a 55° tilted ZnPc layer, as expected for this weak ZnPc-C₆₀ interaction. Based upon angular-resolved near edge x-ray absorption fine structure (NEXAFS) measurements [214] reported for CuPc/C₆₀ bilayer by Huang *et.al.*, CuPc adopts a

highly tilted configuration with an average angle of $\sim 70^\circ$ relative to the surface plane, which is consistent with our present observations. The detailed α and β phases structures are described below:

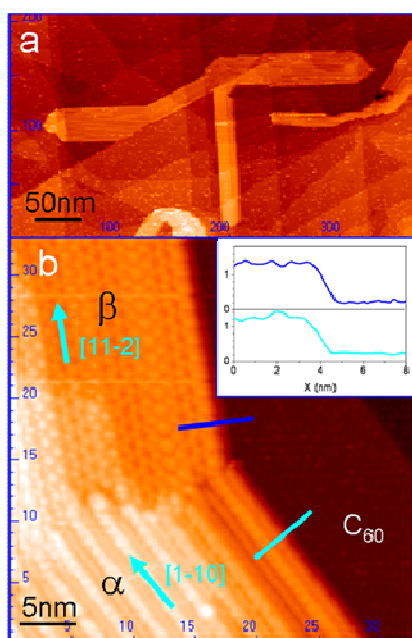


Figure 5.1 (a) Large scale of STM image showing a ZnPc island on top of 1 ML $C_{60}/Ag(111)$; (b) STM image showing domain boundary of the ZnPc islands: α -phase along $[1\bar{1}0]$ of C_{60} monolayer, β -phase along $[11\bar{2}]$; Inset: Line profile across the point on the island edge for two phases indicated by the dark blue (β -phase) and bright blue (α -phase).

Figure 5.2.a shows the α -phase domain contains three distinct striations running along the substrate $[1\bar{1}0]$ direction. The stripes are marked as A (bright), B (dim) and C (dark), as shown in Figure 5.2.a. The bright stripes (A) are always nested between two dim stripes (B). The apparent height of the A-striation is ~ 0.08 - 0.10 nm higher than that of B-striations, based upon 32 measurements. The magnified STM image in Figure 5.2.b shows the molecular packing within each striation. Both A and B striations display topographic variations with a periodicity of 0.93 nm, and 0.46 nm, respectively. In contrast, the C striation appears smooth

and featureless and is thus attributed to missing row. As we can see from Figure 5.2.a, these missing rows (C-striations) are not uniformly distributed and thus do not reflect a Moiré Pattern along $[11\bar{2}]$ direction.

The number of near-neighbor A-striations describes the width of defect-free domains that are between two C-striations, as marked in Figure 5.2.a. The statistical distribution of defect-free islands, based upon 16 different island samples, is shown in Figure 5.2.c. The nearest-neighbor distance between A-striations is about 2.45 nm. Considering the molecular dimension of ZnPc (1.4 nm \times 1.4 nm), this distance significantly exceeds a single molecule width, but is less than that of two adjacent flat-lying molecules. To accommodate two ZnPc molecules into this 2.45 nm width, ZnPc molecules are presumed to arrange in a zigzag style along the $[11\bar{2}]$ substrate direction, similar to ZnPc in the bulk crystal [215]. The height difference between the A-striation and B-striation reflects actual topographic differences. A structural model that mimics the α -ZnPc polymorph is shown in the Figure 5.2.d. The unit vectors of the α -phase of ZnPc islands are $a = 2.45 \pm 0.04$ nm, $b = 0.93 \pm 0.05$ nm, $\theta = 92 \pm 3^\circ$, as highlighted in the model. The internal periodicity in both A-striation and B-striation is explained by the model. Two protrusions in B-striations represent the two phenyl rings of neighboring ZnPc molecules (brown circle); the large protrusion in A-striations corresponds to the unresolved juxtaposition of edge-contacting ZnPc molecules (orange circle).

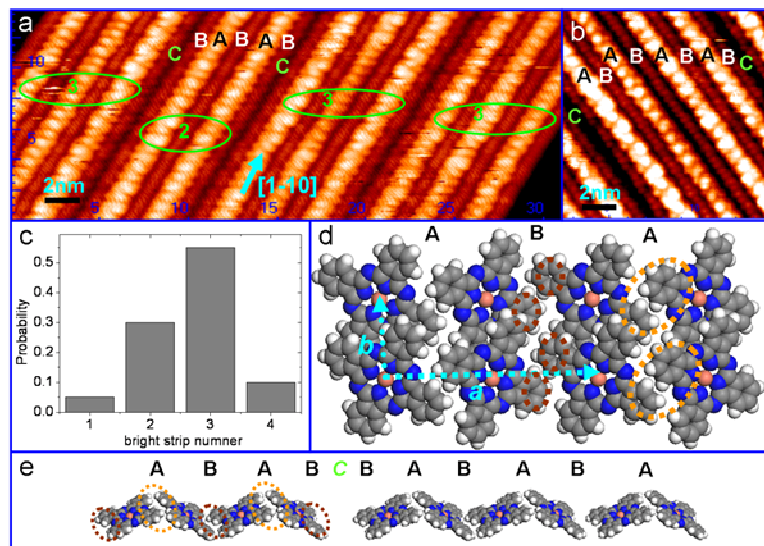


Figure 5.2 (a-b) STM images showing (a) the α -phase ZnPc on C₆₀ monolayer, containing three ZnPc stripes of varying intensity: A (bright), B (medium) and C(dim.) with variable spacing (b) molecular scale features; (c) Histogram of the number of near-neighbor A-striations between any two C-striations; Proposed model: (d) Top view; (e) Side view.

Like the α -phase, the β -phase contains molecular rows (now along $[1\bar{1}2]$), under magnificent STM (Figure 5.3.a), the striations are comprised of zigzag features with a strict 1.69 nm periodicity. Contrast variation, are small (0.01 nm~0.03 nm), but display much richer shape variation than the α -phase. Typically, such detailed variations reflect tunnel variations due to registration with the C₆₀ sublattice. Bright spots represent good “contact” and are presumed to be lattice matched to the C₆₀ sublayer. Such contrast is reminiscent of other standing organic monolayer phases [150]. For neighboring stripes as shown in Figure 5.3.b, we propose the model of Figure 5.3.c. The ZnPc unit cell is described by the cell parameters: $a = 1.48 \pm 0.02$ nm, $b = 1.69 \pm 0.03$ nm and $\theta = 120 \pm 3^\circ$.

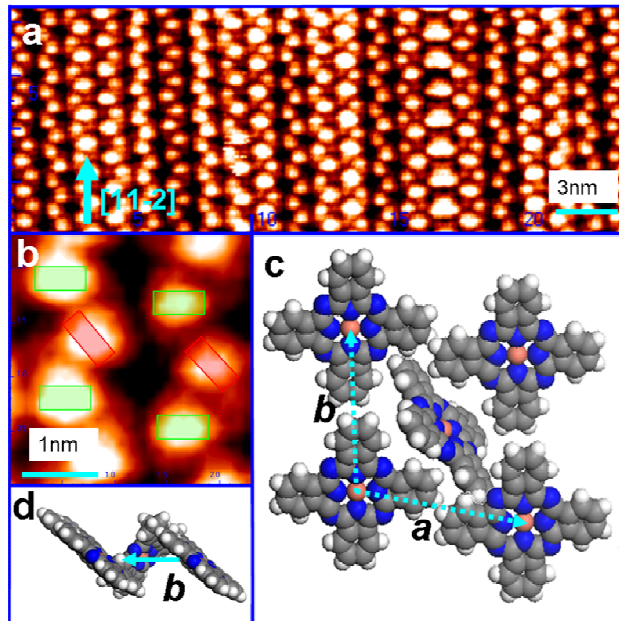


Figure 5.3 (a) STM image of the ZnPc β -phase on C_{60} showing (b) Magnified image showing two inequivalent orientations marked as green and red; Proposed model of the ZnPc β -phase islands:(c) Top view; (d) Side view.

Thermally Annealed Phases

To test the thermal stability of these room-temperature-grown phases, samples were annealed at 400 K for 10 min prior to room-temperature imaging. As shown in Figure 5.4.a, island shapes compact and the apparent island height increases to 1.5 ± 0.3 nm (Figure 5.4.b). The near equivalence of the island height and ZnPc molecules width reveals ZnPc in a near-vertical orientation. A previous x-ray diffraction (XRD) study [216] of thick ZnPc films on glass showed that the ZnPc adopts a higher tilt angle at higher substrate temperature ($T_s=373$ K to 473 K), consistent with our observations. The room-temperature-produced α - and β -phases are completely transformed into a singular structure. Within this more robust structure, molecules are organized into $[1\bar{1}0]$ substrate-directed rows. The ZnPc unit cell showing spacing between rows is of $b = 0.92 \pm 0.04$ nm and along

the rows periodicity of $a = 0.52 \pm 0.04$ nm, as marked in Figure 5.4.c. These dimensions correspond to the cofacial columnar stacking of ZnPc molecules within the bulk β -phase. Interestingly, the stress defects observed in the α and β -room temperature phases are not present in this vertical standing phase. As expected, the intermolecular π - π interactions between the stacked molecules within the upright phase exceed the spacing in the α - and β - phase molecular arrangements. The structure and morphology of the ZnPc films are thermally stable up to the desorption temperature of approximately 500 K.

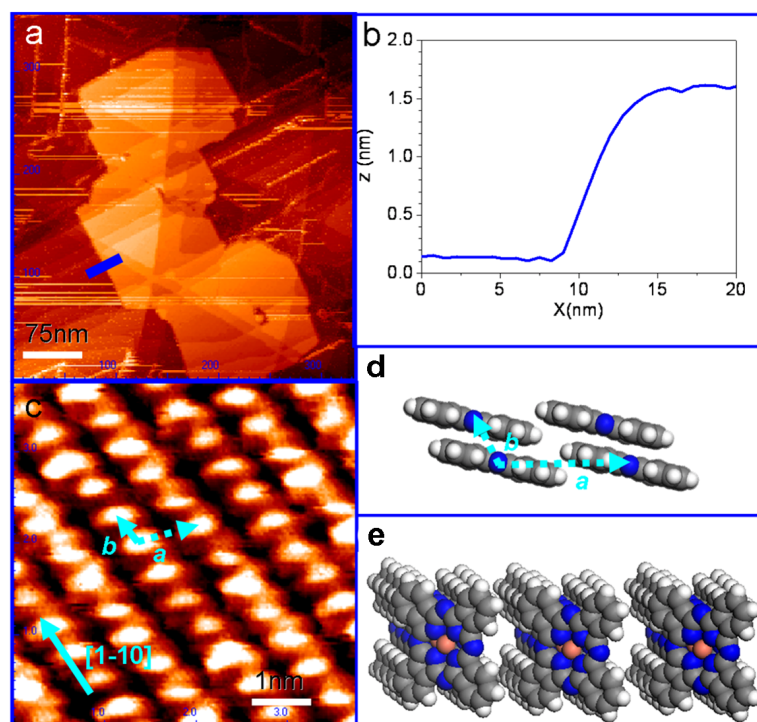


Figure 5.4 (a) STM image of post-deposition annealed ZnPc island on C_{60} showing a compacted shape relative to room-temperature-grown islands; (b) Line profile across the point on the island edge indicated by the blue line in (a); (c) STM image showing molecular scale features with unit cell superimposed; (d) Top view of proposed model; (e) Side view of proposed model.

5.1.3.2. $F_{16}ZnPc$ on C_{60}

To explore the impact of chemical modification on heterojunction formation, we additionally explore $F_{16}ZnPc:C_{60}$ interface formation. Figure 5.5.a shows an STM image of an $F_{16}ZnPc$ island grown on C_{60} monolayer/Ag(111) at room temperature. The elongated island shape is similar to $ZnPc$ islands on the C_{60} monolayer (image not shown). The apparent height of the $F_{16}ZnPc$ islands is as 1.2 ± 0.3 nm, based on an average of 15 different line profiles (Figure 5.5.b) across different island edges. This suggests a layer of highly tilted $F_{16}ZnPc$ molecules, similar to $F_{16}CuPc$ on Al_2O_3 [217, 218] and on SiO_2 [219]. In the present, the long edge of the island is along the substrate $[1\bar{1}2]$ direction. A high resolution STM image in Figure 5.5.b reveals $F_{16}ZnPc$ islands consist of short “stacks” of features along the $[1\bar{1}2]$ and $[1\bar{2}1]$ directions. The width of each stack is 0.98 ± 0.05 nm with a periodicity of 0.42 ± 0.03 nm. This dimension is also in agreement with $F_{16}ZnPc$ structures on Al_2O_3 [217, 218] and on SiO_2 [219], as measured by Atomic Force Microscopy (AFM). We assign each bright spot to an $F_{16}ZnPc$ molecule in upright orientation on C_{60} monolayer with the aromatic plane tilted slightly 15° from the surface normal, similar to the α -phase and β -phase $ZnPc$ islands on C_{60} . Imaged stacks can be recognized as columnar stacks of molecules, as shown in Figure 5.5.c. The stack direction (bright blue arrow in Figure 5.5.c top view) is about 5° from the $[1\bar{1}2]$ substrate direction (long magenta arrow in Figure 5.5.b and 5.5.c). There are two key differences between the $F_{16}ZnPc:C_{60}$ interface and those on the oxide surfaces, $F_{16}CuPc$ on Al_2O_3 and

on SiO₂. First, the length of the columnar stacks on C₆₀ is variable (4 to 7 molecules). The histogram of stacks length is shown in Figure 5.5.d, based on six different F₁₆ZnPc islands. Second, stacks are connected by a dim feature along the $[1\bar{1}2]$ direction (long magenta arrow in Figure 5.5.b and 5.5.c), as depicted by dark green circle in Figure 5.5.b. Based upon our structural model, the dim spot represented a F₁₆ZnPc molecular (point) defect, in which the F₁₆ZnPc adopts a more shallow tilt to bridge neighboring stacks. This is depicted in Figure 5.5.c. The defects are regularly spaced by 1.21 ± 0.05 nm, along the $[\bar{1}21]$ direction (short magenta arrow in Figure 5.5.b and 5.5.c). However, due to the apparent variations in stack length, there is no strict periodicity along the $[\bar{1}1\bar{2}]$ direction (long magenta arrow in Figure 5.5.b and 5.5.c). Upon annealing at 450 K for 10 min, no obvious structural transition is observed. The desorption of F₁₆ZnPc islands takes place above 480 K.

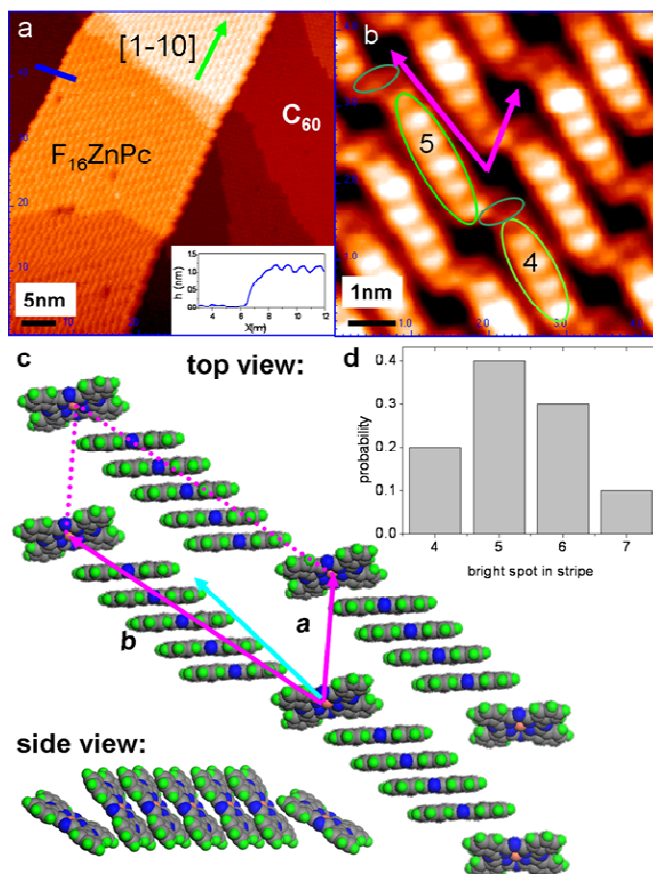


Figure 5.5 (a) STM image showing a $F_{16}ZnPc$ island on a 1 ML $C_{60}/Ag(111)$, The C_{60} close packed $[1\bar{1}0]$ direction is highlighted in green; Inset: Line profile across the point on the island edge indicated by blue line; (b) STM image showing molecular scale features; Defect is marked by dark green circle; Different number of molecular features in different stacks are highlighted by the light green circle; (c) Schematic model of the point defects at the end of each stack; vector along $[1\bar{1}2]$: top view (Actual tilt angle is shown in the side view), (d) Histogram of the number of $F_{16}ZnPc$ molecules contain in each stack.

5.1.4. Discussion:

5.1.4.1. Island Shapes

Large islands, observed even in the room-temperature grown film, generally signify large ZnPc and $F_{16}ZnPc$ mobility on the C_{60} surface. This implies weak

ZnPc- C_{60} and F_{16} ZnPc- C_{60} interactions. Large elongated islands of upright standing molecules are commonly observed on non-metallic surfaces, such as 6P ($C_{36}H_{26}$) on $TiO_2(110)$ [220], CuPc on $NH_3/Si(001)$ [221], and F_{16} CuPc on Al_2O_3 [217, 218] and on SiO_2 [219]. Anisotropic islands shapes can be of kinetic origin, reflecting: (1) preferential diffusion direction or (2) island-edge variation in sticking coefficient. Anisotropy in thermodynamically favored islands largely reflects the anisotropy in the intermolecular interaction, which is closely related to sticking anisotropies. For ZnPc, elongated islands persist after annealing, albeit more compact, suggesting diffusion anisotropy is not the main shape determinant. Based upon our structural model, molecular arrays at the ends of narrow islands experience a stronger π - π interaction than that at the sides of islands, resulting in a rapid-growth direction. Therefore, attachment anisotropy drives the formation of these highly anisotropic elongated islands. At higher substrate temperatures, the ZnPc islands on C_{60} become more compact with an aspect ratio (length-to-width) reducing to around 3-to-1. This is consistent with the structural model (Figure 5.4.e), in which the shift-stacked ZnPc-ZnPc interactions along the a and b directions are expected to be less anisotropic than for the α - and β - phases.

5.1.4.2. Stress induced defect.

STM images of Pc molecules on C_{60} substrate reveal dense regular packing of molecules along specific crystallographic directions, resulting in molecular

striations. However, on a length scale of a few nanometers, substrate structural variations between striations are observed. Lattice mismatch between overlayer and sublayer generally induces strain on the overlayer, often resulting in such anisotropic structures. The consequence of an adsorbate favoring a lattice constant distinct from that of the substrate can be studied analytically in one dimension (1D) via the Frenkel-Kontorova model. This model is used to predict dislocations and domain walls in solids under crystallographic stress [222]. Below a critical value of the mismatch the adlayer remains commensurate with the substrate; above it domain walls are formed, separating commensurate regions, i.e., regions where the adsorbate layer has a perfect registry with the substrate. Inside the domain wall the adsorbate occupies different adsorption sites, leading to an effective “rumpling” of adsorbate layer. The domain walls then form a superlattice on a perfect substrate, effectively releasing the stress by either increasing or decreasing the number of atoms in the adsorbate layer, thus stabilizing the adlayer [223].

We now consider the height variations in the molecular striations as evidence of defects induced by interfacial stress. For MPc on the C₆₀ monolayer, even though the interaction of C₆₀ with MPc molecules is weak relative to a metal surface, the C₆₀ monolayer nonetheless is expected to be highly corrugated due to the C₆₀ 1 nm spacing and the C₆₀-orientation (pentagon vs. hexagon) that affects the C₆₀-Pc interaction. Since the lattice mismatch between C₆₀ sublayer and the MPc *ac* plane is large, the sublayer will exert forces that should distort the ZnPc overlayer from the bulk-like geometry. The formation of defects can act to relieve

this substrate induced stress and should appear along the low energy direction. This is consistent with our observations. Based upon the proposed structural models for the α - and β -phase of ZnPc islands, the striation direction emphasized the π -association of highly-tilted ZnPc. This direction is the energetically favored ZnPc film axis and does not respond to the underlying stress. In contrast, the ZnPc intermolecular interaction along the other direction is relatively weak and is very susceptible to Frenkel-Kontorova triggered stress relief. Upon 400 K annealing, all the ZnPc molecules take on a standard stacked face-to-face geometry. This configuration reinforces π - π interactions.

For F_{16} ZnPc islands on C_{60} , we expect electrostatic repulsion between the nearest neighbors with 16 fluorine atoms in the molecule. Typically, four to seven F_{16} ZnPc molecules assemble into a π -stack short stick feature along the direction 5° offset from the C_{60} $[11\bar{2}]$ direction, possibly due to the electrostatic repulsion. Meanwhile, the corrugation from C_{60} sublayer prevents short stick growing longer. A defect F_{16} ZnPc (dim spot) appears to release the tension induced by the mismatch between F_{16} ZnPc and C_{60} .

Combining this observation with our previous result of pentacene on C_{60} monolayer [207], we suggest that defects arising to relieve stress in organic thin films due to interactions with the underlying C_{60} monolayer are a common phenomenon.

5.1.5. Conclusion:

We have used STM to observe the interface morphology of ZnPc islands that assemble as highly tilted phases on 1 ML C₆₀/Ag(111). In room-temperature-grown films, defects arise to relieve stress in the ZnPc film due to interactions with the underlying C₆₀. Defects proliferate along the direction of weakest ZnPc-ZnPc interaction. Upon 400 K annealing, ZnPc molecules become erect and defects largely disappear due to stronger molecule-molecule interactions. F₁₆ZnPc on C₆₀/Ag(111) shows similar behavior. Defects appear along the [112] and [121] directions of C₆₀. The electrostatic repulsion between F₁₆ZnPc molecules and the interaction between ZnPc and C₆₀ account for defect formation. Together with pentacene/C₆₀ structures reported in Chapter 4, the observations show that stress-induced defects on organic-organic interface are common. Carefully engineering stress relief patterns at soft interfaces can be used to control nanoscale interface morphology.

5.2. Reversed Deposition: Formation of Wandering C₆₀ Chains

5.2.1. Introduction

Interaction between C₆₀ molecules generates monolayer structures with hexagonal packing and 1 nm nearest-neighbor spacing [60] on a rich variety of

inorganic substrates [66, 224-228]. Alternative arrangements, such as linear fullerene structures, usually require the use of a template such as a vicinal surface [164, 165]. In Chapter 4, such template-induced C_{60} nanochains formation was described for trace C_{60} coverage on a pentacene bilayer. In this structure, C_{60} chains are stabilized by electrostatic and dispersive forces. When C_{60} coverage exceeds ~ 0.05 molecules/nm², however, a disordered phase, consisting C_{60} wandering chains, arise. Such wandering-chain phases were also observed on monolayer of zinc phthalocyanine (ZnPc) and α -sexithiophene monolayer [169]. Such filamentous structures are in complete contrast to C_{60} 's typical close-packed growth habit, but are reminiscent of structures that arise in dipole fluids. Dipole fluids models describe spontaneous spatial modulations in a diverse collection of 2D systems, including Langmuir monolayers [229], thin magnetic films [230], and physisorbed monolayers on solid surfaces [231]. Patterns of stripes, bubbles, and intermediately shaped domains arise in these systems from the competition between short-range attractions and longer-range repulsions between system components. We now extend the dipole fluid model to wandering C_{60} chains. From a fundamental scientific viewpoint, the formation of single molecular width chains in the absence of a template is challenge. From a technologic viewpoint, low density wandering C_{60} chains are valuable as continuous pathways for charge transport. The understanding of the formation mechanism of such C_{60} chains is an important goal.

In this section, I present STM investigation and a statistical analysis of

wandering chains formation. Chain structures are compared to the molecular dynamics prediction of a 2D dipole fluid with the C_{60} - C_{60} attractive interaction described by the well established Girifalco potential and the C_{60} - C_{60} repulsion described by an effective dipole term. The physical origin of this dipole term is then discussed.

5.2.2. Experimental

The substrates used for C_{60} -filament formation, are first described. Ag(111) surface was prepared. Deposition of 1.5 ML ZnPc on Ag(111) from an effusion cell at 660 K (typical deposition rate of 0.25 ML/min), was followed by a mild annealing at 400 K. A high density (HD) ZnPc monolayer resulted, as shown in Figure 5.6.a. Pentacene bilayer films were also used as substrates for C_{60} wandering chains. Pentacene was evaporated in a preparation chamber from a boron nitride crucible in an effusion cell held at 390 K. The C_{60} -wandering chain phases were then prepared by C_{60} evaporation from an effusion cell at 650 K (typical deposition rate of 0.3 ML/min). Structural analysis was performed on room temperature as-grown films.

5.2.3. Results

5.2.3.1. STM measurements

The STM image of 0.3 ML C₆₀/HD-ZnPc in Figure 5.6.a shows the aggregation of C₆₀ into islands, with the remaining ZnPc regions intact. This indicates a large C₆₀ diffusion length on ZnPc. Bare ZnPc regions reveal no structural change from the HD-ZnPc monolayer, as shown in Figure 5.6.a.(inset). C₆₀ island nucleation occurs at the domain boundary of the supporting HD-ZnPc layer. The estimated C₆₀ diffusion length (≥ 100 nm) implies the corrugation from the underlying organic film is relatively shallow. With increasing C₆₀ exposure to 1 ML, islands of the wandering C₆₀ chains cover the surface (Figure 5.6.b). Within these islands, C₆₀ assemble into wandering chains with a pronounced linear character and some additional branching. The intermolecular distance between C₆₀ molecules is 1.0 nm, close to the van der Waals distance of bulk C₆₀ [60]. The C₆₀ density within these islands is ~ 0.54 molecules/nm², with standard deviation ~ 0.04 molecules/nm², depending weakly on coverage (0.2 ML~1 ML). This structure is of considerably reduced density by comparison to the C₆₀ close-packed hexagonal phase, with a density of 1.15 molecules/nm². The typical C₆₀ branch length crosslink separation is 5.12 nm, with standard deviation of 1.16 nm. After annealing the sample at 400 K, modest coarsening is observed in the formation of C₆₀ clusters. These clusters coexist with the C₆₀, as shown in Figure 5.6.d, and remain a minor film structure. To quantify the effect of annealing, we measured

the number of nearest neighbors per molecule (Figure 5.6.e). A nearest-neighbor is defined as that located within a center-to-center distance of $r_c=1.0$ nm. For unannealed samples (Figure 5.6.c), more than 50% of C_{60} are in linear ($N=2$) arrangement, indicating the one-dimensional character of the structures. The average coordination number of unannealed sample is 2.28. For annealed samples, the coordination number increases to 3.15, signaling the aggregation of small clusters. Higher temperature annealing was not undertaken due to the finite thermal stability of the molecular underlayer structures (pentacene bilayer and ZnPc monolayer). We note that wandering chain C_{60} phase also on pentacene monolayer/Au(111) (not shown), pentacene bilayer/Ag(111) (Figure 5.6.f), and sexithiophene/Ag(111) [169]. These chain-phase structures are different from the C_{60} structures on inorganic substrates, where C_{60} molecules form close-packed structures. The lower-density C_{60} structure on organic substrates mediated C_{60} - C_{60} interactions by the organic substrate molecules.

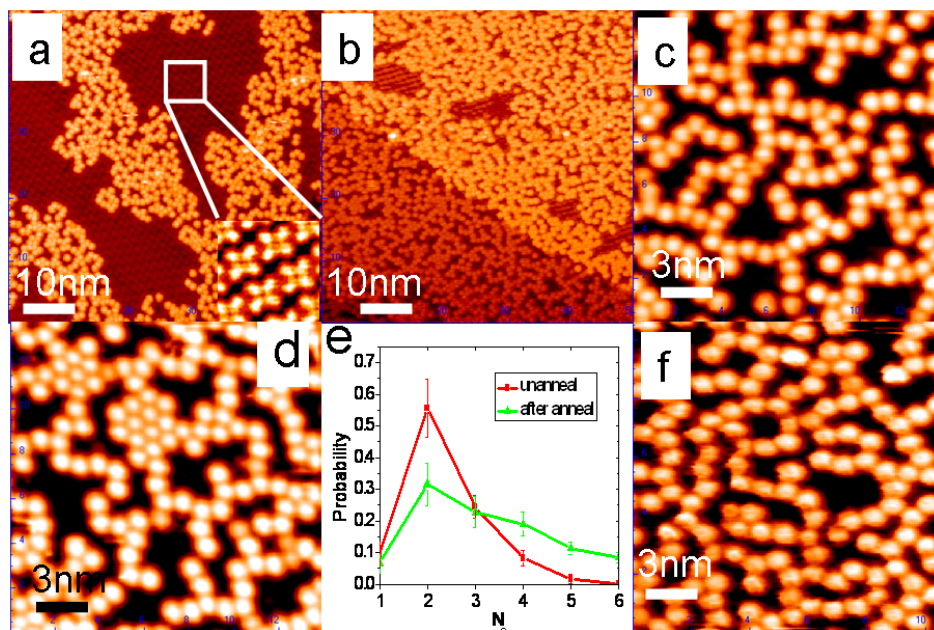


Figure 5.6 (a) STM image of 0.3 ML C_{60} /HD-ZnPc monolayer; Magnified inset shows bare HD-ZnPc region, confirming the lack of structural change; (b) 1 ML C_{60} /HD-ZnPc monolayer; (c) Molecularly resolved STM image shows quasi-linear C_{60} chains of single-molecule width; (d) Molecularly resolved STM image shows chain coarsening after annealing at 400 K; (e) Histograms of the coordination number (N_c) probability of C_{60} in unannealed samples (red) and annealed samples (green). The coordination number probability of unannealed sample (red) peaks at $N_c=2$, indicating the presence of linear structures. (f) Molecularly resolved STM image shows very similar quasi-linear C_{60} chains on pentacene bilayer support.

5.2.3.2. Molecular Dynamics Simulation

Since C_{60} wandering-chain structures are observed on multiple organic thin substrates, a general rule must govern this behavior. Similar spatial patterns involving a wide variety of physical systems, such as Langmuir monolayers [229], thin magnetic films [230], and physisorbed monolayers on solid surfaces [232], have been reported and attributed to a common mechanism: the competition of short-range attractive forces and long-range repulsions. In the present C_{60} system, there must also be a repulsive force between C_{60} molecules and inhibiting

aggregation into the high density close-packed structure. One possible origin of this repulsion is the induced dipole moment at organic-organic interfaces [33]. A simple Hamiltonian captures the essential features needed to describe the behavior of the above mentioned system.

$$H = -J \sum_{\langle R, R' \rangle} n_R n_{R'} + \frac{A}{2} \sum_{R, R'} \frac{n_R n_{R'}}{|R - R'|^3} \quad \text{Eq.(5.1)}$$

The first term in the above equation is the nearest neighbor attraction; the second term mimics the long-range dipole-dipole repulsion.

We perform Molecular Dynamic simulation of N=685 particles held in a plane (35 nm × 35 nm) at constant temperature T (room temperature) by Langevin dynamics,

$$\begin{aligned} \frac{d^2x}{dt^2} &= F_{ext} - m\gamma \frac{dx}{dt} + R \\ \langle R_i R_{i+\tau} \rangle &= 2m\gamma k_B T \delta(\tau) \end{aligned} \quad \text{Eq.(5.2)}$$

where x is the position coordination of one C₆₀ molecule, R is a random force that represents thermal fluctuations, which constantly inputs energy into the system and γ is the friction constant that takes kinetic energy away from the system. These forces keep the system fluctuating at temperature T . In the simulation, we treated 685 spherical particles as a dipole fluid by imposing permanent vertical dipole moments μ_i ($i=1 \dots N$) in the center of each C₆₀. F_{ext} is thus the total force between two particles i and j consisting of a Girifalco potential [233], dipole-dipole repulsion, and a perturbation term depending on the temperature.

The Girifalco potential is one of the simplest ways to describe C₆₀-C₆₀ interactions and has been shown to best reproduce the bulk phase [233]. If we only

think about the van der Waals interactions, then the interaction between two C₆₀ molecules can be seen as the summation of the Lennard-Jones interactions between two sets of 60 carbon atoms

$$V_G(r) = \sum_{i,j=1}^{60} \left(-\frac{A}{r_{i,j}^6} + \frac{B}{r_{i,j}^{12}} \right) \quad \text{Eq.(5.3)}$$

where A and B are L-J parameters. If we assume all these atoms are uniformly distributed on the C₆₀ sphere surface, then the potential can be written as:

$$V_G(r) = \sigma^2 \int_{1,2} dS_1 dS_x \left(-\frac{A}{r_{1,2}^6} + \frac{B}{r_{1,2}^{12}} \right) \quad \text{Eq.(5.4)}$$

r is the distance between two C₆₀ centers. σ is the carbon density distribution $\sigma = \frac{60}{S_1}$, and $\varphi(r_{1,2}) = \sigma^2 \left(-\frac{A}{r_{1,2}^6} + \frac{B}{r_{1,2}^{12}} \right)$ is the Lennard-Jones potential between two points with distance r_{12} on two C₆₀ surfaces, and the integration is over two C₆₀ sphere surface S_1 and S_2 . After the integrating, we get:

$$V_G(r) = -\alpha \left[\frac{1}{s(s-1)^3} + \frac{1}{s(s+1)^3} - \frac{2}{s^4} \right] + \beta \left[\frac{1}{s(s-1)^9} + \frac{1}{s(s+1)^9} - \frac{2}{s^{10}} \right] \dots \text{Eq. (5.5)}$$

where $s = \frac{r}{2a}$, $2a$ is 7.1 \AA , $\alpha = 4.68 \times 10^{-2} \text{ eV}$, $\beta = 8.48 \times 10^{-5} \text{ eV}$

The Girifalco potential has a well depth of $\sim 0.27 \text{ eV}$, as shown in Figure 5.7 (black line). This strong interaction makes the C₆₀ molecules stay together to form the close packed structure on most inorganic surfaces.

We use the Debye (D) as unit to describe dipole moment in this section. If we assume each C₆₀ carries a vertical dipole moment p , the repulsion between two vertical dipole moments is expressed as:

$$V_d = \frac{p^2}{4\pi\epsilon r^3} \quad \text{Eq.(5.6)}$$

where r is the distance between the two C_{60} molecule centers, ϵ is vacuum permittivity. In our simulation, we adjusted the value of p from 0 D to 25 D. One Debye corresponds to $3.336 \times 10^{-30} \text{ coulomb} \cdot \text{meter}$, equivalent to one electron charges separated by $\sim 0.02 \text{ nm}$.

The influence of the displacement magnitude on the net C_{60} - C_{60} interaction potential is shown in Figure 5.7. The dipole must have a value of 16.8 D to increase the effective C_{60} - C_{60} potential by $\sim 0.13 \text{ eV}$ at the nearest-neighbor distance of 1.0 nm. Simulations based upon this potential are shown in Figure 5.8: as the dipole p grows from 16.8 D to 23.8 D, the small close packed cluster disappears and the chains become more dominant.

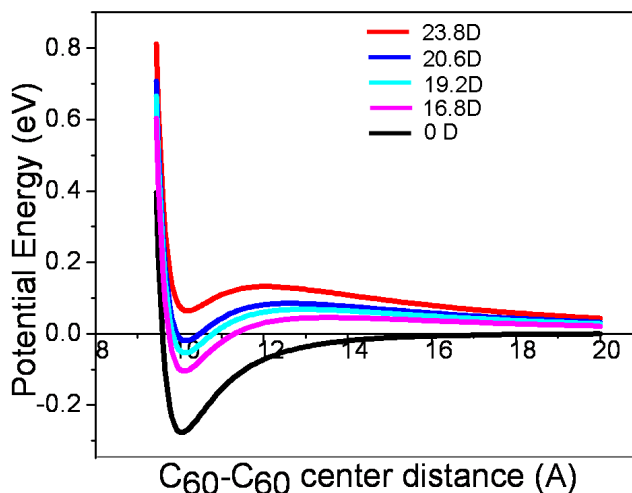


Figure 5.7 Effective C_{60} - C_{60} interaction: Girifalco potential with dipole-dipole repulsion

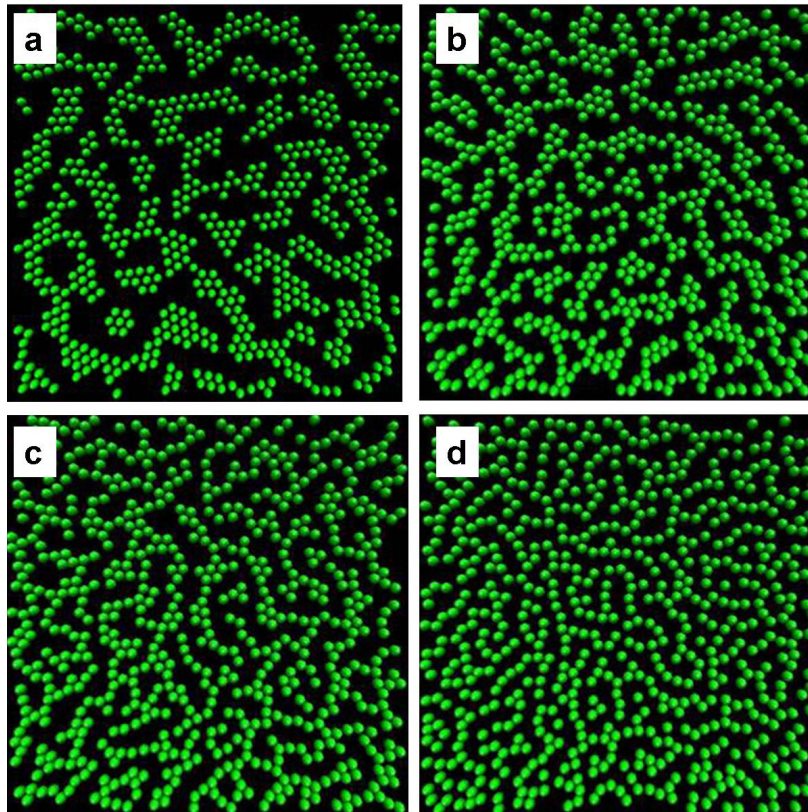


Figure 5.8 Simulated structures based upon the 2D dipole fluid potential with dipole values (N=685 particles in 35 nm×35 nm plane at room temperature): (a) 16.8 D; (b) 19.2 D; (c) 20.6 D; (d) 23.8 D. Substrate corrugation is excluded from the simulation. Snapshots are following 1.6×10^4 ps of elapsed time.

5.2.3.3. Measured-Simulated Structure Comparisons

We now present a more quantitative comparison between the measured chain-phase structure and the simulated results. The pair distribution function (PDF) is a useful tool to explore short-range ordered in system with long-range disorder. The PDF is given by the expression:

$$g(r) = \frac{1}{N^2} \sum_{i=1}^N \sum_{j=1}^N \langle \delta(|r_{ij}| - r) \rangle \dots \text{Eq. (5.7)}$$

where N is the number of C_{60} molecules and r_{ij} is the separation between the i -th

and j -th C_{60} molecules. The formation of $g(r)$ is determined by the energetic interactions between the C_{60} molecules. Of immediate relevance is the form of this function based upon interacting spherical dipolar particles [234, 235]. In Figure 5.9, we compare the PDF's obtained from experimental and simulated structure; the latter obtained with 23.8 D dipole spheres. Both PDF's are strongly peaked at the nearest-neighbor separation of 1 nm. Two additional peaks at 2 nm and 3 nm are observed, before the PDF decays to one. This loss of correlation is consistent with the measured branch length, noted above. Significantly, $g(r)$ maxima are located close to integer values of the molecular diameter, indicating the predominance of linear aggregation. Based upon the available data, a dipole fluid model with a simple Hamiltonian ($p=23.8$ D) reproduces the data well.

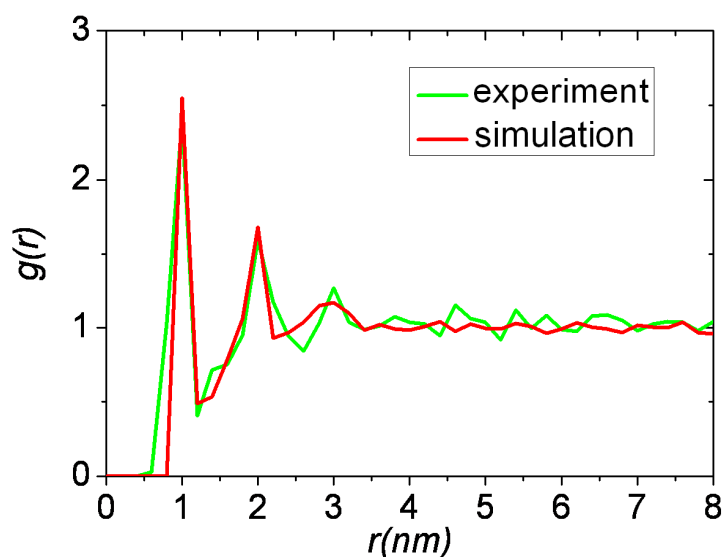


Figure 5.9 Pair distribution function $g(r)$ obtained from the molecular dynamic simulation performed with a dipole value of $p=23.8$ D (Figure 5.8.c) and from measurement. Experimental values are based upon the analysis of 3 samples and 11 images (corresponding to a total analyzed area of 4400 nm^2)

5.2.4. Discussion

The C_{60} meandering chain structures are reproduced with a model potential in which the attractive (Girifalco) potential between C_{60} molecules is balanced against a repulsive dipolar interaction between C_{60} . A substantial ~ 23 D value for each C_{60} is needed to reproduce the data.

Ishii *et al.* [33] first recognized that dipoles naturally occur at heterointerfaces between organic materials of greatly differing ionization energies and electron affinities (~ 0.5 eV offset). On the basis of work function and photoemission measurements, interfacial dipole has been reported for a number of systems [236]. The formation of an interfacial dipole between two organic layers originates from several dominant effects [237]: (1) the admixture of a charge transfer character in the ground state wavefunctions describing the donor-acceptor interface, a well known phenomenon described previously at the theoretical level [238-240]. (2) polarization of the electronic cloud within the molecules, resulting from interactions between all permanent and induced multipoles. (3) Pauli repulsion effect at small intermolecular distances, from the overlap of the wavefunctions of two neighboring molecules. This interaction is responsible for the well known “pillow effect” observed for molecules deposited on metals [241, 242].

In the present case involving C_{60} , we first assume the interface dipole is solely induced by charge transfer. For C_{60} in direct contact with Ag(111), there is a metal-to- C_{60} charge transfer of 0.8 electron [71]. Based upon the 0.3 nm C_{60} -Ag(111) distance [68], the interfacial dipole for directly adsorbing C_{60} is ~ 12

D. Based upon our simulations, a dipole of this magnitude would not inhibit the formation of the hexagonally close-packed monolayer. Moreover, on the metal surface, this dipole is well screened by the metallic substrate [243]. As a result, C_{60} molecules form close packed structures on Ag(111). Our chain phase structures suggest, however, that C_{60} molecules experience a much larger repulsive interaction when deposited on this organic film on the Ag(111) substrate. Certainly, the low carrier concentrations and slow dielectric relaxation in the organic thin film suppress the creation of an image charge allowing the dipole to retain its value (and repulsion). Therefore, dipole-dipole repulsion at organic-organic interfaces may be greater than on directly adsorbed silver.

Scanning tunneling spectroscopy measurements ($z(V)$) on C_{60} chains, reported in chapter 4, indicate that even a monolayer of a molecular semiconductor provides significant electronic decoupling of a second layer from the metal [188]. We thus utilize the simulation-derived dipole moment of 23 D to estimate the effective charge transfer to the C_{60} . The ZnPc layer is positioned 0.3 nm above the silver substrate [134, 244] while C_{60} is another 0.3 nm above ZnPc [245], placing the C_{60} -ZnPc separation at 0.6 nm. Based upon the dipole definition, $p = q \times r$, the 23 D corresponds to a charge transfer of 0.8 electron from the silver. This charge is comparable to the charge transfer for directly adsorbing C_{60} , suggesting that the ZnPc film may mediate charge transfer to the uppermost C_{60} layer.

However, this 23 D is regarded as an upperbound to the charge-transfer dipole, as it neglects the additional contribution of induced dipoles. Indeed,

quantum-chemical calculation [237] done for the tetrathiafulvalene (TTF)/tetracyanoquinodimethane (TCNQ) dimer, demonstrates that the net dipole involves significant polarization effects. Computations show the induced dipole moment is sensitive to geometric position of the dimer, i.e., the tilt angle or a lateral shift between the molecular centers. In contrast, the charge-transfer dipole, which produces the greatest the vacuum level shift, is independent of the tilt angle. Based upon the strong polarization of C_{60} and ZnPc, we may also expect an appreciable induced moment. The 0.8 electron metal-to- C_{60} charge transfer should thus be regarded as an upperbound to the actual charge transfer. Another contributing factor to the effective C_{60} - C_{60} repulsion is the elastic force due to the lattice mismatch between an adsorbed C_{60} and the underlying organic film. Indeed, the elastic case can be regarded as the tensorial generalization of the dipole repulsion problem treated here. The mechanical flexibility of organic thin films arises microscopically from weak interactions between the molecules. We note that ZnPc has a lower cohesive energy than C_{60} , and should thus be more susceptible to stress-driven reconstruction. Since ZnPc film (and pentacene film) remains intact upon C_{60} deposition, we conclude that interfacial stress is not driving the formation of the wandering chain phase. The formation of an interface is influenced by a large number of factors, and it is almost impossible to distinguish among all of them. For the present case, we model forces with an effective dipolar repulsion between C_{60} molecules. This effective dipole includes a dominant charge transfer term (estimated at 0.5 electron) and an additional dipole

term.

5.2.5. Conclusion

We observe wandering C_{60} chains on a variety of organic molecular films. Such filamentous structures are in complete contrast to C_{60} molecule's typical close-packed growth habit, but are reminiscent of dipole fluids. Chain structures are compared to the molecular dynamics predictions of a 2D dipole fluid with the C_{60} - C_{60} interaction described by the Girifalco potential with additional dipole terms. A vertical moment of ~ 24 D simulates filament formation. The wandering chains have been demonstrated to be once again due to the balance between short-range attractive interactions, such as the van der Waals attraction between the C_{60} molecules and long-range the dipolar repulsions, arising from the interactions between induced dipole or effective dipole from the unit mismatch between organic films and C_{60} . The results shown in this section provide clues for an understanding of the complex behavior at organic-organic interface. Although our simulation work is based on the simplest dipolar fluid model, we obtain a reliable estimate for the upperbound of charge transfer to C_{60} .

5.3. C₆₀-induced ZnPc Displacement: Formation of C₆₀-ZnPc Co-crystalline Monolayer

5.3.1. Introduction

Nanofabrication methods rely upon two seemingly disparate “top-down” and “bottom-up” approaches [159] to create patterns. Top-down methods essentially “impose” a structure or pattern on the substrate being processed via area-specific addition/removal of material whereas bottom-up methods guide the assembly of molecular building block into nanoscale architecture by utilizing local chemical properties of component molecules. Molecular programmed interactions such as hydrogen bonding [246-249], dipole-dipole [250], donor-acceptor [251, 252], van der Waals [253, 254], or metal coordinative [255, 256] interactions, support a rich variety of architecture with distinctive properties. The emphasis in self assembly has generally been placed upon the design of specific molecules for spatial organization. However, it is also worthwhile to borrow and adapt top-down concepts in self assembly. Here we utilize the “etch” concept on the molecular level to fabricate nanostructured C₆₀-ZnPc films. We show how zigzag networks can be reliably produced in a layer-by-layer growth that exploits differences in surface adsorption energies for self-limited etching.

5.3.2. Experimental

Low density ZnPc monolayers are first made by physical vapor deposition of ZnPc from a BN crucible at 660 K onto an Ag(111) substrate. Deposition is performed in a preparative chamber (base pressure $\sim 6 \times 10^{-8}$ Torr) and the sample is then transferred under vacuum into the UHV-STM chamber for structural analysis. Subsequent C₆₀ deposition is then performed from a Knudsen cell (T=650 K) within the UHV-STM chamber. To minimize damage to the organic films and preserve their structural integrity, local electronic properties were measured using constant current distance voltage spectroscopy ($z(V)$) [43, 144] with a constant tunneling current of 20 pA.

5.3.3. Result

In Chapter 3, we introduce the two ZnPc monolayer structures that readily form on Ag(111)- a low density (LD) monolayer phase and a high density (HD) monolayer. C₆₀ deposition on ZnPc both monolayer structures produces the wandering-C₆₀ chain phase, discussed in section 5.2, however, these two binary film structures have very different thermal stabilities.

The LD-ZnPc-supported chain phase undergoes a dramatic transformation upon 15 minutes annealing at 400 K. This layered binary structure rearranges into co-crystalline phase, consisting of C₆₀ zigzag chains in a ZnPc nanoscale array, Figure 5.10.a (The HD-ZnPc supported chain phase, in contrast, retains its

structure upon annealing. Figure 5.6.d) The C_{60} zigzag chains follow the substrate $[\bar{1}10]$ direction, Figure 5.10.b, and have a nearest-neighbor C_{60} spacing of 1.00 ± 0.02 nm and an internal zigzag angle of $\sim 120^\circ$. The chain-to-chain spacing is 1.52 ± 0.02 nm at the point of closest contact and 2.51 ± 0.02 nm at the most offset points, as shown in Figure 5.10.c. In the STM images, surface regions between C_{60} molecules appear dark. The unit cell of this structure, $a = 1.70 \pm 0.02$ nm, $b = 2.31 \pm 0.01$ nm, and $\theta = 65 \pm 2^\circ$, corresponding to a C_{60} molecule density of 0.58 molecule/nm². This C_{60} density is thus comparable to that of the meandering- C_{60} chains phase from which it is formed. This co-crystalline zigzag structure is commensurate with the Ag(111) surface.

The transformation matrix is $\begin{bmatrix} a \\ b \end{bmatrix} = \begin{bmatrix} 6 & 0 \\ -1 & 8 \end{bmatrix} \begin{bmatrix} a_{Ag} \\ b_{Ag} \end{bmatrix}$, where the lattice vectors for silver are $a_{Ag} = b_{Ag} = 2.89 \text{ \AA}$.

As previously described, the surface area initially covered by the C_{60} -wandering chain phase is determined by the coverage of C_{60} . At lower C_{60} coverage, where only $\sim 30\%$ of the surface is covered by the C_{60} chain phase, large regions of ZnPc are exposed. Upon thermally annealing these samples, the surface phase separated into two regions: the co-crystalline zigzag phase and the HD-ZnPc phase (Figure 5.10.a). Evidently, the ZnPc molecules expelled during the formation of the co-crystalline phase are accommodated in the formally LD-ZnPc phase, allowing transformation into the HD-ZnPc structure. Evidence for this transformation is the appearance of the three 120° rational domains, reflecting the 3-fold symmetry of Ag (111) substrate.

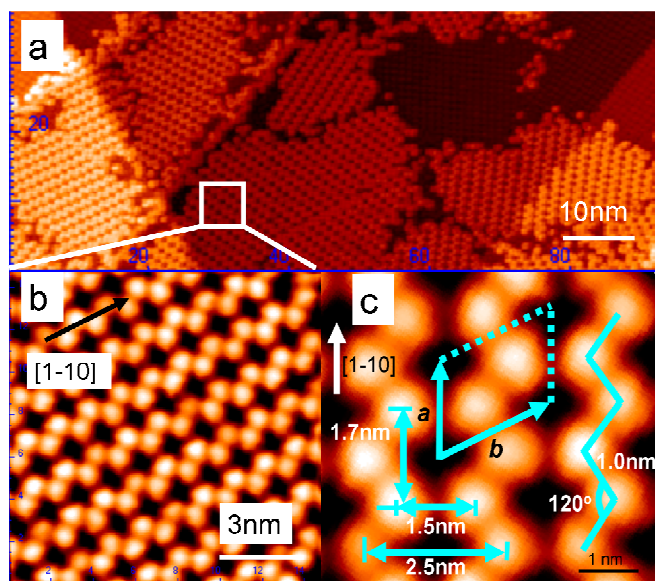


Figure 5.10 (a) STM image of surface structure following the annealing of a binary film consisting of a C_{60} wandering phase supported on a LD-ZnPc monolayer. ($T=400$ K, $t=15$ minutes). Domains of the co-crystalline zigzag network coexist with the HD-ZnPc monolayer (b) Magnified STM image of the co-crystalline structure. (c) Structural parameters for the array superimposed on the STM image.

The co-crystalline structure is commensurate with Ag(111) and thus presumed to be a monolayer structure in direct contact with the Ag(111) surface. The direct chemisorption of C_{60} is now verified with tunneling microscopy, performed in constant-current distance-voltage mode ($z(V)$) at room temperature. The spectral data in Figure 5.11 shows a peak in the tunneling spectrum, assigned to the highest occupied molecular orbital (HOMO) of C_{60} . The spectra for the pure C_{60} component films, the hexagonal C_{60} monolayer (*red*) is used as a spectral reference. The HOMO of C_{60} in zigzag chains of the co-crystalline phase (*green*) is at the same -1.9 eV energetic position as the monolayer phase. This is direct evidence that the C_{60} molecules are directly bonded to the substrate, as the HOMO levels are extremely sensitive to the proximity to the Ag(111) surface. By comparison, the C_{60} HOMO level for the wandering chain phase on ZnPc (Figure

5.6.c) (blue) is shifted towards much higher energies (-2.4 eV) due to the reduction in polarization energy. This upward shift is also observed for C₆₀ straight chains supported on the pentacene bilayer [188].

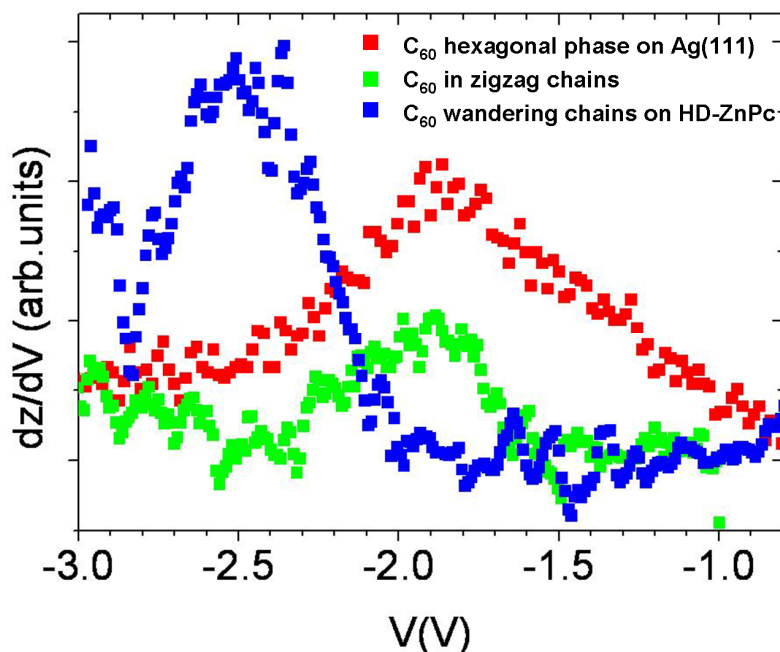


Figure 5.11 Comparison of dz/dV local tunneling spectra for C₆₀ zigzag structure (green), C₆₀ meandering chains on ZnPc monolayer (blue) and reference C₆₀ close-packed island (red) on Ag(111). Energy alignment of 1.9 eV HOMO feature confirms direct C₆₀-Ag (111) contact in zigzag chains. Spectra acquired with initial tunneling condition of -1.27V and 0.05nA.

The structural model for the co-crystalline phase (zigzag structures) is displayed in Figure 5.12. From our model, the stoichiometry of this co-crystalline structure is (C₆₀)₂ZnPc. We assume that the C₆₀ hexagon resides at the energetically preferential hollow sites of the Ag substrate [68]. Taking into account C₆₀ pore size and the curvature of C₆₀, we deduce that ZnPc molecules lie flat in the interstitial regions. Unfortunately, the high contrast (height variation) of

C_{60} relative to ZnPc precludes direct imaging of ZnPc molecules. Because of the finite size of the STM tip, the tip will simultaneously tunnel through the ZnPc while the side of the tip tunnels through C_{60} . By considering symmetry, we select the orientation of ZnPc that aligns the aromatic ZnPc axis with the substrate $[\bar{1}10]$ direction, as observed in the HD-ZnPc phase. However, given the large distance between neighboring ZnPc molecules (1.73 nm in zigzag chains; 1.68 nm in the bulk phase) and the room temperature conditions, free rotation of the ZnPc molecules is a distinct possibility. Such free rotation would further account for the difficulty of imaging ZnPc in this phase.

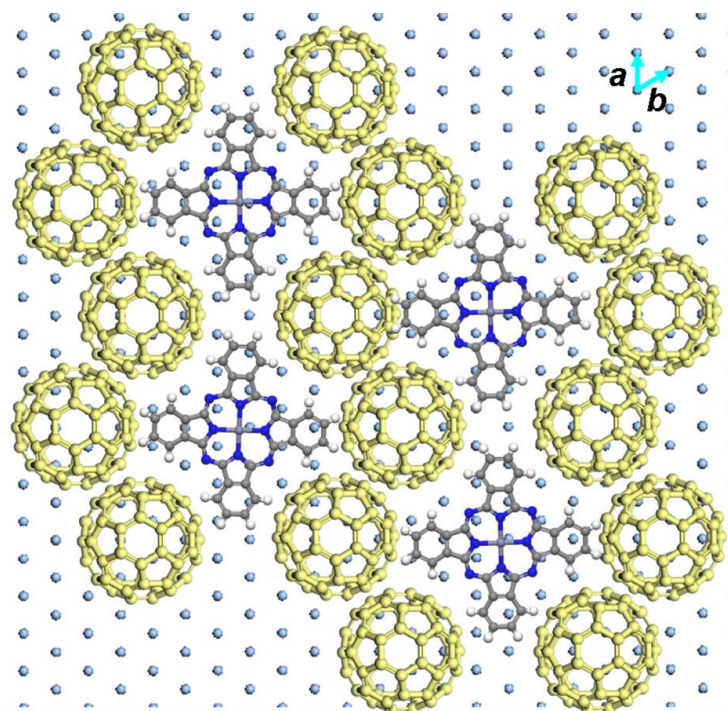


Figure 5.12 Proposed structural models for the co-crystalline C_{60} -ZnPc phase, consisting of C_{60} zigzags arrays

5.3.4. Discussion

We observe the transformation of a $C_{60}/ZnPc$ bilayer structure into a co-crystalline monolayer phase. During this thermal transformation, the C_{60} chains displace ZnPc molecules with a LD-ZnPc monolayer, while increasing the ZnPc density in the surrounding region. This reactive etching mechanism is depicted schematically in Figure 5.13: Phthalocyanine molecules in the LD-phase (Figure 5.13.a) are bound to Ag (111) by relatively weak van der Waals interactions. At room temperature, C_{60} deposition results in the forming of a bilayer, consisting of the LD-ZnPc bottom layer and the C_{60} wandering chain phase top layer (Figure 5.13.b). Thermal activation of ZnPc displacement by C_{60} then occurs. Due to strong intermolecular C_{60} - C_{60} attractions in chains, it appears that the wandering chains remain connected and break through the ZnPc bottom layer (Figure 5.13.c). Such a molecular displacement is expected only if the adsorption of the displacing molecule exceeds that of the displaced molecule [196]. The thermal energy further allows the chain to align with the Ag (111) to realize its preferred $\langle 110 \rangle$ alignment with the substrate. The annealing temperature is sufficient for ZnPc diffusion and desorption from the ZnPc second layer.

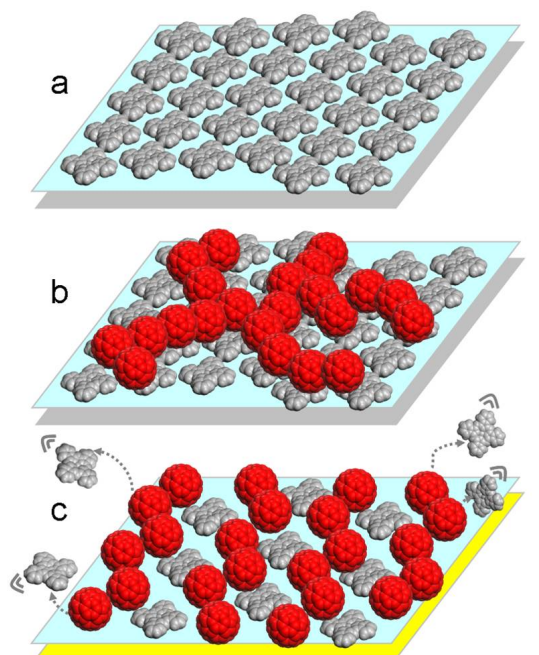


Figure 5.13 Schematic illustration of 2D co-crystalline formation mechanism upon C_{60} displacing ZnPc after annealing.

5.3.5. Summary

We have investigated the formation of a 2D co-crystalline structure made of C_{60} :ZnPc. The structure is produced by the effective etching of the LD-ZnPc monolayer by the C_{60} chain-phase under thermal activation. This study demonstrated that a well-defined the structure with a nanoscale repeat pattern can be readily formed by exploiting differences in chemisorption energies and relatively weak intermolecular interactions. This etching-assembly approach is complementary to the molecular programmed self-assembly approach, where chemical groups are often employed to direct pattern formation.

6. Chapter 6 Binary system: ZnPc:F₁₆ZnPc

The ZnPc and F₁₆ZnPc single component properties are discussed in chapter 3. In this chapter, I will discuss binary ZnPc:F₁₆ZnPc films. This work has been submitted to The Journal of Physical Chemistry C. Collaborating with Professor Marco Buongiorno Nardelli from North Carolina State University, a paper on DFT calculations has been submitted to The Journal of Physical Chemistry C.

6.1. Introduction

Intermolecular interactions at surfaces drive rich structural diversity that promises exciting applications of molecular nanoscience [159]. In particular, aromatic coordination complexes, such as metal-phthalocyanine (MPc), deposited on metal substrates are prototypical models of semiconductor/metal interfaces for molecular electronics applications [24].

Despite the enormous interest that these ideas have spawned in recent years, it remains unclear whether structural diversity translates to functional diversity, especially when intermolecular interactions are noncovalent. Moreover, the effect of the molecule-substrate interaction is not completely understood and the potential role of the interface in tailoring the electronic properties of the assembly remains to be explored. It is thus important to investigate situations where

intermolecular interactions and/or substrate-mediated interactions have dramatic consequences for the electronic structure of molecular assemblies and can be used for the tailoring of surface properties for advanced supramolecular design.

Metal phthalocyanines are useful materials for organic thin film electronics due to their chemical stability, electronic and optical properties, and film quality [110]. As discussed in chapter 3, single component ZnPc and F₁₆ZnPc films on Ag(111) follow structural trends established for MPc film growth on a variety of substrates including HOPG [140], MoS₂ [122], Au(111) [123, 125], “5 × 20” Au(001) [128, 129], and Ag(111) [134, 137]. Both molecules readily form ordered structures that are incommensurate with Ag(111). The monomolecular arrangements in these incommensurate phases are largely dictated by the molecule-molecule interaction.

We now explore the relationship between film structural organization and film electronic structure in films assembled from ZnPc and F₁₆ZnPc. Assemblies of two molecules with virtually identical size and shape, but with offset electronic states and opposing electrical transport characteristics, are intriguing from the perspective of structure-property correlations. Previously F₁₆CoPc and Ni tetraphenylporphine were found to display perfect intermixing, where donor and acceptor species alternated from site to site in an ordered 2D array [257]. We now probe the impact on electronic structure of molecular-level intermixing for the case of ZnPc and F₁₆ZnPc, comparing the co-crystalline film results to those of single-component films.

6.2. Experimental

ZnPc and F₁₆ZnPc were co-deposited onto Ag(111) from two BN crucibles at 660K and 680K, respectively, at a typical rate of 0.25 ML/min and then transferred under vacuum to the STM chamber.

6.3. Result

6.3.1. Structural Information

Co-deposited, ZnPc and F₁₆ZnPc spontaneously organize into a highly ordered two dimensional superlattice. As shown in Figure 6.1.a, this superlattice exhibits few structural defects and extends over large domains, crossing silver steps without interruption. Molecularly resolved images (Figure 6.1.b) reveal a checkerboard pattern, in which ZnPc and F₁₆ZnPc are alternatively arranged along the substrate $[\bar{1}10]$ and $[\bar{1}1\bar{2}]$ directions. The bright molecule is tentatively assigned to F₁₆ZnPc, based upon the energetic ordering of HOMO levels, described below. This bright/dim contrast is observed across a wide -1.5 V ~ 1.5 V tip bias range. One supramolecular unit cell ($a = 2.03 \pm 0.02$ nm, $b = 2.01 \pm 0.02$ nm, $\theta = 89 \pm 1^\circ$) is superimposed on the image, indicating a molecular packing density of 0.49 molecules/nm².

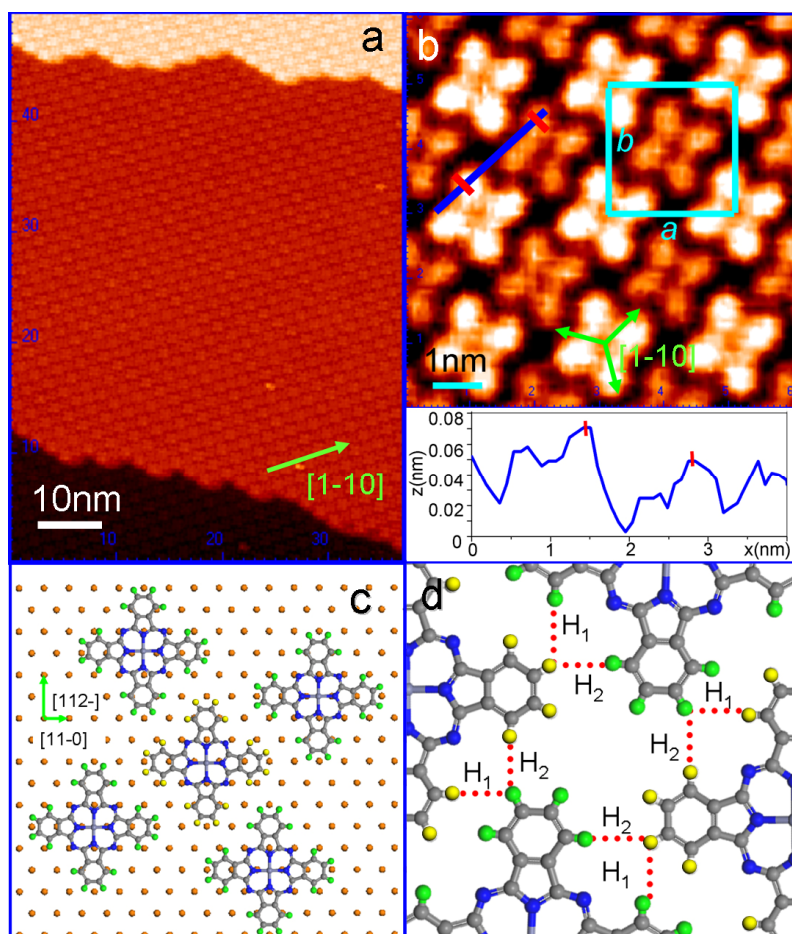


Figure 6.1(a-b) STM images of ZnPc: F_{16} ZnPc intermixed monolayer. Topographic profile along dark blue line shown in inset. (c) Structural model of commensurate checkerboard phase. Registration to Ag(111) determined with the assistance of a $(2\sqrt{3} \times 2\sqrt{3})R30^\circ$ - C_{60} calibrant (not shown). (d) Molecular neighbors in checkerboard show two C-F...H separations, H_1 (285 pm) and H_2 (298 pm) with ± 20 pm uncertainty

Images with submolecular resolution show one of the long axes of each molecule (i.e. phenyl ring axis) aligned with the close-packed substrate $[1\bar{1}0]$ direction. Thus, ZnPc and F_{16} ZnPc occupy identical adsorption sites on the silver surface. A model for the checkerboard structure is provided in Figure 6.1.c. Precise registration with respect to the Ag(111) was determined with the assistance of an internal C_{60} molecular calibrant. Specifically, we prepared $(2\sqrt{3} \times 2\sqrt{3})R30^\circ$ C_{60} islands in coexistence with the checkerboard structure on

Ag(111). We then utilized the well known registration of C_{60} with respect to Ag(111) [68] to deduce ZnPc and F_{16} ZnPc registration in the checkerboard.

Within the checkerboard structure, neighboring molecules (Figure 6.1.d) show two inequivalent C-F...H separations, 285 ± 20 pm and 298 ± 20 pm based on 15 measurements. These separations are well within the expected range of hydrogen bonds and are nearly identical to those reported for F_8 ZnPc on Ag(111) [258]. Table 6.1 summarizes parameters for all observed ZnPc, F_{16} ZnPc monolayer structures and checkerboard structure.

Table 6.1 Primitive Vector Parameter of the adsorbed overlayer with respect to Ag(111)*

Structure		ZnPc		F ₁₆ ZnPc alternating row		Checkerboard
		LD	HD			
Primitive Vector	<i>a</i> (nm)	1.56	1.35	1.50	1.50	1.45
	<i>b</i> (nm)	1.25	1.33	1.63	1.75	1.50
	θ	83	88	84	65	90
Matrix		$\begin{pmatrix} 5.4 & 0 \\ 0.5 & 2.5 \end{pmatrix}$	$\begin{pmatrix} 4.7 & 0 \\ 0.2 & 2.6 \end{pmatrix}$	$\begin{pmatrix} 5.2 & 0 \\ 0.6 & 3.2 \end{pmatrix}$	$\begin{pmatrix} 5.2 & 0 \\ 2.6 & 3.2 \end{pmatrix}$	$\begin{pmatrix} 5 & 0 \\ 0 & 3 \end{pmatrix}$
Substrate Registration		Incommensurate —point on line	Incommensurate —point on line	Incommensurate —point on line	Incommensurate —point on line	Commensurate
Molecular Packing Density (molecules/nm ²)		0.51	0.55	0.41	0.41	0.49

*The primitive vectors for Ag(111) surface along $[\bar{1}10]$ and $[\bar{1}12]$ directions with the nearest neighbor distances.

6.3.2. Electronic Energy Levels

Scanning Tunneling Spectroscopy (*z*-*V*) measurements were performed on both the single-component (Figure 6.2.a) and checkerboard monolayer (Figure 6.2.b). For the single component molecular films, the occupied state resonances are observed at -1.5 eV (ZnPc) and -1.4 eV (F₁₆ZnPc) and are attributed to the HOMO's. Unoccupied states appear at 1.5 eV (ZnPc) and 1.3 eV, (F₁₆ZnPc), but we cannot rule out additional electronic states at lower energies due to limited signal-to-noise at low and positive voltages. These HOMO levels, and their relative positions, are consistent with ultraviolet photoelectron spectra (UPS) for closely related systems: Cl₈ZnPc/Ag(111) [259], F₄CuPc/Ag(111) [260], and CuPc and F₁₆CuPc/Au [261].

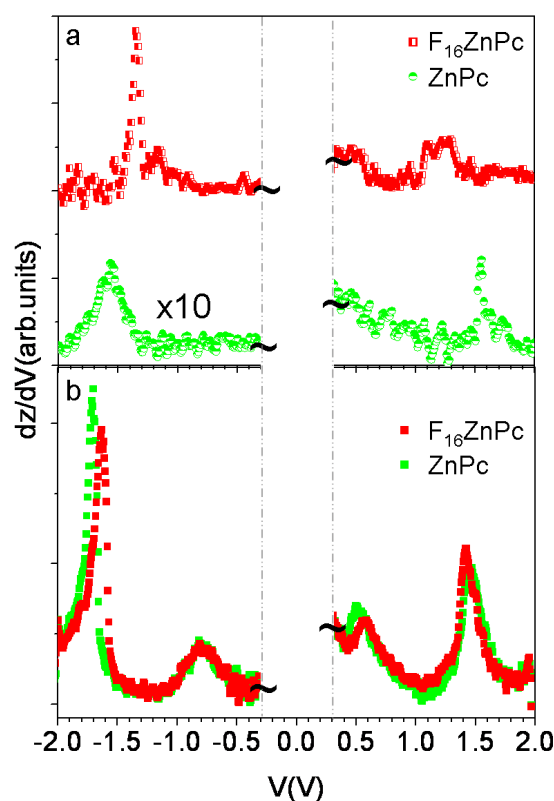


Figure 6.2 Tunneling spectra acquired in z - V mode:(a) Single component monolayer phases: For occupied molecular state: ZnPc (green) trace averages 14 sweeps at 50 pA from -0.910 V initial bias F₁₆ZnPc (red) trace averages 27 sweeps at 60 pA from -1.000 V initial bias. For unoccupied molecular state: ZnPc (green) trace averages 10 sweeps at 50 pA from -0.834 V initial bias; F₁₆ZnPc (red) trace average 10 sweeps at 50 pA from -0.839 V initial bias. (b) Intermixed Checkerboard phase: traces average 40 sweeps at 40 pA with initial -0.839 V bias for both occupied molecular state and unoccupied state ZnPc (green) and F₁₆ZnPc (red) traces acquired by separately positioning the tip over the dim and bright image features

In the intermixed checker phase, local spectroscopy measurements are separately performed over both bright and dim molecules. The HOMO positions, dim (-1.75 eV) and bright (-1.65 eV), are shifted from those of pure ZnPc (-1.5 eV) and F₁₆ZnPc (-1.4 eV) films. These features are assigned to ZnPc (dim) and F₁₆ZnPc (bright), respectively, on the basis of energetic ordering. Most significant is the appearance of a pronounced electronic state in the checkerboard structure

for *both* species at -0.8 eV, indicating a delocalization over the supramolecular structure. This state is not detected on pure ZnPc or pure F₁₆ZnPc films. Unoccupied states at 0.55 eV and 1.5 eV are also observed for this stable checkerboard film.

6.4. Discussion

Single component ZnPc and F₁₆ZnPc films follow structural trends established for MPc film growth on a variety of substrates including HOPG, MoS₂ [122], Au(111) [123, 125], “5 × 20” Au(001) [128, 129], and Ag(111) [134]. On these surfaces, MPc molecules also readily form ordered structures that are incommensurate with the substrate. The monomolecular arrangements in these incommensurate phases are largely dictated by the molecule-molecule interaction. Effectively the MPc-surface interaction, though involving a charge transfer, does not appear to be highly directional.

The checkerboard structure allows the long (phenyl) axes of both MPc molecules to run along the nearest- and next-nearest directions of the Ag(111) lattice. Moreover, the precise registration centers the carbocyanine macrocycle on a silver atom, effectively overlapping a 7-atom cluster on the Ag(111) substrate. This indicates a stronger chemisorption interaction with the substrate, and is consistent with the more stable STM imaging. This stronger chemisorption interaction further accounts for H...F hydrogen bond lengths of 285 pm (H₁) and

298 pm (H₂) which are ~10% longer than the typical H...F bond length of 260 pm [262, 263]. This molecular arrangement is nearly identical to that reported for F₈ZnPc [258] in which DFT-computed intermolecular spacing for F₈ZnPc also yielded two elongated H...F hydrogen bonds (281 pm and 290 pm). Evidently, the chemisorption interaction with the substrate is compensating the supramolecular arrangement for the energetic cost of stretching the hydrogen bonds.

Electronic states on the commensurate checkerboard structure are delocalized over both ZnPc and F₁₆ ZnPc components, as evidenced by the newly occupied state at -0.8 eV. Checkerboard bands at -1.6 eV and 1.5 eV appear correlated to single-component states at similar energies (-1.4 eV and 1.4 eV for F₁₆ZnPc and -1.6 eV and 1.6 eV for ZnPc). Charge-transfer from the substrate was previously observed for F₄CuPc on Ag [260]. UPS studies of neat subfluorinated phthalocyanines have similarly reported “interface states” associated with substrate-molecule interaction, but at much lower binding energies compared to the new state in our checker phase [259, 260]. We propose the new state arises from a partial filling of the molecular LUMO. The low-energy states for checkerboard structures involve a diffuse metal-to-LUMO charge transfer. This metal-to- π interaction partially broadens the molecular bands, but the phthalocyanines essentially retain the electronic characteristics of the discrete molecules. The delocalized π character of the frontier orbitals interact with the broad s-band of silver, which act as a surface free electron gas. This gives rise to a weak but persistent charge transfer from the metal to the molecules that result in

the occupation of the MPc's LUMO and the stabilization of the adlayer. This weak-and-extended coupling mechanism has been previously proposed for π -conjugated molecules such as PTCDA and C_{60} absorbed on the noble metal surface through a rearrangement of the π -electron systems [68, 264, 265].

6.5. Summary

We have compared the structural and electronic characteristics of single-component and binary monomolecular films of ZnPc and F_{16} ZnPc. Co-deposition of ZnPc and F_{16} ZnPc results in an intermixed “checkerboard” phase. Unlike the single-component phases, the binary phase is commensurate with the substrate and is stabilized by both chemisorption and an H...F hydrogen bond network with elongated H...F bonds, relative to those typically observed in molecular systems. This checkerboard structure gives rise to a new low energy state, delocalized over both species. This interface state involves a diffuse metal to LUMO charge transfer. The more robust ZnPc: F_{16} ZnPc checkerboard structure facilitates the detection of this state in room temperature STS measurements.

7. Chapter 7 Summary and Outlook

Since the time I have initiated this dissertation research, multi-component organic molecular films have seen increasing application in photovoltaic technologies and other organic electronic applications. These applications have been based upon unverified assumptions regarding film structure and electronic properties. This thesis provides an increased understanding of factors that control structure in binary molecular films and begins to establish structure-electronic property relations across donor-acceptor interfaces. In this thesis, three technologically relevant “donor-acceptor” systems are studied with variable temperature STM/STS: pentacene (Pn):C₆₀, zinc phthalocyanine (ZnPc): C₆₀ and zinc phthalocyanine (ZnPc) and perfluorinated zinc phthalocyanine (F₁₆ZnPc). These three model systems provide a systematic exploration of the impact of molecular *shape* and molecular *band offset* on morphology-electronic relations in thin film heterostructures.

In this thesis, I have demonstrated how domain size and chemical morphology are controlled by composition and film processing conditions. I also show how single component phase diagrams may be more generally exploited to selectively prepare binary film architectures. I perform “non-destructive” $z(V)$ spectroscopy at room temperature and show that the electronic transport gap is influenced by polarization energies that depend explicitly upon the local chemical environment,

such as the number of nearest neighbors and orientation-dependent polarizabilities. The $z(V)$ technique has been shown to provide accurate value of energy levels within ~ 6 eV of E_f at room temperature. The $z(V)$ measurement is thus a useful tool to characterize molecular interfaces.

Some general observations are outlined below:

- (1) Organic binary co-crystalline films (pentacene: C_{60} and ZnPc: C_{60}) are kinetically accessible by exploiting the relative differences in the component cohesive energies to the substrate. By utilizing sequential deposition, the component with lower absorption energy is deposited first, and then the more strongly adsorbing component, C_{60} selectively displaces the first component. The final structure is stabilized by weak anisotropic interactions. This kinetic route to assembly is different from supramolecular directional bond (hydrogen and halogen bonds) approaches and surface templated assembly. This mechanism may be quite general, giving an additional method for the rational design of complex nanoscale architecture.
- (2) C_{60} wandering chains form on a variety of organic thin film substrates. These single-molecular-width chains are simulated with a model that balances short-range attraction (Girifalco potential) and long-range repulsion. An effective dipole moment of 23 D suggests that substantial charge redistribution accompanies C_{60} adsorption on organic films.
- (3) Local tunneling spectroscopy on the supported C_{60} wandering chains shows that the HOMO and LUMO levels are significantly shifted from their bulk

values. This indicates polarization energies that depend explicitly upon local chemical environment, such as the number of nearest neighbor. A higher packing density along the donor-acceptor interface would have a more effective charge screening effect and result in a lower charge injection barrier. This suggests that higher packing density along donor-acceptor interface is a desirable configuration for avoiding “polarization barriers” in organic photovoltaic applications

- (4) The ZnPc:F₁₆ZnPc checkerboard structure gives rise to a new low energy state, delocalized over both species. This state involves a charge transfer from the metal substrate to the molecule’s LUMO. This indicates the important role the substrate plays.

Overall, this research has developed methods in controlling chemical morphology along the donor-acceptor interface, and understanding of how this morphology influences electronic transport. While the experiments and studies described in this thesis looked only at monolayer and bilayer films, thick films involving three dimensional interfaces are, of course, the most relevant for heterostructure operation. However, STM can not easily measure the buried structure of 3D donor-acceptor interfaces that are directly relevant for photovoltaic devices. Kelvin probe force microscopy would be a good tool to overcome the thickness limitation. Also, due to the instability of the room temperature tunneling junction, the useful voltage ranges for the $z(V)$ studies is $|V_{bias}| \geq 0.5$ V. Performing

spectroscopy measurements at lower temperatures, where the tunneling junction will be more stable, would allow us to extend the usable voltage range for spectroscopy to within 100mV of the Fermi level. A combination of ultraviolet photoelectron spectroscopy (UPS), inverse photoelectron spectroscopy (IPES) and two-photon photoelectron spectroscopy (2PPES) would provide more detailed electronic information on dynamical aspect of exciton dissociation, such as the influence of the donor-acceptor interface on exciton lifetime, rate of exciton diffusion, and the influence of electrostatic fields near the interface. With the protocols for sample preparation determined in the STM studies, more comprehensive electronic information can be derived. Such experiments are already underway at NIST. Structural models deduced from the images, such as relative orientation and separation of the donor and acceptor molecules, can be used as an input for further calculations to understand the nature of the intermolecular forces that determine the architectures.

Based upon results in this thesis, I proposed two particularly interesting experiments that could be done by STM:

1. It would be of interest to investigate interfacial electronic and molecular structure through the use of a third molecular component in a system such as pentacene-C₆₀ dyad. By sequential deposition, the dopants could decorate the donor-acceptor interfaces and increase packing density. $z(V)$ measurement at the dopant sites and also at the domain boundaries could reveal the packing density effect on electronic structure.

2. C₆₀ wandering chain formation on top of organic thin films is particularly interesting. In this work, the effective dipole derived from calculation is about ~23 D, compared with ~12 D in C₆₀ on bare silver. To further investigate the origin of this dipole, more polarizable molecules, such as C₇₀, deposited on the same organic thin films could be used.

REFERENCES:

- [1] Garnier F, Yassar A, Hajlaoui R, Horowitz G, Deloffre F, Servet B, *Molecular engineering of organic semiconductors: design of self-assembly properties in conjugated thiophene oligomers*, Journal of the American Chemistry Society, 1993, **115(19)**: p. 8716-21.
- [2] Stewart M, Howell R.S, Pires L, Hatalis M.K, *Polysilicon TFT technology for active matrix OLED displays*, IEEE Transactions on Electron Devices, 2001, **48(5)**: p. 845-51.
- [3] Forrest S.R, Burrows P.E, Shen Z, Gu G, Bulovic V, Thompson M.E, *The stacked OLED (SOLED): a new type of organic device for achieving high-resolution full-color displays*, Synthetic Metals, 1997, **91(1-3)**: p. 9-13.
- [4] Sugimoto A, Ochi H, Fujimura S, Yoshida A, Miyadera T, Tsuchida M. *Flexible OLED displays using plastic substrates*, IEEE Journal of Selected Topics in Quantum Electronics, 2004, **10(1)**: p.107-14.
- [5] Klauk H, Gundlach D.J, Nichols J.A, Jackson T. *Pentacene organic thin-film transistors for circuit and display applications*. IEEE Transactions on Electron Devices, 1999, **46(6)**: p.1258-63.
- [6] Gundlach D.J, Lin Y.Y, Jackson T.N, Nelson S.F, Schlom D.G. *Pentacene organic thin-film transistors-molecular ordering and mobility*, Electron Device Letters IEEE, 1997, **18(3)**: p.87-9.
- [7] Ong B.S, Wu Y, Liu P, Gardner S, *High-Performance Semiconducting Polythiophenes for Organic Thin-Film Transistors*, Journal of the American Chemistry Society, 2004, **126(11)**: p.3378-9.
- [8] Tang C.W, *Two-layer organic photovoltaic cell*, Applied Physics Letters. 1986, **48(2)**: p.183-5.
- [9] Nelson J, *Organic photovoltaic films*, Current Opinion in Solid State and Materials Science, 2002, **6(1)**: p.87-95.
- [10] Friend R.H, Gymer R.W, Holmes A.B, Burroughes J.H, Marks R.N, Taliani C, *Electroluminescence in conjugated polymers*, Nature. 1999, **397(6715)**:p.121-8.
- [11] Brabec C.J, Sariciftci N.S, Hummelen J.C, *Plastic Solar Cells*, Advanced Functional Materials, 2001, **11(1)**: p.15-26.
- [12] Peumans P, Uchida S, Forrest S.R, *Efficient bulk heterojunction photovoltaic cells using small-molecular-weight organic thin films*, Nature, 2003, **425(6954)**: p.158-62.
- [13] Brian A.G, Mark C.H, *Comparing organic to inorganic photovoltaic cells: Theory, experiment, and simulation*, Journal of Applied Physics, 2003, **93(6)**: p.3605-14.
- [14] Hoppe H, Sariciftci N.S, *Organic solar cells: An overview*, Journal of Material Research, 2004, **19(7)**: p.1924-45.
- [15] Liu A, Zhao S, Rim S.B, Wu J, Konemann M, Erk P, *Control of electric field strength and orientation at the donor-acceptor interface in organic solar cells*, Advanced Materials, 2008, **20(5)**: p.1065-70.

- [16] Sariciftci N.S, Smilowitz L, Heeger A.J, Wudl F, *Photoinduced electron transfer from a conducting polymer to buckminsterfullerene*, Science, 1992, **258(5087)**: p.1474-6.
- [17] Schwartz B.J, *Conjugated polymers as molecular materials: how chain conformation and film morphology influence energy transfer and interchain interactions*, Annual Review of Physical Chemistry, 2003, **54(1)**: p.141-72.
- [18] Moons E, *Conjugated polymer blends: linking film morphology to performance of light emitting diodes and photodiodes*, Journal of Physics: Condensed Matter, 2002, **14(47)**: p.12235-60.
- [19] Padinger F, Rittberger R.S, Sariciftci N.S, *Effects of postproduction treatment on plastic solar cells*, Advanced Functional Materials, 2003, **13(1)**: p.85-8.
- [20] Coakley K.M, McGehee M.D, *Conjugated polymer photovoltaic cells*, Chemistry of Materials, 2004, **16(23)**: p.4533-42.
- [21] Liam S.C.P, Obadiah G.R, David S.G, *Electrical scanning probe microscopy on active organic electronic devices*, Advanced Materials, 2009, **21(1)**:p.19-28.
- [22] M.Pope, *Electronic process in organic crystals and polymers*, Oxford University Press, New York, 1999.
- [23] R.Farchioni, *Organic electronic materials: conjugated polymers and low molecular weight organic solids*, Springer, Berlin, 2001.
- [24] Gregor W, Christof W, *Growth of Aromatic Molecules on Solid Substrates for Applications in Organic Electronics*, ChemInform, 2004, **35(51)**:
- [25] Sullivan P, Jones T.S, *Pentacene/fullerene (C₆₀) heterojunction solar cells: Device performance and degradation mechanisms*, Organic Electronics, 2008, **9(5)**:p.656-60.
- [26] Yang J, Nguyen T-Q, *Effects of thin film processing on pentacene/ C₆₀ bilayer solar cell performance*, Organic Electronics, 2007, **8(5)**: p.566-74.
- [27] Cheyng D, Gommans H, Odijk M, Poortmans J, Heremans P. *Stacked organic solar cells based on pentacene and C₆₀*, Solar Energy Materials and Solar Cells, 2007, **91(5)**: p.399-404.
- [28] Pandey A.K, Nunzi J-M, *Efficient flexible and thermally stable pentacene/C₆₀ small molecule based organic solar cells*, Applied Physics Letters, 2006, **89(21)**: p.213506-3.
- [29] Bernstein J, *Polymorphism in molecular crystals*, Oxford University Press, New York, 2002.
- [30] Romaner L, Nabok D, Puschnig P, Zojer E, Ambrosch-Draxl C. *Theoretical study of PTCDA adsorbed on the coinage metal surfaces, Ag(111), Au(111) and Cu(111)*, New Journal of Physics, 2009, **11(5)**: p.053010.
- [31] Hooks D.E, Fritz T, Ward M.D, *Epitaxy and molecular organization on solid substrates*, Advanced Materials, 2001, **13(4)**: p.227-41.
- [32] Slawomir B, William R.S, Mats F, *Energy-level alignment at organic/metal and organic/organic interfaces*, Advanced Materials, 2009, **21(14-15)**:p.1450-72.
- [33] Hisao I, Kiyoshi S, Eisuke I, Kazuhiko S., *Energy level alignment and*

- Interfacial electronic structures at organic/metal and organic/organic interfaces*, *Advanced Materials*, 1999, **11(8)**: p.605-25.
- [34] Forrest S.R, Burrows P.E, *Growth modes of organic semiconductor thin films using organic molecular beam deposition: epitaxy, van der Waals epitaxy, and quasi-epitaxy*, *Supramolecular Science*, 1997, **4(1-2)**: p.127-39.
- [35] Xu B, Tao C, Williams E.D, Reutt-Robey J.E, *Coverage dependent supramolecular structures: C₆₀:ACA monolayers on Ag(111)*, *Journal of the American Chemistry Society*, 2006, **128(26)**: p.8493-9.
- [36] Binnig G, Rohrer H, Gerber C, Weibel E, *Surface studies by scanning tunneling microscopy*, *Physical Review Letters*, 1982, **49(1)**: p.57.
- [37] Kuk Y, Silverman P. J, *Scanning tunneling microscope instrumentation*, *Review of Scientific Instruments*, 1989, **60(2)**: p.165-80.
- [38] Bardeen J, *Tunneling from a many-particle point of view*, *Physical Review Letters*, 1961, **6(2)**: p.57.
- [39] Chen C.J, *Introduction to scanning tunneling microscopy*, Oxford University Press, 1993.
- [40] Giaever I. *Energy gap in superconductors measured by electron tunneling*, *Physical Review Letters*, 1960, **5(4)**: p.147.
- [41] Tersoff J, Hamann D.R, *Theory of the scanning tunneling microscope*, *Physical Review B*, 1985, **31(2)**: p.805.
- [42] Bai C. *Scanning tunneling microscopy and its application*: Springer-Verlag, Berlin, 1995.
- [43] Alvarado S.F, Seidler P.F, Lidzey D.G, Bradley D.D.C. *Direct determination of the exciton binding energy of conjugated polymers using a scanning tunneling microscope*, *Physical Review Letters*, 1998,**81(5)**: p.1082.
- [44] Binnig G, Frank KH, Fuchs H, Garcia N, Reihl B, Rohrer H, *Tunneling spectroscopy and inverse photoemission: image and field States*, *Physical Review Letters*, 1985, **55(9)**: p.991.
- [45] Dougherty DB, Maksymovych P, Lee J, Yates Jr.J.T, *Local spectroscopy of image-potential-derived states: from single molecules to monolayers of benzene on Cu(111)*,*Physical Review Letters*, 2006, **97(23)**: p.236806-4.
- [46] M.A.Van Hove WHW, C.M.Chan, *Low energy electron diffraction (experiment, theory, and surface structure determination)*, Springer-Verlag, 1986.
- [47] Forrest S.R, Burrows P.E, Haskal E.I, *Ultrahigh-vacuum quasiepitaxial growth of model van der Waals thin films. II. Experiment*, *Physical Review B*, 1994, **49(16)**:p. 11309.
- [48] Masaaki Hara HS, Akira Yamada, Anthony F.Garito, *Epitaxial growth of organic thin films by organic molecular beam epitaxy*, *Japanese Journal of Applied Physics* 1989, **28**: p.L306-L308.
- [49] Koma A, *Molecular beam epitaxial growth of organic thin films*,*Progress in Crystal Growth and Characterization of Materials*, 1995,**30(2-3)**: p.129-52.
- [50] Herman MA, Sitter,H. *Molecular beam epitaxy*, Springer-Verlag: Berlin, 1988.

- [51] Baski A.A, Fuchs H. *Epitaxial growth of silver on mica as studied by AFM and STM*, Surface Science, 1994, **313(3)**: p.275-88.
- [52] Allan JM, *The art and science and other aspects of making sharp tips*, The Journal of Vacuum Science and Technology B, 1991, **9(2)**: p. 601-8.
- [53] Nierengarten JF, Gu T, Aernouts T, Geens W, Poortmans J, Hadziioannou G., *Fullerene–oligophenyleneethynylene conjugates: relationships between charge-carrier mobility, photovoltaic characteristics and chemical structure*, Applied Physics A: Materials Science & Processing, 2004, **79(1)**: p.47-9.
- [54] Peumans P, Yakimov A, Forrest S.R. *Small molecular weight organic thin-film photodetectors and solar cells*, Journal of Applied Physics, 2003, **93(7)**: p.3693-723.
- [55] Yoo S, Potscavage Jr WJ, Domercq B, Han S-H, Li T-D, Jones S.C, *Analysis of improved photovoltaic properties of pentacene/C₆₀ organic solar cells: Effects of exciton blocking layer thickness and thermal annealing*, Solid-State Electronics, 2007, **51(10)**: p.1367-75.
- [56] Osikowicz W, Jong MPd, Salaneck WR. *Formation of the interfacial dipole at organic-organic interfaces: C₆₀/polymer interfaces*, Advanced Materials, 2007, **19(23)**: p. 4213-7.
- [57] Brousse B, Ratier B, Moliton A, *Vapor deposited solar cells based on CuPc-C₆₀ single heterojunction: optimization of the deposition process*, Synthetic Metals, 2004, **147(1-3)**: p.293-8.
- [58] Brousse B, Ratier B, Moliton A, *Vapor deposited solar cells based on heterojunction or interpenetrating networks of zinc phthalocyanine and C₆₀* Thin Solid Films, 2004, **451-452**: p.81-5.
- [59] Geens W, Poortmans J, Jain S.C, Nijs J, Mertens R, Veenstra S.C, *Analytical study of PPV-oligomer- and C₆₀-based devices for optimizing organic solar cells*. Solar Energy Materials and Solar Cells, 2000, **61(1)**: p.43-51.
- [60] M.S.Dresselhaus GD, P.C.Ecklund. *Science of fullerenes and carbon nanotubes*. Academic Press, San Diego, 1996.
- [61] H. W. Kroto JRH, S. C. O'Brien, R. F. Curl and R. E. Smalley, *C₆₀: Buckminsterfullerene*, Nature, 1985, **318**: p.162-3.
- [62] Gimzewski J.K, Modesti S, David T, Schlittler R.R, *Scanning tunneling microscopy of ordered C₆₀ and C₇₀ layers on Au(111), Cu(111), Ag(110), and Au(110) surfaces*, The Journal of Vacuum Science and Technology B, 1994, **12(3)**: p. 1942-6.
- [63] Heiney P.A, Fischer J.E, McGhie A.R, Romanow W.J, Denenstien A.M, McCauley Jr J.P, *Orientational ordering transition in solid C₆₀*, Physical Review Letters, 1991, **66(22)**: p2911.
- [64] Fartash A, *Orientational epitaxy of high-quality C₆₀ films on Ag(111)*, Physical Review B, 1995, **52(11)**: p.7883.
- [65] Altman E.I, Colton R.J, *The interaction of C₆₀ with noble metal surfaces*, Surface Science, 1993, **295(1-2)**: p.13-33.
- [66] Altman E.I, Colton R.J, *Determination of the orientation of C₆₀ adsorbed on Au(111) and Ag(111)*, Physical Review B, 1993, **48(24)**: p.18244.

- [67] Sakurai T, Wang X.D, Hashizume T, Yurov V, Shinohara H, Pickering H.W. *Adsorption of fullerenes on Cu(111) and Ag(111) surfaces*, Applied Surface Science, 1995, **87-88**: p.405-13.
- [68] Lin-Lin W, Hai-Ping C, *Density functional study of the adsorption of a C₆₀ monolayer on Ag(111) and Au(111) surfaces*, Physical Review B, 2004, **69(16)**: p.165417.
- [69] T.Hashizume TS, *Fullerenes adsorption on Cu(111) and Ag(111) surfaces*, Surface Review and Letters, 1996, **3(1)**: p.905-13.
- [70] Tamai A, Seitsonen A.P, Fasel R, Shen Z.X, Osterwalder J, Greber T, *Doping-induced reorientation of C₆₀ molecules on Ag(111)*, Physical Review B, 2005, **72(8)**: p.085421.
- [71] Pedio M, Hevesi K, Zema N, Capozzi M, Perfetti P, Gouttebaron R, *C₆₀/metal surfaces: adsorption and decomposition*, Surface Science, 1999, **437(1-2)**: p.249-60.
- [72] Campbell R.B, Robertson J.M, Trotter J, *The crystal structure of hexacene, and a revision of the crystallographic data for tetracene*, Acta Crystallographica, 1962, **15(3)**: p.289-90.
- [73] Campbell R.B, Robertson J.M, Trotter J. *The crystal and molecular structure of pentacene*. Acta Crystallographica, 1961, **14(7)**: p.705-11.
- [74] Ruiz R, Nickel B, Koch N, Feldman L.C, Haglund R.F, Kahn A, *Pentacene ultrathin film formation on reduced and oxidized Si surfaces*, Physical Review B, 2003, **67(12)**: p.125406.
- [75] Meyer zu Heringdorf F-J, Reuter M.C, Tromp R.M. *Growth dynamics of pentacene thin films*, Nature, 2001, **412(6846)**: p.517-20.
- [76] Mayer A.C, Ruiz R, Headrick R.L, Kazimirov A, Malliaras G.G. *Early stages of pentacene film growth on silicon oxide*, Organic Electronics, 2004, **5(5)**: p.257-63.
- [77] Bouchoms IPM, Schoonveld W.A, Vrijmoeth J, Klapwijk T. M, *Morphology identification of the thin film phases of vacuum evaporated pentacene on SiO₂ substrates*, Synthetic Metals, 1999, **104(3)**: p.175-8.
- [78] Dimitrakopoulos C.D, Brown A.R, Pomp A, *Molecular beam deposited thin films of pentacene for organic field effect transistor applications*, Journal of Applied Physics, 1996, **80(4)**: p.2501-8.
- [79] Ruiz R, Nickel B, Koch N, Feldman L.C, Haglund R.F, Kahn A, *Dynamic scaling, island size distribution, and morphology in the aggregation regime of submonolayer pentacene films*, Physical Review Letters, 2003, **91(13)**: p.136102.
- [80] Conrad B.R, Cullen W.G, Riddick B.C, Williams E.D. *Pentacene islands grown on ultra-thin SiO₂*, Surface Science, 2009, **603(3)**: p.L27-L30.
- [81] Takashi M, Hideaki I, Masaru O, Kentaro S. *Structural studies on highly ordered and highly conductive thin films of pentacene*, Journal of Applied Physics, 1992, **72(11)**: p.5220-5.
- [82] Lukas S, Witte G, Woll C, *Novel mechanism for molecular self-assembly on metal substrates: unidirectional rows of pentacene on Cu(110) produced by a*

- substrate-mediated repulsion*, Physical Review Letters, 2001, **88(2)**: p.028301.
- [83] Sohnchen S, Lukas S, Witte G, *Epitaxial growth of pentacene films on Cu(110)*, Journal of Chemical Physics, 2004, **121(1)**: p.525-34.
- [84] Chen Q, McDowall A.J, Richardson N.V, *Ordered structures of tetracene and pentacene on Cu(110) surfaces*, Langmuir, 2003, **19(24)**: p. 10164-71.
- [85] Baldacchini C, Mariani C, Betti M.G. *Adsorption of pentacene on filled d-band metal surfaces: Long-range ordering and adsorption energy*, Journal of Chemical Physics, 2006, **124(15)**: p.7.
- [86] Menozzi C, Corradini V, Cavallini M, Biscarini F, Betti M. G, Mariani C, *Pentacene self-aggregation at the Au(110)-(1x2) surface: growth morphology and interface electronic states*, Thin Solid Films, 2003, **428(1-2)**: p.227-31.
- [87] Ph G, Carty D, Hughes G, McDonald O, Cafolla A. A, *Long-range order in a multilayer organic film templated by a molecular-induced surface reconstruction: Pentacene on Au(110)*, Applied Physics Letters, 2004, **85(14)**: p.2777-9.
- [88] Wang Y.L, Ji W, Shi D.X, Du S.X, Seidel C, Ma Y.G. *Structural evolution of pentacene on a Ag(110) surface*, Physical Review B, 2004, **69(7)**: p.075408.
- [89] Eremtchenko M, Temirov R, Bauer D, Schaefer J.A, Tautz F.S, *Formation of molecular order on a disordered interface layer: pentacene/Ag(111)*, Physical Review B, 2005, **72(11)**: p.115430.
- [90] Danisman M.F, Casalis L, Scoles G, *Supersonic molecular beam deposition of pentacene thin films on two Ag(111) surfaces with different step densities*, Physical Review B, 2005, **72(8)**: p.085404.
- [91] Kafer D, Witte G, *Evolution of pentacene films on Ag(1 1 1): Growth beyond the first monolayer*, Chemical Physics Letters, 2007, **442(4-6)**: p.376-83.
- [92] Zhang H.L, Chen W, Huang H, Chen L, Wee A.T.S, *Preferential trapping of C₆₀ in nanomesh voids*, Journal of the American Chemical Society, 2008, **130(9)**: p.2720-1
- [93] Joo H.K, Zhu X.Y. *π -stacked pentacene thin films grown on Au(111)*, Applied Physics Letters, 2003, **82(19)**: p.3248-50.
- [94] France C.B, Schroeder P.G, Parkinson B.A. *Direct observation of a widely spaced periodic row structure at the pentacene/Au(111) interface using scanning tunneling microscopy*. Nano Letters, 2002, **2(7)**: p.693-6.
- [95] France C. B, Schroeder P.G, Forsythe J.C, Parkinson B.A, *Scanning tunneling microscopy study of the coverage-dependent structures of pentacene on Au(111)*, Langmuir, 2003, **19(4)**: p.1274-81.
- [96] Xu B, Tao C, Cullen W.G, Reutt-Robey J.E, Williams E.D. *Chiral symmetry breaking in two-dimensional C₆₀-ACA intermixed system*, Nano Letters, 2005, **5(11)**, p.2207-11.
- [97] Frederick B.G, Chen Q, Leibsle F.M, Dhesi S.S, Richardson N.V, *Electron-stimulated disordering in c(8x2) benzoate/Cu(110): a combined STM, LEED and HREELS study*, Surface Science, 1997, **394(1-3)**: p.26-46.
- [98] Lee K, Yu J, *Ab initio study of pentacene on Au(011) surface*, Surface Science.

- 2005, **589(1-3)**: p.8-18.
- [99] Schroeder P.G, France C.B, Park J.B, Parkinson B.A. *Energy level alignment and two-dimensional structure of pentacene on Au(111) surfaces*, Journal of Applied Physics, 2002, **91(5)**: p.3010-4.
- [100] Daniel K, Lars R, Gregor W. *Growth of pentacene on clean and modified gold surfaces*. Physical Review B, 2007, **75(8)**: p.085309.
- [101] Lang N.D, Kohn W. *Theory of metal surfaces: charge density and surface energy*. Physical Review B, 1970, **1(12)**: p.4555.
- [102] Hyldgaard P, Persson M, *Long-ranged adsorbate-adsorbate interactions mediated by a surface-state band*, Journal of Physics: Condensed Matter, 2000, **12(1)**: p.L13-L9.
- [103] Lackinger M, Griessl S, Heckl WM, Hietschold M, *Coronene on Ag(111) investigated by LEED and STM in UHV*, The Journal of Physical Chemistry B, 2002, **106(17)**: p.4482-5.
- [104] Levi A.C, Calvini P, *Elastic theory of surface deformation in C₆₀ adsorption*. Surface Science, 2007, **601(6)**: p.1494-500.
- [105] Ming X, Michael X.Y, Sam K.J, Brian E.B, Paul S, *Benzene adsorption on Cu(111): Formation of a stable bilayer*, The Journal of Chemical Physics, 1994, **101(10)**: p.9122-31.
- [106] Lee J, Dougherty D.B, Yates J.T. *Edge-on bonding of benzene molecules in the second adsorbed layer on Cu(110)*, The Journal of Physical Chemistry B, 2006, **110(32)**: p.15645-9.
- [107] Beernink G, Strunskus T, Witte G, Ch W, *Importance of dewetting in organic molecular-beam deposition: Pentacene on gold*, Applied Physics Letters, 2004, **85(3)**: p.398-400.
- [108] Guaino P, Carty D, Hughes G, Moriarty P, Cafolla A.A, *Scanning tunneling microscopy study of pentacene adsorption on Ag/Si(1 1 1)-(√3×√3)R30°*, Applied Surface Science, 2003, **212-213**: p537-41.
- [109] Teng J, Guo J, Wu K, Wang E, *Temperature and coverage driven condensation of pentacene on the Si(111)-(√3×√3)R30°Ag surface*, Journal of Physics: Condensed Matter, 2007, **19(35)**: p.356005.
- [110] Zhenan B, Andrew J.L, Ananth D, *Organic field-effect transistors with high mobility based on copper phthalocyanine*, Applied Physics Letters, 1996, **69(20)**: p.3066-8.
- [111] Jan Hendrik S, Zhenan B, *Influence of disorder on the electron transport properties in fluorinated copper-phthalocyanine thin films*, Journal of Applied Physics, 2001, **89(6)**: p.3526-8.
- [112] Guntter S, Abdol Khezer S, Wolfgang S, Holger K, Dieter W, *Photo-oxidative stability and its correlation with semi-empirical MO calculations of various Tetraazaporphyrin derivatives in solution*, Journal of Porphyrins and Phthalocyanines, 1997, **1(2)**: p.159-67.
- [113] Meng-Sheng L, Steve S, *Electronic structure and bonding in metal phthalocyanines, Metal=Fe, Co, Ni, Cu, Zn, Mg*, The Journal of Chemical Physics, 2001, **114(22)**: p.9780-91.

- [114]E.A.Silinsh VC, *Organic Molecular Crystals*. AIP Press, New York. 1994.
- [115]Buchholz J.C, Somorjai G.A, *The surface structures of phthalocyanine monolayers and vapor-grown films: A low-energy electron diffraction study*, The Journal of Chemical Physics, 1977, **66(2)**:p.573-80.
- [116]C.J.Brown, *Crystal Structure of β -copper phthalocyanine*, Journal of the Chemical Society A, 1968, p.2488-93.
- [117]Sharp J.H, Miller R.L, *Kinetics of the thermal $\alpha \rightarrow \beta$ polymorphic conversion in metal-free phthalocyanine*, The Journal of Physical Chemistry, 1968, **72(9)**: p.3335-7.
- [118]C.C.Leznoff, *Phthalocyanines: Properties and Applications*. VCH Publishers Inc., 1989.
- [119]Hajime H, Anthony J.D, Yusei M, *The structure and properties of phthalocyanine films grown by the molecular beam epitaxy technique. III. Preparation and characterization of lutetium diphthalocyanine films*, Journal of Applied Physics, 1990, **67(11)**: p.6871-5.
- [120]Hajime H, Shaoli F, Yusei M, *Epitaxial growth of lead phthalocyanine film on KI crystal*, Journal of Applied Physics, 1993, **73(6)**: p.3111-3.
- [121]Peisert H, Schwieger T, Auerhammer J.M, Knupfer M, Golden M.S, Fink J, *Order on disorder: Copper phthalocyanine thin films on technical substrates*, Journal of Applied Physics, 2001, **90(1)**: p.466-9.
- [122]Ludwig C, Strohmaier R, Petersen J, Gompf B, Eisenmenger W, *Epitaxy and scanning tunneling microscopy image contrast of copper--phthalocyanine on graphite and MoS₂*, The Journal of Vacuum Science and Technology B, 1994, **12(3)**: p. 1963-6.
- [123]Chizhov I, Scoles G, Kahn A, *The influence of steps on the orientation of copper phthalocyanine monolayers on Au(111)*, Langmuir, 2000, **16(9)**: p.4358.
- [124]Lu X, Hipps K.W, *Scanning tunneling microscopy of metal phthalocyanines: d^6 and d^8 cases*, The Journal of Physical Chemistry B. 1997, **101(27)**: p.5391.
- [125]Lu X, Hipps K.W, Wang X.D, Mazur U, *Scanning tunneling microscopy of metal phthalocyanines: d^7 and d^9 cases*, Journal of the American Chemical Society, 1996, **118(30)**: p.7197.
- [126]Takada M, Tada H, *Low temperature scanning tunneling microscopy of phthalocyanine multilayers on Au(100) surfaces*, Chemical Physics Letters, 2004, **392(1-3)**: p.265-9.
- [127]Cheng Z. H, Gao L, Deng Z. T, Liu Q, Jiang N, Lin X, *Epitaxial growth of iron phthalocyanine at the initial stage on Au(111) Surface*, The Journal of Physical Chemistry C, 2007, **111(6)**: p.2656-60.
- [128]Park K.T, Miller A, Klier K, Opila R.L, Rowe J.E, *Heteroepitaxial copper phthalocyanine on Au(011) studied by high-resolution X-ray photoelectron spectroscopy*, Surface Science, 2003, **529(3)**: p.L285-L92.
- [129]Trinity S.E, Kenneth T.P, Steven L.H, Mark D.U, Jack E.R, *Influence of substrate temperature on epitaxial copper phthalocyanines studied by photoemission spectroscopy*, Journal of Applied Physics, 2004, **95(3)**:

p.982-8.

- [130]Trinity S.E, Kenneth T.P, Marc D.U, Steven L.H, Jack E.R, *Interaction of metallophthalocyanines(MPc,M= Co, Ni) on Au(001): Ultraviolet photoemission spectroscopy and low energy electron diffraction study*, Journal of Applied Physics, 2006, **100(9)**: p.093515.
- [131]Amsalem P, Giovanelli L, Themlin J.M, Koudia M, Abel M, Oison V, *Interface formation and growth of a thin film of ZnPcCl₈/Ag(1 1 1) studied by photoelectron spectroscopy*, Surface Science, 2007, **601(18)**:4185-8.
- [132]Koudia M, Abel M, Maurel C, Bliiek A, Catalin D, Mossoyan M, *Influence of chlorine substitution on the self-assembly of zinc phthalocyanine*, The Journal of Physical Chemistry B, 2006, **110(20)**: p.10058-62.
- [133]Manandhar K, Park K.T, Ma S, Hrbek J, *Heteroepitaxial thin film of iron phthalocyanine on Ag(111)*, Surface Science, 2009, **603(4)**: p.636-40.
- [134]Manandhar K, Ellis T, Park K.T, Cai T, Song Z, Hrbek J, *A scanning tunneling microscopy study on the effect of post-deposition annealing of copper phthalocyanine thin films*, Surface Science, 2007,**601(17)**: p.3623-31.
- [135]Koudia M, Abel M, Maurel C, Bliiek A, Catalin D, Mossoyan M, *Influence of chlorine substitution on the self-assembly of zinc phthalocyanine*, The Journal of Physical Chemistry B, 2006, **110(20)**: p.10058-62.
- [136]Nakamura M, Tokumoto H, *Molecular arrangement of copper phthalocyanine on Si(001)-(2x1)-H:a high-resolution frictional force microscopy and molecular mechanics study*, Surface Science,1998, **398(1-2)**:p.143-53.
- [137]Huang H, Chen W, Wee A.T.S, *Low-temperature scanning tunneling microscopy investigation of epitaxial growth of F₁₆CuPc Thin Films on Ag(111)*, The Journal of Physical Chemistry C, 2008, **112(38)**: p.14913-8.
- [138]Wakayama Y, *Assembly process and epitaxy of the F₁₆CuPc monolayer on Cu(111)*, The Journal of Physical Chemistry C, 2007, **111(6)**: p.2675-8.
- [139]Barlow D, Scudiero L, Hipps K. W, *Scanning tunneling microscopy of 1, 2, and 3 layers of electroactive compounds*, Ultramicroscopy, 2003, **97(1-4)**:p.47-53.
- [140]Huang Y, Chen W, Chen S, Wee A, *Low-temperature scanning tunneling microscopy and near-edge X-ray absorption fine structure investigation of epitaxial growth of F₁₆CuPc thin films on graphite*, Applied Physics A: Materials Science & Processing, 2009, **95(1)**: p.107-11.
- [141]Forrest S.R, *The path to ubiquitous and low-cost organic electronic appliances on plastic*, Nature, 2004, **428(6986)**: p.911-8.
- [142]M.Schwoerer. *Organic molecular solids*, Wiley,Weinheim, 2007.
- [143]Esther B, Dimas GdO, Stefan S, Helmut D, Osso JO, Bernd S. *In situ study of the growth of nanodots in organic heteroepitaxy*, Physical Review Letters, 2006, **97(7)**: p.076102.
- [144]Dougherty D.B, Maksymovych P, Lee J, J. T. Yates, Jr. *Local spectroscopy of image-potential-derived states: from single molecules to monolayers of benzene on Cu(111)*, Physical Review Letters, 2006, **97(23)**: p.236806.

- [145]Joo HK, Demetrio da Silva F, Jean-Luc B, Zhu X.Y, *Shallow trap states in pentacene thin films from molecular sliding*, Applied Physics Letters, 2005, **86(15)**: p.152115.
- [146]Thayer GE, Sadowski JT, Meyer zu Heringdorf F, Sakurai T, Tromp RM, *Role of surface electronic structure in thin film molecular ordering*, Physical Review Letters, 2005, **95(25)**: p.256106.
- [147]Fukagawa H, Yamane H, Kataoka T, Kera S, Nakamura M, Kudo K, *Origin of the highest occupied band position in pentacene films from ultraviolet photoelectron spectroscopy: Hole stabilization versus band dispersion*, Physical Review B, 2006, **73(24)**: p.245310.
- [148]Fritz S.E, Martin S.M, Frisbie C.D, Ward M.D, Toney M.F, *Structural characterization of a pentacene monolayer on an amorphous SiO₂ substrate with grazing incidence X-ray diffraction*, Journal of the American Chemical Society. 2004, **126(13)**: p.4084-5.
- [149]Wei-Shan H, Yu-Tai T, Yen-Fu C, Chia-Seng C, *Orientation-dependent conductance study of pentacene nanocrystals by conductive atomic force microscopy*, Applied Physics Letters, 2008, **93(5)**: p.053304.
- [150]Changgan Z, Bin L, Bing W, Haiqian W, Kedong W, Jinlong Y, *What can a scanning tunneling microscope image do for the insulating alkanethiol molecules on Au(111) substrates?* The Journal of Chemical Physics, 2002, **117(2)**:p.851-6.
- [151]Cantrell R, Clancy P, *A computational study of surface diffusion of C₆₀ on pentacene*, Surface Science, 2008, **602(22)**: p.3499-505.
- [152]Alerhand O.L, Vanderbilt D, Meade R.D, Joannopoulos J.D, *Spontaneous formation of stress domains on crystal surfaces*, Physical Review Letters, 1988, **61(17)**: p.1973.
- [153]van Gastel R, Bartelt N.C, Feibelman P.J, Leonard F, Kellogg G.L, *Relationship between domain-boundary free energy and the temperature dependence of stress-domain patterns of Pb on Cu(111)*, Physical Review B, 2004, **70(24)**: p.245413.
- [154]Kern K, Niehus H, Schatz A, Zeppenfeld P, Goerge J, Comsa G, *Long-range spatial self-organization in the adsorbate-induced restructuring of surfaces: Cu{100}-(2x1)O*, Physical Review Letters, 1991, **67(7)**: p.855.
- [155]Yang WL, Brouet V, Zhou XJ, Choi HJ, Louie SG, Cohen ML, *Band structure and fermi surface of electron-doped C₆₀ monolayer*, Science, 2003, **300(5617)**: p.303-7.
- [156]Gregory D, Jingzhi P, Donald GT, Zhu X.Y. *Lateral confinement of image electron wave function by an interfacial dipole lattice*, The Journal of Chemical Physics, 2003, **118(10)**: p.4337-40.
- [157]Ng K-O, Vanderbilt D, *Stability of periodic domain structures in a two-dimensional dipolar model*, Physical Review B, 1995, **52(3)**: p.2177.
- [158]Rosei F, Schunack M, Jiang P, Gourdon A, Lagsgaard E, Stensgaard I, *Organic molecules acting as templates on metal surfaces*, Science, **296(5566)**: p.328-31.

- [159]Barth JV, Costantini G, Kern K, *Engineering atomic and molecular nanostructures at surfaces*, Nature, 2005, **437(7059)**: p.671-9.
- [160]Mena-Osteritz E, Bauerle P, *Complexation of C₆₀ on a cyclo thiophene monolayer template*, Advanced Materials, 2006, **18(4)**: p.447-51.
- [161]Andreas K, Davide B, Fuyong C, Meike S, Francois D, Thomas J, *Adsorption and dynamics of long-range interacting fullerenes in a flexible, two-dimensional, nanoporous porphyrin network*, ChemPhysChem, 2006, **7(7)**: p.1462-70.
- [162]Bonifazi D, Kiebele A, Stohr M, Cheng F, Jung T, Diederich F, *Supramolecular nanostructuring of silver surfaces via self-assembly of fullerene and porphyrin modules*, Advanced Functional Materials, 2007, **17(7)**: p.1051-62.
- [163]Nikolai W, Davide B, Fuyong C, Andreas K, Meike S, Thomas J, *A supramolecular multiposition rotary device*, Angewandte Chemie International Edition, 2007, **46(22)**: p.4089-92.
- [164]Xiao W, Ruffieux P, Ait-Mansour K, Groning O, Palotas K, Hofer W.A, *Formation of a regular fullerene nanochain lattice*, The Journal of Physical Chemistry B, 2006, **110(43)**: p.21394-8.
- [165]Neel N, Kroer J, Berndt R, *Highly periodic fullerene nanomesh*, Advanced Materials, 2006, **18(2)**: p.174-7.
- [166]Klitgaard S.K, Egeblad K, Haahr L.T, Hansen M.K, Hansen D, Svagin J, *Self-assembly of C₆₀ into highly ordered chain-like structures on HOPG observed at ambient conditions*, Surface Science, 2007, **601(9)**: p.L35-L8.
- [167]Feng M, Lee J, Zhao J, Yates, Petek H, *Nanoscale templating of close-packed C₆₀ nanowires*, Journal of the American Chemical Society, 2007, **129(41)**: p.12394-5.
- [168]Dougherty D.B, Jin W, Cullen W.G, Reutt-Robey J.E, Robey S.W, *Variable temperature scanning tunneling microscopy of pentacene monolayer and bilayer phases on Ag(111)*, The Journal of Physical Chemistry C, 2008, **112(51)**: p.20334-9.
- [169]Zhang H, Chen W, Chen L, Huang H, Wang X.S, Yuhara J, Wee A, *C₆₀ molecular chains on alpha-Sexithiophene nanostripes*, Small, 2007, **3(12)**: p.2015-8.
- [170]David WIF, Ibberson RM, Matthewman JC, Prassides K, Dennis TJS, Hare JP, *Crystal structure and bonding of ordered C₆₀*, Nature, 1991, **353(6340)**: p.147-9.
- [171]Lu J.P, Li X.P, Martin R.M, *Ground state and phase transitions in solid C₆₀*, Physical Review Letters, 1992, **68(10)**: p.1551.
- [172]Tsiper EV, Soos ZG, *Charge redistribution and polarization energy of organic molecular crystals*, Physical Review B, 2001, **64(19)**: p.195124.
- [173]Amy F, Chan C, Kahn A, *Polarization at the gold/pentacene interface*, Organic Electronics, 2005, **6(2)**: p.85-91.
- [174]Ohno T.R, Chen Y, Harvey S.E, Kroll G.H, Weaver J.H, Haufler R.E, *C₆₀ bonding and energy-level alignment on metal and semiconductor surfaces*.

- Physical Review B, 1991, **44(24)**: p.13747.
- [175]Perdigao LMA, Perkins E.W, Ma J, Staniec P.A, Rogers B.L, Champness N.R, *Bimolecular networks and supramolecular traps on Au(111)*, The Journal of Physical Chemistry B, 2006, **110(25)**: p.12539-42.
- [176]Eddaoudi M, Kim J, Rosi N, Vodak D, Wachter J, O'Keeffe M, *Systematic design of pore size and functionality in isoreticular MOFs and their application in methane storage*, Science, 2002, **295(5554)**: p.469-72.
- [177]Shuhei Furukawa, *Structural transformation of a two-dimensional molecular network in response to selective guest inclusion*. Angewandte Chemie International Edition, 2007, **46(16)**: p.2831-4.
- [178]Wong-Foy A.G, Matzger A.J, Yaghi O.M, *Exceptional H₂ saturation uptake in microporous metal-organic frameworks*, Journal of the American Chemistry Society, 2006, **128(11)**: p.3494-5.
- [179]Dinca M, Dailly A, Liu Y, Brown C.M, Neumann D.A, Long J.R. *Hydrogen storage in a microporous metal-organic framework with exposed Mn²⁺ coordination sites*, Journal of the American Chemistry Society, 2006, **128(51)**: p.16876-83.
- [180]Tait SL, Wang Y, Costantini G, Lin N, Baraldi A, Esch F, *Metal-organic coordination interactions in Fe-Terephthalic acid networks on Cu(100)*, Journal of the American Chemistry Society, 2008, **130(6)**: p.2108-13.
- [181]Sudik A. C, Cote A. P, Yaghi O. M. *Metal-organic frameworks based on trigonal prismatic building blocks and the new "acs" topology*, Inorganic Chemistry. 2005, **44(9)**: p.2998-3000.
- [182]Dietmar P, Comisso A, Dmitriev A, Strunskus T, Lin N, Woll C, *Ionic hydrogen bonds controlling two-dimensional supramolecular systems at a metal surface*, Chemistry-A European Journal, 2007, **13(14)**: p.3900-6.
- [183]Feyter S.D, Schryver F.C.D, *Two-dimensional supramolecular self-assembly probed by scanning tunneling microscopy*, Chemical Society Reviews, 2003, **32(3)**: p.139-50.
- [184]Wintjes N, Hornung J, Lobo-Checa J, Voigt T, Samuely T, Thilgen C, *Supramolecular synthons on surfaces: controlling dimensionality and periodicity of tetraarylporphyrin assemblies by the interplay of cyano and alkoxy substituents*, Chemistry - A European Journal, 2008, **14(19)**: p. 5794-802.
- [185]Yoshimoto S, Tsutsumi E, Narita R, Murata Y, Murata M, Fujiwara K, *Epitaxial supramolecular assembly of fullerenes formed by using a coronene template on a Au(111) surface in solution*, Journal of the American Chemistry Society, 2007, **129(14)**: p.4366-76.
- [186]Han H, Wei C, Lan C, Hong Liang Z, Xue Sen W, Shi Ning B, *"Zigzag" C₆₀ chain arrays*, Applied Physics Letters, 2008, **92(2)**: p.023105.
- [187]Luis M.A, Perdigao, Saywell A, Gisell F, *Functionalized supramolecular nanoporous arrays for surface templating*, Chemistry-A European Journal. 2008, **14(25)**: p. 7600-7.
- [188]Dougherty D.B, Jin W, Cullen W.G, Dutton G, Reutt-Robey J.E, Robey S.W.

- Local transport gap in C₆₀ nanochains on a pentacene template*, Physical Review B, 2008, **77(7)**: p.073414.
- [189]Echenique P.M, Berndt R, Chulkov E.V, Fauster T, Goldmann A, *Decay of electronic excitations at metal surfaces*, Surface Science Reports. 2004, **52(7-8)**: p.219-317.
- [190]Gaffney K.J, Wong C.M, Liu S.H, Miller A.D, McNeill J.D, Harris C.B, *Femtosecond electron dynamics at the benzene/Ag(111) interface*, Chemical Physics, 2000, **251(1-3)**: p.99-110.
- [191]Zhong Q, Gahl C, Wolf M. *Two-photon photoemission spectroscopy of pyridine adsorbed on Cu(1 1 1)*, Surface Science, 2002, **496(1-2)**: p.21-32.
- [192]Velic D, Hotzel A, Wolf M, Ertl G. *Electronic states of the C₆H₆/Cu(111) system: Energetics, femtosecond dynamics, and adsorption morphology*, The Journal of Chemical Physics, 1998, **109(20)**: p.9155-65.
- [193]Feng M, Zhao J, Petek H, *Atomlike, hollow-core-bound molecular orbitals of C₆₀*, Science, 2008, **320(5874)**: p.359-62.
- [194]Jost M.B, Troullier N, Poirier D.M, Martins J.L, Weaver J.H, Chibante L.P.F, *Band dispersion and empty electronic states in solid C₆₀: Inverse photoemission and theory*, Physical Review B, 1991, **44(4)**: p.1966.
- [195]Lindstrom C.D, Muntwiler M, Zhu X.Y. *Electron dynamics at polyacene/Au(111) interfaces*, The Journal of Physical Chemistry B, 2007, **111(24)**: p.6913-20.
- [196]Kash P.W, Yang M.X, Teplyakov A.V, Flynn G.W, Bent B.E, *Chemical displacement of molecules adsorbed on copper surfaces: Low-temperature studies with applications to surface reactions*, The Journal of Physical Chemistry B. 1997, **101(40)**: p.7908-18.
- [197]Girifalco L.A. *Interaction potential for carbon (C₆₀) molecules*. The Journal of Physical Chemistry, 1991, **95(14)**: p.5370-1.
- [198]Xinghua L, Grobis M, Khoo K.H, Steven G.L, Crommie M.F, *Charge transfer and screening in individual C₆₀ molecules on metal substrates: A scanning tunneling spectroscopy and theoretical study*, Physical Review B, 2004, **70(11)**: p.115418.
- [199]Dimitrakopoulos C.D, Malenfant P, *Organic thin film transistors for large area electronics*, Advanced Materials, 2002, **14(2)**: p.99-117.
- [200]Coropceanu V, Cornil J, da Silva Filho D.A, Olivier Y, Silbey R, Bredas J-L, *Charge transport in organic semiconductors*, Chemical Reviews. 2007, **107(4)**: p.926-52.
- [201]Loi MA, da Como E, Dinelli F, Murgia M, Zamboni R, Biscarini F, *Supramolecular organization in ultra-thin films of α -sexithiophene on silicon dioxide*. Nature Material, 2005, **4(1)**: p.81-5.
- [202] de Oteyza D.G, Barrena E, Osso J.O, Sellner S, Dosch H. *Thickness-dependent structural transitions in fluorinated copper-phthalocyanine (F₁₆CuPc) Films*, Journal of the American Chemical Society, 2006, **128(47)**: p.15052-3.
- [203]Kowarik S, Gerlach A, Sellner S, Schreiber F, Cavalcanti L, Kononov O,

- Real-time observation of structural and orientational transitions during growth of organic thin films*, Physical Review Letters, 2006, **96(12)**: p.125504.
- [204] Timpanaro S, Sassella A, Borghesi A, Porzio W, Fontaine P, Goldmann M. *Crystal structure of epitaxial quaterthiophene thin films grown on potassium acid phthalate*, Advanced Materials, 2001, **13(2)**: p.127-30.
- [205] Oehzelt M, Koller G, Ivanco J, Berkebile S, Haber T, Resel R, *Organic heteroepitaxy: p-sexiphenyl on uniaxially oriented alpha-sexithiophene*, Advanced Materials, 2006, **18(18)**: p.2466-70.
- [206] Heath J.R, *Molecular Electronics*. Annual Review of Materials Research, 2009, **39(1)**: p.1-23.
- [207] Daniel BD, Wei J, William GC, Janice ER-R, Steven WR, *Striped domains at the pentacene:C₆₀ interface*, Applied Physics Letters, 2009, **94(2)**: p.023103.
- [208] Stadler C, Hansen S, Pollinger F, Kumpf C, Umbach E, Lee T.L, *Structural investigation of the adsorption of SnPc on Ag(111) using normal-incidence x-ray standing waves*, Physical Review B, 2006, **74(3)**: p.035404.
- [209] Kilian L, Umbach E, Sokolowski M. *Molecular beam epitaxy of organic films investigated by high resolution low energy electron diffraction (SPA-LEED): 3,4,9,10-perylenetetracarboxylicacid-dianhydride (PTCDA) on Ag(100)*, Surface Science, 2004, **573(3)**: p.359-78.
- [210] Karl F. Schoch, Jr., James Gregg, Jr., Thomas A.T, *Morphology of metal phthalocyanine thin films*, Journal of Vacuum Science & Technology A, 1988, **6(1)**: p.155-8.
- [211] Dogo S, Germain J.P, Maleysson C, Pauly A, *Interaction of NO₂ with copper phthalocyanine thin films I: Characterization of the copper phthalocyanine films*, Thin Solid Films, 1992, **219(1-2)**: p.244-50.
- [212] Yamashita A, Maruno T, Hayashi T, *Absorption spectra of organic molecular beam deposited vanadyl- and titanylphthalocyanine*, The Journal of Physical Chemistry, 2002, **97(18)**: p.4567-9.
- [213] Kataoka T, Fukagawa H, Hosoumi S, Nebashi K, Sakamoto K, Ueno N, *Observation of a temperature-dependent transition of a copper-phthalocyanine thin film adsorbed on HOPG*, Chemical Physics Letters, 2008, **451(1-3)**:p.43-7.
- [214] Han H, Wei C, Shi C, Dong Chen Q, Xing Yu G, Andrew Thye Shen W. *Molecular orientation of CuPc thin films on C₆₀/Ag(111)*, Applied Physics Letters, 2009, **94(16)**: p.163304.
- [215] Kobayashi T, Fujiyoshi Y, Iwatsu F, Uyeda N, *High-resolution TEM images of zinc phthalocyanine polymorphs in thin films*, Acta Crystallographica, 1981, **37(5)**: p.692-7.
- [216] Senthilarasu S, Hahn YB, Soo-Hyoung L, *Structural analysis of zinc phthalocyanine (ZnPc) thin films: X-ray diffraction study*, Journal of Applied Physics, 2007, **102(4)**: p.043512.
- [217] Oss JO, Schreiber F, Kruppa V, Dosch H, Garriga M, Alonso MI, *Controlled*

- molecular alignment in phthalocyanine thin films on stepped sapphire surfaces*. *Advanced Functional Materials*, 2002, **12(6-7)**: p.455-60.
- [218]Barrena E, Osso J.O, Schreiber F, Garriga M, Alonso M.I, Dosch H, *Self organization of phthalocyanines on Al₂O₃ (112-0) in aligned and ordered films*, *Journal of Materials Research*, 2004, **19(7)**: p.2061-71.
- [219]Dimas G.d.O, Esther B, Osso J.O, Helmut D, Stephan M, Jens P. *Controlled enhancement of the electron field-effect mobility of F₁₆CuPc thin-film transistors by use of functionalized SiO₂ substrates*, *Applied Physics Letters*, 2005, **87(18)**:p.183504.
- [220]Berkebile S, Koller G, Hlawacek G, Teichert C, Netzer F.P, Ramsey M.G, *Diffusion versus sticking anisotropy: Anisotropic growth of organic molecular films*, *Surface Science*, 2006, **600(24)**: p.L313-L7.
- [221]Gardener J, Owen J.H.G, Miki K, Heutz S, *A scanning tunnelling microscopy investigation into the initial stages of copper phthalocyanine growth on passivated silicon surfaces*, *Surface Science*, 2008; **602(4)**: p.843-51.
- [222]Frenkel Y.K.T, *On the theory of plastic deformation and twinning*. *Zh.Eksp.Teor.Fiz*, 1938, **8**: p.1340.
- [223]Cyganik P, Buck M, Wilton-Ely, Woll C, *Stress in self-assembled monolayers: w-biphenyl alkane thiols on Au(111)*, *The Journal of Physical Chemistry B*, 2005, **109(21)**: p.10902-8.
- [224]Zhang Y, Gao X, Weaver M.J, *Scanning tunneling microscopy of C₆₀ and C₇₀ on ordered Au(111) and Au(110): molecular structure and electron transmission*, *Journal of physical Chemistry*, 1992, **96(22)**: p.510-3.
- [225]Wragg J.L.C, J.E.; White, H.W.; Kratschmer, W.; Huffman, D.R, *Scanning tunneling microscopy of solid C₆₀/ C₇₀*, *Nature*, 1990, **348(6302)**: p.623-4.
- [226]Li Y.Z, Patrin J.C, Chander M, Weaver J.H, Chibante L.P.F, Smalley R.E. *Ordered overlayers of C₆₀ on GaAs(110) studied with scanning tunneling microscopy*, *Science*, 1991, **252(5005)**: p.547-8.
- [227]Wang H, Zeng C, Wang B, Hou J.G, Li Q, Yang J, *Orientational configurations of the C₆₀ molecules in the (2x2) superlattice on a solid C₆₀ (111) surface at low temperature*, *Physical Review B*, 2001, **63(8)**: p.085417.
- [228]Grobis M, Lu X, Crommie M.F, *Local electronic properties of a molecular monolayer: C₆₀ on Ag(001)*, *Physical Review B*, 2002, **66(16)**: p.161408.
- [229]Mohwald H, *Direct characterization of monolayers at the air-water interface*, *Thin Solid Films*, 1988, **159(1-2)**: p.1-15.
- [230]Seul M, Wolfe R, *Evolution of disorder in magnetic stripe domains I. Transverse instabilities and disclination unbinding in lamellar patterns*, *Physical Review A*, 1992, **46(12)**: p.7519.
- [231]Kern K, Niehus H, Schatz A, Zeppenfeld P, Goerge J, Comsa G, *Long-range spatial self-organization in the adsorbate-induced restructuring of surfaces: Cu{100}-(2 x 1)O*, *Physical Review Letters*, 1991, **67(7)**: p.855.
- [232]Kern K, Niehus H, Schatz A, Zeppenfeld P, Goerge J, Comsa G, *Long-range spatial self-organization in the adsorbate-induced restructuring of surfaces: Cu{100}-(2x1)O*, *Physical Review Letters*, 1991, **67(7)**: p.855.

- [233]Girifalco L.A, *Molecular properties of C₆₀ in the gas and solid phases*, Journal of Physical Chemistry, 1992, **96(2)**: p.858-61
- [234]Weis J.J, Levesque D, *Ferroelectric phases of dipolar hard spheres*, Physical Review E, 1993, **48(5)**: p.3728.
- [235]Weis J.J, Levesque D, *Chain formation in low density dipolar hard spheres: A Monte Carlo study*, Physical Review Letters,1993, **71(17)**: p.2729.
- [236]Hill IG, Milliron D, Schwartz J, Kahn A, *Organic semiconductor interfaces: electronic structure and transport properties*, Applied Surface Science, 2000, **166(1-4)**: p.354-62.
- [237]Igor A, Victor G, *Quantum-chemical characterization of the origin of dipole formation at molecular organic/organic interfaces*, Advanced Functional Materials, 2009, **19(4)**: p.624-33.
- [238]Mulliken R.S, Person W.B, *Molecular compounds and their spectra*, Journal of the American Chemical Society, 2002, **91(13)**: p.3409-13.
- [239]Dewar M.J.S, Thompson C.C, *π -molecular complexes--III: A critique for charge-transfer, and stability constants for some TCNE-hydrocarbon complexes*, Tetrahedron, 1966, **22(7)**: p.97-114.
- [240]Morokuma K, *Why do molecules interact? The origin of electron donor-acceptor complexes, hydrogen bonding and proton affinity*, Accounts of Chemical Research, 2002, **10(8)**: p.294-300.
- [241]Bagus PS, Staemmler V, Woll C, *Exchangelike effects for closed-shell adsorbates: interface dipole and work function*, Physical Review Letters, 2002, **89(9)**: p.096104.
- [242]Gregor W, Simon L, Paul SB, Christof W. *Vacuum level alignment at organic/metal junctions: ``Cushion" effect and the interface dipole*, Applied Physics Letters, 2005, **87(26)**: p.263502.
- [243]Arkhipov V.I, Emelianova E.V, Tak Y.H, Bassler H, *Charge injection into light-emitting diodes: Theory and experiment*, Journal of Applied Physics, 1998, **84(2)**: p.848-56.
- [244]Gerlach A, Schreiber F, Sellner S, Dosch H, Vartanyants I.A, Cowie B.C.C, *Adsorption-induced distortion of F₁₆CuPc on Cu(111) and Ag(111): An x-ray standing wave study*, Physical Review B, 2005;**71(20)**: p.205425.
- [245]Lozzi L, Granato V, Picozzi S, Simeoni M, Rosa S.L, Delly B, *CuPc:C₆₀ blend film: A photoemission investigation*, The Journal of Vacuum Science and Technology B, 2006, **24(4)**: p. 1668-75.
- [246]Perdigao L.M.A, Perkins E.W, Ma J, Staniec P.A, Rogers B.L, Champness N.R. *Bimolecular networks and supramolecular traps on Au(111)*, Journal of Physical Chemistry B, 2006, **110(25)**: p.12539-42.
- [247]Furukawa S, Uji-i H, Tahara K, Ichikawa T, Sonoda M, De Schryver F.C, *Molecular geometry directed Kagome and honeycomb networks: Toward two-dimensional crystal engineering*, Journal of the American Chemical Society, 2006 , **128(11)**: p.3502-3.
- [248]Stohr M, Wahl M, Galka CH, Riehm T, Jung TA, Gade LH, *Controlling molecular assembly in two dimensions: The concentration dependence of*

- thermally induced 2D aggregation of molecules on a metal surface*, *Angewandte Chemie-International Edition*, 2005, **44(45)**: p.7394-8.
- [249]De Feyter S, De Schryver F.C, *Two-dimensional supramolecular self-assembly probed by scanning tunneling microscopy*, *Chemical Society Reviews*, 2003, **32(6)**: p.393-6
- [250]Yokoyama T, Yokoyama S, Kamikado T, Okuno Y, Mashiko S, *Selective assembly on a surface of supramolecular aggregates with controlled size and shape*, *Nature*, 2001, **413(6856)**: p.619-21.
- [251]Mena-Osteritz E, Bauerle P, *Complexation of C₆₀ on a cyclothiophene monolayer template*, *Advanced Materials*, 2006, **18(4)**: p.447-8.
- [252]Theobald J.A, Oxtoby N.S, Phillips M.A, Champness N.R, Beton P.H. *Controlling molecular deposition and layer structure with supramolecular surface assemblies*. *Nature*, 2003, **424(6952)**: p.1029-31.
- [253]Samori P, Engelkamp H, de Witte P, Rowan A.E, Nolte R.J.M, Rabe J.P, *Self-assembly and manipulation of crown ether phthalocyanines at the gel-graphite interface*, *Angewandte Chemie-International Edition*, 2001, **40(12)**: p.2348-9.
- [254]Samori P, Cacialli F, Anderson HL, Rowan A.E, *Towards complex functions from complex materials*, *Advanced Materials*, 2006,**18(10)**: p.1235-8.
- [255]Ziener U, Lehn JM, Mourran A, Moller M, *Supramolecular assemblies of a bis(terpyridine) ligand and of its [2 x 2] grid-type Zn-II and Co-II complexes on highly ordered pyrolytic graphite*, *Chemistry-a European Journal*, 2002,**8(4)**: p.951-7.
- [256]Lin N, Stepanow S, Vidal F, Barth J.V, Kern K, *Manipulating 2D metal-organic networks via ligand control*, *Chemical Communications*, 2005 (**13**):1681-3.
- [257]Hippis K.W, Scudiero L, Barlow D.E,Cooke M.P, *A self-organized 2-dimensional bifunctional structure formed by supramolecular design*, *Journal of the American Chemical Society*, 2002, **124(10)**: p.2126-7.
- [258]Vincent O, Mathieu K, Mathieu A, Louis P, *Influence of stress on hydrogen-bond formation in a halogenated phthalocyanine network*, *Physical Review B*, 2007, **75(3)**: p. 035428.
- [259]Amsalem P, Giovanelli L, Themlin JM, Koudia M, Abel M, Oison V, *Interface formation and growth of a thin film of ZnPcCl₈/Ag(1 1 1) studied by photoelectron spectroscopy*, *Surface Science*, 2007, **601(18)**: p.4185-8.
- [260]Schwieger T, Peisert H, Knupfer M, *Direct observation of interfacial charge transfer from silver to organic semiconductors*, *Chemical Physics Letters*, 2004, **384(4-6)**: p.197-202.
- [261]Nagel M, Biswas I, Peisert H, Chasse T, *Interface properties and electronic structure of ultrathin manganese oxide films on Ag(001)*, *Surface Science*, 2007, **601(18)**: p.4484-7.
- [262]Thalladi V.R, Weiss H-C, Blaser D, Boese R, Nangia A, Desiraju G.R, *H-F interactions in the crystal structures of some fluorobenzenes*, *Journal of the American Chemical Society*,1998, **120(34)**: p.8702-10.

- [263]Der Hovanesian A, Doyon J.B, Jain A, Rablen PR, Sapse A-M, *Models of F-H contacts relevant to the binding of fluoroaromatic inhibitors to carbonic anhydrase II*, Organic Letters,1999, **1(9)**: p.1359-62.
- [264]Eremtchenko M, Schaefer J.A, Tautz F.S, *Understanding and tuning the epitaxy of large aromatic adsorbates by molecular design*, Nature, 2003, **425(6958)**: p.602-5.
- [265]Eremtchenko M, Bauer D, Schaefer J.A, Tautz F.S, *Polycyclic aromates on close-packed metal surfaces: functionalization, molecular chemisorption and organic epitaxy*, New Journal of Physics,2004, **6**, p.4